Atomic dynamics in solids and liquids from inelastic neutron scattering

Thesis by
Camille Marie Bernal-Choban

In Partial Fulfillment of the Requirements for the
Degree of
Doctor of Philosophy

CALIFORNIA INSTITUTE OF TECHNOLOGY
Pasadena, California

2024
Defended September 18, 2023

Camille Marie Bernal-Choban
ORCID: 0000-0001-7550-3153

To all those who offered support and guidance throughout this journey. Your patience, kindness, and encouragement made this work possible. And to those who come after, you can do it.

ACKNOWLEDGEMENTS

I would like to extend my utmost thanks to my advisor, Brent Fultz. Thank you for answering the email from an enthusiastic undergraduate in 2017—it changed my life for the better. You have taught me what it means to be a scientist, from asking the right questions, pursuing the truth (within experimental error), and stepping back to really *think* about what results mean. Your support and guidance through this time will always be remembered.

To my thesis committee, Dr. Katherine Faber, Dr. Garrett Granroth, and Dr. Joseph Falson, thank you. Dr. Faber, thank you for chairing my committee and your infectious enthusiasm for learning. Dr. Faber, Dr. Granroth, and Dr. Falson, your comments and feedback have been invaluable, and I thank you for the time and effort dedicated to perusing and improving these pages.

No experiments in my thesis would have been possible without the amazing support of all the instrument scientists and other personnel at Oak Ridge National Laboratory. Doug Abernathy, thank you for teaching me how to use the ARCS software on my first neutron experiment in 2018 and for your support on all the other experiments we were on. Rebecca Mills, your insight into sample environments when we proposed melting in situ was invaluable. Garrett Granroth, thank you for sharing your knowledge of reduction and analysis scripts with me and always encouraging me to stay in science. I enjoyed getting to know all of you more with each trip to Oak Ridge, and I look forward to seeing you again in the future.

Claire Saunders and Stefan Lohaus, while we began as colleagues, I am so honored to call you my close friends. You are incredible humans and scientists, and I cannot imagine my journey at Caltech without you. Thank you for answering every call and believing in me when I found it difficult to.

I would also like to thank my research group members, present and past, for curating such a welcoming environment. Thank you for checking in when I am stressed and offering me words of support. Your passion for science, balanced with fun activities like museum trips and movie nights, helped me maintain a work-life balance throughout graduate school.

Caleb, my love, words aren't enough to express my gratitude for your continued support through these years. From helping me move and braving a long-distance

relationship so I could earn my Ph.D. to being my sounding board through good and bad days and so many in-betweens, thank you.

Thank you to my mother and father, who encouraged my kitchen ingredient "potion-making" and playing with calculators as a toddler, even if they did not understand why I liked experimenting. You both made me feel like I could be anything I set my mind to.

To those who I have had the privilege of mentoring throughout my Ph.D. years, thank you. You constantly remind me how amazing it is to learn new things, and your enthusiasm for science makes me remember why I became, and why I love being, a scientist.

Lastly, I want to acknowledge my funding sources that have helped make this work possible. During my Ph.D., I received monetary support from the U.S. Department of Energy, Basic Energy Sciences under Contract DE-FG02-03ER46055 and used resources provided by Oak Ridge National Laboratory (ORNL) and the National Energy Research Scientific Computing Center (NERSC).

ABSTRACT

As temperature increases, atomic scale disorder, or entropy, drives the thermophysical properties of materials. One way it does this is by passing heat through materials in the form of vibrations. In solids, vibrational motions are called phonons, and their behaviors are used to predict macroscopic properties such as thermal expansion and thermal conductivity. Other forms of entropy include configurational and electronic entropy, which also evolve with temperature. Configurational changes in solids are often small, but in liquids, the prominence of diffusion makes this contribution significant. This dissertation addresses these atomistic components of entropy in two studies, one on bcc chromium and the other on the melting of monatomic systems.

In the first study, phonon densities of states (DOS) of body-centered cubic (bcc) chromium were measured by time-of-flight inelastic neutron scattering at temperatures up to 1493 K. Density functional theory (DFT) calculations with both quasi-harmonic (QH) and anharmonic (AH) methods were performed at temperatures above the Néel temperature. Features in the phonon DOS decrease in energy (soften) substantially with temperature. A Born-von Kármán analysis using fits to the experimental DOS reveals a softening of almost 17% of the high transverse phonon branch between 330 and 1493 K. The low transverse branch changes by approximately half this amount. The AH calculations capture the observed behavior of the two transverse phonon branches, but the QH calculations give some inverted trends. Vibrational entropies from phonons and electrons are obtained, and their sum is in excellent agreement with the entropy of chromium obtained by calorimetry, indicating that above 330 K, no explicit temperature-dependent magnetic contributions are necessary.

The second investigation delves into the latent heat of melting, defined as $T_m \Delta S_{fus}$, where T_m is the melting temperature and ΔS_{fus} is the entropy of fusion. At the scale of atoms and electrons, ΔS_{fus} has components from changes of atom configurations, atom vibrations, and thermal excitations of electrons. New data analyses were developed for inelastic neutron scattering (INS) to obtain changes in vibrational spectra upon melting. Combining these INS experiments with computational work using thermodynamic integration and molecular dynamics, components of ΔS_{fus} were obtained for a total of six elements, Ge, Si, Bi, Sn, Pb, Li. Upon melting, there is always a positive change of configurational entropy, ΔS_{config}.

A baseline value of ΔS_{config}=1.2 k_{B}/atom, approximately the value for Richard's rule, corresponds to zero change in the vibrational part of the entropy of fusion, ΔS_{vib}. Elements having values of ΔS_{fus} that depart from this value of Richard's rule have both an additional ΔS_{vib} and an additional ΔS_{config}. Surprisingly, the extra ΔS_{config} is close to 77% of ΔS_{vib}, for both positive and negative deviations from Richard's rule. This implies a correlation between the change in the number of basins in a potential energy landscape and the change in the inverse of their curvature upon melting.

PUBLISHED CONTENT AND CONTRIBUTIONS

[1] C. M. Bernal-Choban, V. Ladygin, G. E. Granroth, C. N. Saunders, S. H. Lohaus, D. L. Abernathy, and B. Fultz, "The components of entropy in the latent heat of fusion." C. M. B.-C. planned and performed experiments, analyzed data, and wrote the manuscript. *In preparation*.

[2] C. M. Bernal-Choban, H. L. Smith, C. N. Saunders, D. S. Kim, L. Mauger, D. L. Abernathy, and B. Fultz, "Nonharmonic contributions to the high-temperature phonon thermodynamics of Cr." Phys. Rev. B, **107**, 054312 (2023). DOI: 10.1103/PhysRevB.107.054312. C. M. B.-C. analyzed experimental data, planned and performed all computational work, and wrote the manuscript.

TABLE OF CONTENTS

LIST OF ILLUSTRATIONS

LIST OF TABLES

Chapter 1

INTRODUCTION

When asked to describe my field, I always hesitate about where to begin. Not because there is not much to say—the opposite, in fact—the breadth of materials science is enormous. Over the past eleven years, I have seen materials science evolve to encompass aspects of physics, chemistry, biology, and even computer science. Instead of covering the entire field, this thesis will focus on a small but important corner of materials science, vibrational thermodynamics. This, at least, I can describe well.

For those reading this who might not be scientists, I would like to dedicate this paragraph to explaining the idea and importance of vibrational dynamics. Think of the children's game "telephone," where a chosen sentence passes between people in a line. The catch? Everybody is whispering. Inevitably, a word or two is misheard, and the result differs from the original phrase. Extending this visualization to vibrational thermodynamics, imagine an atom traveling with a set amount of energy (the original sentence). As this atom moves, it transfers some of its initial energy to others (whispering to other players). Discretized vibrations (which have set energies and directions of travel) are a subset of motion called phonons. Much like the original sentence in "telephone," they have lifetimes—lengths of time during which they are unaltered before being whispered awry. The differences in how these phonons propagate, or move, through a material determine how that material responds to external forces, including heat, pressure, and magnetism.

Development and understanding of such responses are crucial to technological advancement. From reinforced steel to semiconductors, our society depends upon materials science. Specifically, we rely on finding and using materials that have desirable properties for a given task. Most semiconductors, which are crucial components of computers, would be a catastrophic choice for reinforcing buildings. However, steel, a mixture of metals, has been used for decades to mitigate structural damage. Finding what materials work and why can be traced back to their fundamental behavior.

A branch of physics called vibrational thermodynamics studies a subset of these fundamental behaviors of materials. In vibrational thermodynamics, temperature

plays a significant role. Returning to the "telephone" game analogy, imagine what would happen if people could move a certain distance in a random direction from their starting position depending on the outside temperature. If warmer weather equates to more movement, people could interact with those previously out of reach. Overall, there is more disarray in the passing of sentences, and the original phrase is likely to be distorted in a shorter time. The amount of disorder associated with this motion is something scientists have named vibrational entropy, and it relates the degree of randomness in a system to the overall energy (and thus behavior) in materials. This thesis focuses on understanding vibrational entropy in elemental solids and liquids.

Throughout this thesis, neutron scattering and anharmonic simulations built upon density functional theory (DFT) and molecular dynamics (MD) are the two main methods used to assess entropy (specifically vibrational) in materials.

Neutron scattering probes vibrational intensity by colliding heavy, uncharged particles known as neutrons with a sample. The material can either lose or gain energy and momentum with each hit. Detecting, recording, and analyzing these events reveals the nature of vibrational interactions. By varying the temperature of the sample and repeating the process, we determine how temperature affects the material. These experimental spectra can be related to vibrational entropy. Often, such experiments can only be performed successfully at national user facilities. Throughout my time as a graduate scholar, I can safely say that I've spent at least three months collecting the data presented here, and this estimate is likely low.

Computer simulations are a powerful tool to confirm results from experimental analyses. Anharmonically informed calculations provide a good description of the temperature-dependent behavior of materials, with the added advantage of being able to separate contributions from fundamental interactions explicitly. In some cases, such simulations confirm our understanding of physics in materials. In others, they reveal previously unexplained physics. Since the calculations to get these properties are intensive, supercomputers also became a necessary part of my graduate studies.

The remainder of this work is structured as follows: Chapter 2 provides general background on topics relevant to the work presented in this dissertation. It begins with an overview of atomic motion, including diffusion and phonons, and outlines traditional ways of mathematically formulating each. Then, it covers neutron scattering and anharmonic calculations and how they are used to obtain and analyze

atomic motion. Chapter 3 presents research and results on chromium (Cr), which shows unusual vibrational behavior at high temperatures. Chapter 4 quantifies the contribution of vibrational, configurational, and electronic entropies to the total entropy of melting in bismuth (Bi), lead (Pb), tin (Sn), and germanium (Ge). These results provide an explanation for deviations from Richard's rule and reveal a surprising fact about the change in the potential energy landscape across melting. To conclude, Chapter 5 considers future directions for this work.

Chapter 2

BACKGROUND

This chapter generally follows information gleaned from references [1–4].

2.1 Atomic Motion

The postulation that everything is made of tiny undividable units—atoms—dates back to ancient Greece. Although we have since found that atoms are not the smallest units of matter, they are often the starting point for visualizing microscopic motion in materials science. Accordingly, this is where we will begin.

Atoms within a solid, liquid, or gas move with varying degrees of randomness. In a gas at equilibrium, an individual atom knows little about how the other particles in the gas behave. As a result, random collisions describe the interactions between atoms well. However, in a solid where atoms are bound to their neighbors, collective motion in the form of quantized waves dominates. Traditionally, these two types of motion are called diffusion (random) and phonons (collective). As this thesis will show, liquids have significant contributing factors from both.

The microscopic motion described above determines the macroscopic properties seen in everyday materials. One goal of thermodynamics is understanding the relationships between fundamental and measured properties. In particular, vibrational thermodynamics studies the temperature dependence of this motion and how it relates to the energetics and, therefore, behaviors of systems.

Diffusion

Three mechanisms for diffusion exist in crystalline solids (repeating units of atoms): interstitial, interstitialcy, and vacancy. The first involves an atom that moves between the periodic lattice of host atoms and is often a different chemical species (Fig. 2.1a). Interstitialcy, shown in Fig. 2.1b, refers to atoms of the same chemical species either replacing a neighbor from, or moving to, an interstitial (in between) site. Vacancy diffusion occurs in lattices with a missing atom (i.e., the atomic arrangement is not perfectly periodic). Within this mechanism, an atom moves into a neighboring empty site, exchanging positions with a vacancy. A two-dimensional case of this is illustrated in Figure 2.1c.

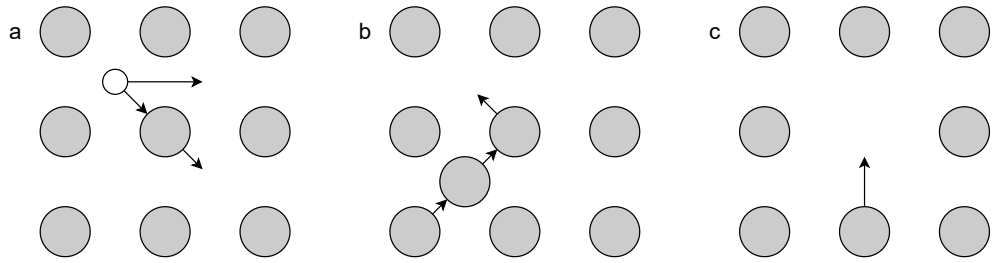

Figure 2.1: Two-dimensional representation of possible diffusion mechanisms in crystalline solids, (a) interstitial, (b), interstitialcy, and (c) vacancy diffusion. Arrows show possible pathways for the diffusing atom(s) to take.

Hereafter, the focus will be on diffusion in liquids and models to describe them. An equilibrium liquid has one primary diffusion mechanism, called single-particle or self-diffusion. Within this steady state picture, atoms roam and collide in a random sequence with their neighbors but do not change the overall energy of the system. For sufficiently long time and spatial scales, this process is approximately continuous with respect to individual jumps.

Continuous diffusion processes have known relationships between flux and concentration (the number of particles in a given volume), Fick's laws. Fick's first law,

$$\mathbf{j}(\mathbf{r}, t) = -D\nabla n(\mathbf{r}, t) \tag{2.1}$$

relates j, the particle flux (the number of atoms passing through an area perpendicular to particle movement in a given time), to the concentration, n, through a diffusion coefficient, D. For a system with a constant number of atoms, the

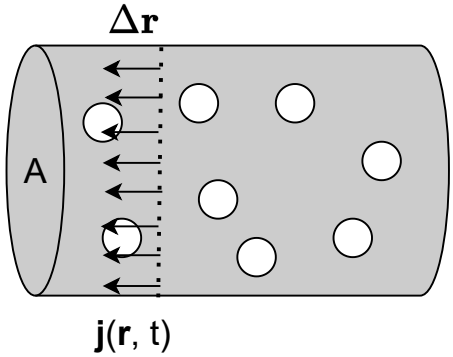

Figure 2.2: Pictoral representation of atoms diffusing a distance $\Delta\mathbf{r}$ through a cylinder with cross-sectional area, A.

particles leaving a subset of the volume must be balanced by a decrease in the concentration of that volume,

$$-\nabla \cdot \mathbf{j}(\mathbf{r}, t) = \frac{\partial n}{\partial t}. \tag{2.2}$$

Substituting the flux from 2.1 into the above continuity equation and assuming D is independent of concentration, Fick's second law,

$$\frac{\partial n}{\partial t} = -\nabla \cdot (-D\nabla n(\mathbf{r}, t)) = D\nabla^2 n(\mathbf{r}, t), \tag{2.3}$$

is found.

Returning to the microscopic (atomic) perspective, consider an atom at position $\mathbf{r}$ at time $t = 0$[1]. Mathematically, this observation relates to the concentration $n(\mathbf{r}, 0) = \delta(\mathbf{r})$. Using this initial condition and assuming that diffusion is equivalent in all directions (isotropic),

$$n(r, t) = \left(\frac{1}{4\pi D|t|}\right)^{3/2} \exp\left(-r^2\right)/4D|t|), \tag{2.4}$$

is a solution to Fick's second law. How the above expression relates to experimental measurements will be given in section 2.2.

Collective vibrational motion

Collective motion in atomic scale systems describes how particles move together in response to each other. Such behavior requires atoms to know or remember their environment within some time scale. This environment is called the potential energy surface (PES), and it contains the energetics of atoms and their surroundings. A one-dimensional representation of PESs for a solid and a liquid is shown in Fig. 2.3.

Within the potential energy surface framework, an atom will "fall into" the position with the least energy. For crystalline solids, these positions form a periodic arrangement called a crystal lattice. In an idealized structure, each particle within this lattice sits at a PES energy minimum, called an equilibrium position, as Fig. 2.4 shows. Realistically, even at zero temperature, atoms vibrate around this equilibrium point. As temperature increases, atoms gain energy[2]. This changes the potential energy landscape, which in turn changes atomic motion[3]. If atoms can

[1] This statement is equivalent to saying that at the beginning of a measurement, there is a 100% probability of an atom being at location r.

[2] This energy is the thermal energy, $\varepsilon = k_B T$ per coordinate degree of freedom.

[3] Atoms with more energy available to them will vibrate more.

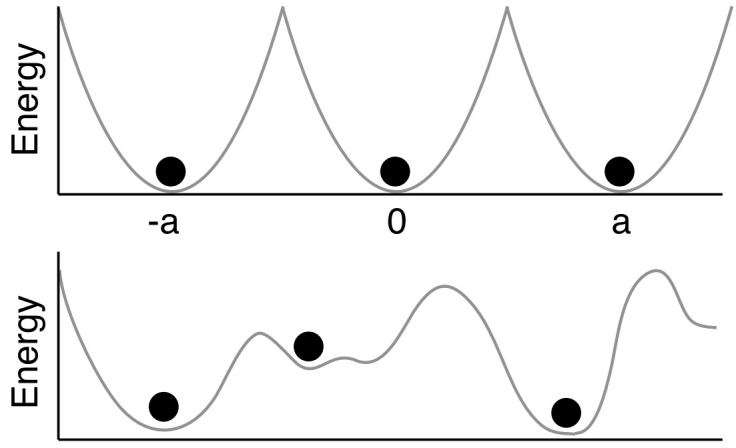

Figure 2.3: Potential energy surfaces in one-dimension for (top) a crystalline solid and (bottom) a liquid. In each, the three atoms are located in the wells with the lowest energy.

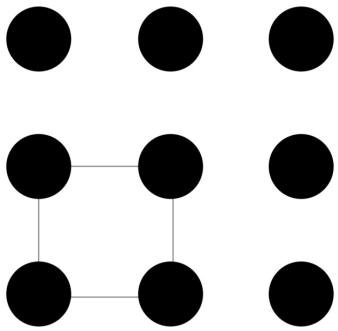

Figure 2.4: Two-dimensional representation of atoms at equilibrium positions in a crystalline solid. The grey rectangle is the repeating motif for the crystal lattice, and extends indefinitely in all directions for an idealized system.

"see" each other (they interact), a change in motion in one affects the others. This propagating response is called collective motion and can be visualized as a wave moving through a material. Some instances are so common that they are given names. Before defining these, it is important to mention two quantities, the wavevector, $\mathbf{k}$, and the wavefunction, $\psi(\mathbf{r}, t) \propto e^{i(\mathbf{k}\cdot\mathbf{r}-\omega t)}$. The former has a magnitude and direction and helps define the direction of wave propagation. The latter describes how the wave changes with position and time[4]. With these definitions in mind, phonons can be classified as longitudinal or transverse. A longitudinal

[4]For example, the amplitude, or height of the wave at a given time and position.

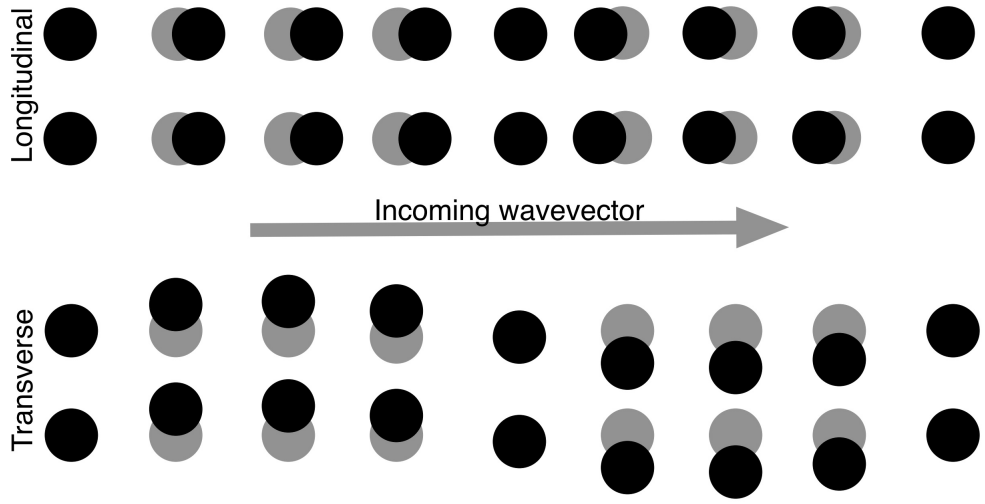

Figure 2.5: Longitudinal (top) and transverse (bottom) phonons in a two-dimensional lattice. Grey atoms depict original equilibrium positions.

phonon is excited when particles in the lattice travel along the same line of motion as **k**, and transverse phonons occur when the resulting atomic movement is perpendicular to the original wavevector (see Fig. 2.5). There are two transverse modes for each longitudinal mode in three dimensions. Each of these is discretized, or has a set energy associated with their creation, that changes with temperature. Describing the temperature evolution of collective motion is a large part of vibrational thermodynamics, and many models have been proposed to predict and understand this behavior in materials.

The harmonic model (HA) is one of the best-known and simplest models to describe vibrational thermodynamics in crystalline solids. It begins by assuming atoms in a lattice interact by springs with forces linear in displacement. In physics, a spring has a known potential energy surface (a parabola), given in one dimension by

$$U_{\mathrm{HA}} = \frac{1}{2} k x^2, \tag{2.5}$$

where k is a force constant, and x is the displacement from an equilibrium lattice position. The strength of the force constant determines the amplitude of atomic vibrations. It is worth noting that any movement within this lattice will continue indefinitely because this model does not have a dissipative (or damping) term. As a result, the thermal properties predicted from this model are inaccurate, with increasing error at high temperatures. However, this approximation helps lay the

mathematical groundwork for predicting vibrational free energy, which is essential for understanding materials behavior.

The above picture imagines the atoms in Fig. 2.4 connected by springs, each with the same energy. In reality, atomic vibrations are quantized with energies, $\varepsilon_n = (n+\frac{1}{2})\hbar\omega$. Two subtle but important points are hidden in this expression: 1) these energies are not continuous, and 2) the $n = 0$ ground state energy is not zero[5]. However, these available energies do lie on a parabolic potential energy surface.

In three dimensions, a lattice with N atoms has $3N$ independent oscillators. Using the above energy levels, a partition function, or how many ways a system can be divided into a subsystem with the same energy, is built. For the harmonic crystal described here, where each atom has access to the same energy levels, this is a product of the partition function for a single oscillator,

$$Z_N = \prod_i^{3N} Z_i = \prod_i^{3N} \frac{e^{-\beta\varepsilon_i/2}}{1 - e^{-\beta\varepsilon_i}}, \tag{2.6}$$

where $\beta = 1/(k_B T)$ and k_B is Boltzmann's constant. The importance of Z_N here is that it is directly related to the vibrational free energy, $F_{\text{vib}} = -k_B T \ln Z_N$. Unfortunately, experiments cannot measure this value. However, a continuous quantity called the vibrational entropy, given by $S_{\text{vib}} = -(\partial F_{\text{vib}}/\partial T)$, is experimentally accessible[6]. A more common definition of S_{vib} is

$$S_{\text{vib}} = 3k_B \int_0^\infty g(\varepsilon)[(n(\varepsilon)+1)\ln(n(\varepsilon)+1) - n(\varepsilon)\ln(n(\varepsilon))]d\varepsilon, \tag{2.7}$$

where $g(\varepsilon)$ is a normalized continuous vibrational spectrum of frequencies called the density of states (DOS)[7] and

$$n(\varepsilon) = \frac{1}{e^{\beta\varepsilon} - 1} \tag{2.8}$$

is the (Planck) occupancy of a vibrational mode with energy ε at a given temperature, T. A more intuitive way to think about this expression for vibrational entropy is as an adding of the vibrations active for a specified temperature multiplied by the disorder these vibrations contribute to the system. In theory, knowledge of these quantities gives thermal expansion, thermal conductivity, and other thermally driven properties of materials. However, two significant shortcomings of the

[5] This is the origin of the zero point motion mentioned earlier.

[6] One method to do so, neutron scattering, is discussed later.

[7] An example of a DOS and how to read it is given in Section 2.2.

harmonic approximation make its predicted values fall short. One is that the energy of the oscillators remains unchanged in response to external parameters, such as temperature or pressure. In the PES view, this is keeping k constant. The second assumption is that these oscillators stay independent with increasing temperature (same as the above statement for no dissipative terms in the potential energy). At low temperatures, this doesn't affect calculated values too much because fewer vibrational modes are active, and therefore, they have fewer opportunities to interact with others. As temperature rises, more vibrational modes (phonons) are created, and they interact more often, changing the shape of the potential energy surface. Therefore, including T only through the Planck occupancy factor is insufficient to describe materials.

One common modification to the harmonic model is the quasiharmonic approximation (QHA). This model uses the intuition that an increase in temperature should lead to a change in the distances between atoms. By mapping a volume change to temperature, this model provides a prediction of the thermal expansion of a crystalline lattice. Returning to the description of atoms as interconnected springs, this is equivalent to changing k, the force constant in Eq. 2.5. If the force constant softens (decreases) or stiffens (increases) with temperature, the range of movement of particles in a lattice will change, resulting in new equilibrium positions. The new minimum energy site that atoms find affects the volume of the entire lattice, as Fig. 2.6 shows. Mathematically, this is equivalent to minimizing the Helmholtz free energy,

$$F(T,V) = U(T,V) - TS(T,V) \approx U(T,V) - TS_{\text{vib}}(T,V), \qquad (2.9)$$

where U is the internal energy, T is temperature, and S is entropy. In practice, finding the volume that minimizes the energy is trial and error. The process begins by generating lattices with different volumes[8]. A harmonic approximation for each yields a Helmholtz free energy for a given lattice, and the minimum volume for each temperature is the one that has the lowest energy. Therefore, by adding a volume change to the HA, the QHA can give a description of thermal expansion. However, because it is an extension of the harmonic approximation, the QHA suffers from the assumption that the oscillators remain independent of each other with increasing temperature.

An anharmonic framework is needed to address accurate temperature and volume dependence of collective motion. Generally speaking, an anharmonic model is

[8] In the QHA this changes the oscillator energy since $k = m\omega^2$ and $\varepsilon = \hbar\omega$.

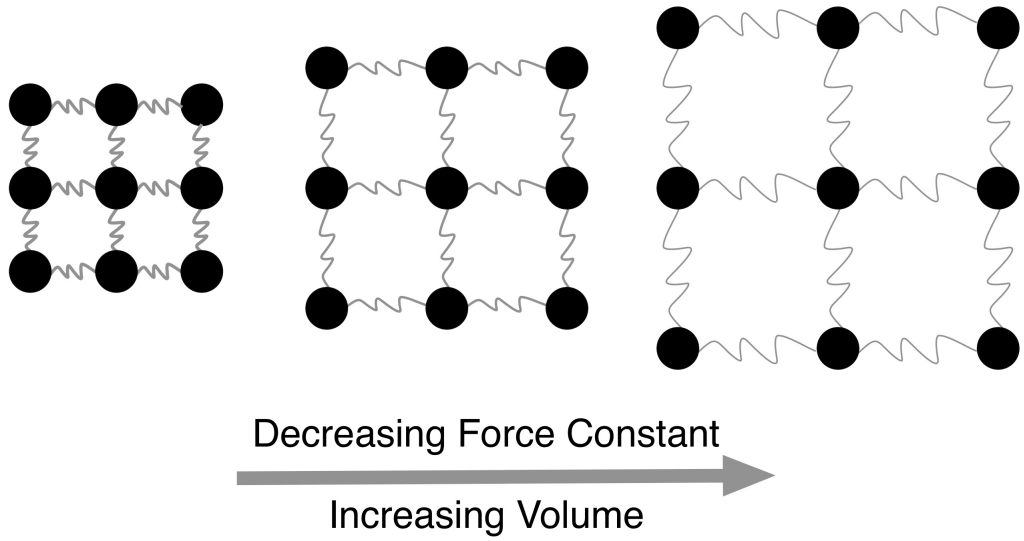

Figure 2.6: Illustration of how the quasiharmonic approximation expands or contracts a lattice by changing the strength of a spring connecting atoms. A larger force constant corresponds to a stiffening—it takes more energy for an atom to vibrate—and a smaller force constant is called a softening and has the opposite effect. This is reflected in the minimum energy sites that atoms take, and at a fixed temperature, the volume will decrease in the former and expand in the latter.

any model that considers contributions beyond the harmonic and quasiharmonic approximations. In doing so, the picture of springs connecting lattice sites falls apart. Now, atoms feel and respond to the effects of their neighbors vibrating in addition to their own oscillations. These additional effects appear in the potential energy surface,

$$U_{\mathrm{AH}} = k_2 x^2 + k_3 x^3 + k_4 x^4 + \cdots . \tag{2.10}$$

Figure 2.7 shows how the PES (at a fixed temperature) of a single atom in one dimension changes with increasing orders of anharmonicity. Although the potential energy surface of a liquid is much more complicated, anharmonic potential energy surfaces also suffice to describe collective motion in such systems, provided that atoms in liquids exhibit solid-like oscillations about temporary (non-periodic) equilibrium positions such as the one in Fig. 2.3. Addressing details on the computational implementation of AH models is the focus of a subsequent section.

Techniques such as neutron scattering directly measure the true vibrational dynamics of a material, including collective motion. This experimental method is discussed next.

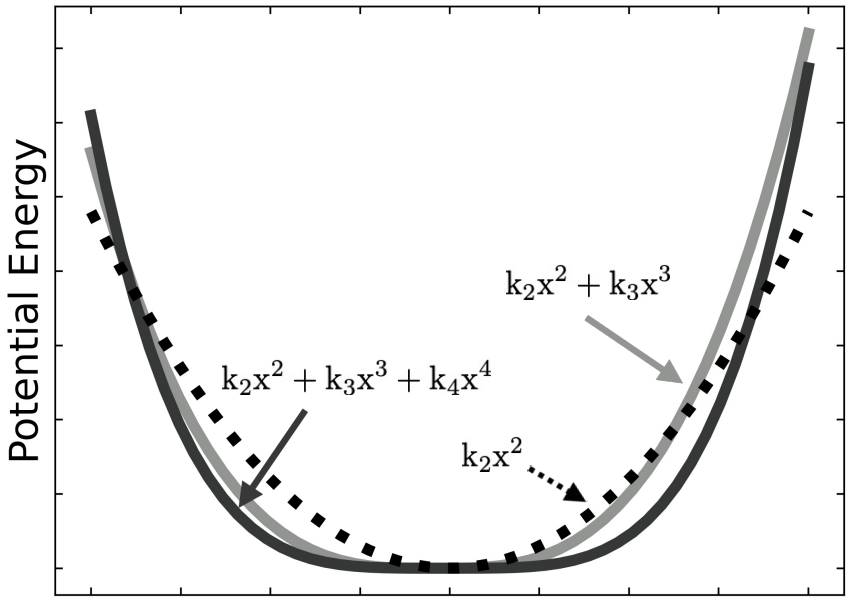

Figure 2.7: One dimension potential energy surfaces illustrating the effects of including anharmonic terms on the shape. In the harmonic approximation, atoms are restricted to a smaller space in x to explore compared to potentials that include anharmonic terms.

2.2 Neutron Scattering

It would be irresponsible to begin a neutron scattering section without briefly mentioning the neutron itself. Neutrons have a definitive mass and charge (it is zero), which are particle-like, but also have wave-like properties such as wavelength, defined as $\lambda = h/\mathbf{p}$, where h is Planck's constant and $\mathbf{p}$ is momentum. This particle-wave duality is a well-known behavior of subatomic particles that allows for the development of scattering theory for neutrons with energy E and wavevector (inverse wavelength), $\mathbf{k} = 2\pi/\lambda$.

Since neutrons are neutral, they predominately scatter from the nuclei of atoms within a material. If neutrons have energies (and therefore wavelengths) on the order of the thermal energy, $E \sim k_B T$, they are called thermal neutrons. Interactions with thermal neutrons directly inform where atoms are within a material, whether at their equilibrium position or not. These are the neutrons discussed here. A typical scattering event, shown in Fig. 2.8, occurs when an incoming neutron with wavevector $\mathbf{k}_i$ and energy E_i collides with an atomic nucleus. Upon

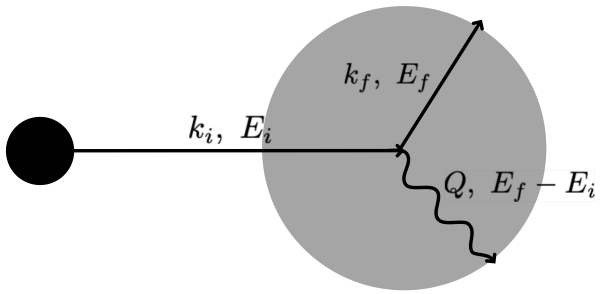

Figure 2.8: An incident neutron with energy E_i and momentum $\hbar\mathbf{k}_i$ colliding with a nucleus in the sample. After impact, the neutron has energy E_f and momentum $\hbar\mathbf{k}_f$. The difference in energy (gain or loss), $E_i - E_f$ is transferred to the sample, along with momentum, $\hbar\mathbf{Q} = \hbar(\mathbf{k}_i - \mathbf{k}_f)$.

impact, the sample can lose or gain momentum ($\hbar\mathbf{Q} = \hbar(\mathbf{k}_i - \mathbf{k}_f)$) and energy ($\Delta E = E_i - E_f$) from the neutron[9]. If the initial neutron energy, E_i is the same as the final, E_f, this scattering is elastic and probes the equilibrium static structure of the material. Inelastic scattering occurs when E_i is not equal to E_f, and captures the dynamics (including diffusion and collective motion) of the system. To get material responses, the losses and gains of the neutron energy and momenta need to be interpreted with respect to the *sample*.

A good place to begin is the neutron cross-section. It is defined as the area a neutron sees as available to scatter from (see Fig. 2.9), and it varies between materials. Correspondingly, a target with a small cross-section means incoming neutrons are less likely to scatter from it over a given time compared to a larger one. Mathematically, this is

$$\sigma_s = \frac{\text{(total flux of neutrons scattered per second)}}{\Phi_0}, \tag{2.11}$$

where Φ_0 is the total flux of neutrons being sent at the target per second. In the context of this work, the quantity of interest is the partial differential cross-section (PDCS),

$$\frac{d^2\sigma}{d\Omega dE_f}, \tag{2.12}$$

[9]For future reference, working in terms of energy and momentum is called working in reciprocal space.

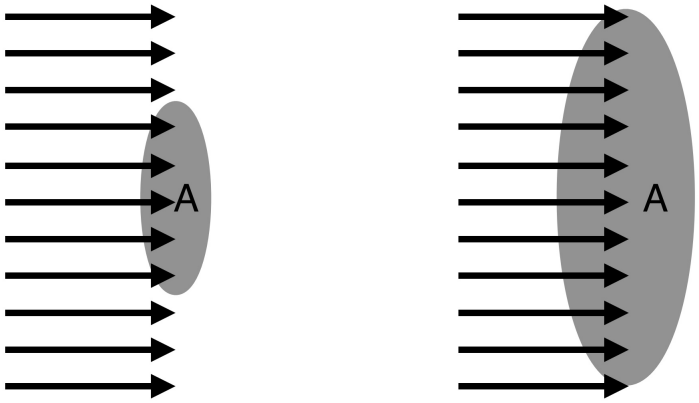

Figure 2.9: Cartoon of neutron scattering with the same incident flux, Φ_0, and different cross-sections. Six out of the eleven incoming neutrons will not interact with the target on the left, but all will interact with the sample on the right. The left is said to have a smaller cross-section than the right.

the number of neutrons scattered per second into solid angle $d\Omega$ about a given direction with final energy between E_f and $E_f + dE_f$ [2]. The primary takeaway from this expression is that the angle neutrons scatter off a sample and their final energies are important.

From the above description, a logical assumption is that if the neutron partial differential cross-section is material dependent, it should be able to link scattering to the properties of the system itself. This thinking is correct, but not without its caveats. For example, what properties are reasonable to get from cross-section analyses? There is more than one answer, but recall that the regime of interest here is thermal neutrons. Therefore, the properties within reach are those on the spatial scale of crystalline lattices, including magnetic excitations and atomic motion. The latter describes the dynamics of materials (diffusion and collective motion). The first step in connecting the PDCS to such properties of materials is introducing the autocorrelation function, $\langle \hat{A}^\dagger \hat{A}(t) \rangle$.

Generally speaking, an autocorrelation function is a mathematical way of giving the statistical correlation of the same parameter of a system at two different points in space and time. Here, the autocorrelation function, $\langle \hat{A}^\dagger \hat{A}(t) \rangle$, measures how property A of the material evolves with time with respect to its initial value. Another way of putting this is if A is one value, is it aware of or influenced by

its value at an earlier time? (If this sounds suspiciously like the atomic motion section above, it should.) The power of this formalism becomes apparent in the expression,

$$\frac{d^2\sigma}{d\Omega dE_f} = \frac{k_f}{k_i}\frac{\sigma}{2}\frac{1}{2\pi\hbar}\int_{-\infty}^{\infty}\langle\hat{A}^\dagger\hat{A}(t)\rangle\exp(-i\omega t)dt \tag{2.13}$$

where the PDCS is related to the integral over time of the correlation function multiplied by an exponential that contains the energy of the *material*. Therefore, by measuring the cross-section and recording the momentum and energy changes in a neutron, the static and vibrational (and magnetic) properties of the material "fall out"! Specifically,

$$\mathcal{S}(\mathbf{Q},\omega) = \frac{1}{2\pi\hbar}\int_{-\infty}^{\infty}\langle\hat{A}^\dagger\hat{A}(t)\rangle\exp(-i\omega t)dt \tag{2.14}$$

(the $\mathbf{Q}$ dependence is hidden in $\hat{A}$) is *only* material dependent and is known in the neutron scattering community as the scattering function, the dynamical structure factor, or the response function. Traditionally, $\mathcal{S}(Q,\omega)$ is used to separate the PDCS into two components, the coherent and incoherent partial differential cross-sections,

$$\left(\frac{d^2\sigma}{d\Omega dE_f}\right)_{\text{coh}} = \frac{\sigma_{\text{coh}}}{4\pi}\frac{k_f}{k_i}N\mathcal{S}(Q,\omega), \tag{2.15}$$

and

$$\left(\frac{d^2\sigma}{d\Omega dE_f}\right)_{\text{inc}} = \frac{\sigma_{\text{inc}}}{4\pi}\frac{k_f}{k_i}N\mathcal{S}_i(Q,\omega), \tag{2.16}$$

where $\sigma_{\text{coh(inc)}}$ are the coherent (incoherent) cross sections, and $\mathcal{S}_i$ is the incoherent scattering function. The coherent term describes correlations between the positions of different atoms in the material over time (i.e., it gives interference effects), and the incoherent portion gives the correlation between the positions of the same atom at different times.

The preceding paragraphs motivate what measurements are needed but not how they are collected. In practice, focusing neutrons and measuring the partial differential scattering cross-section requires significant effort and precision. This task becomes more difficult when measuring the dynamic properties of materials (i.e., vibrational spectra) due to the reduction of intensity in inelastic ($E_i \neq E_f$) scattering. For this reason, all the experiments reported here were performed using resources at the Spallation Neutron Source (SNS) located at Oak Ridge National Laboratory (ORNL) [5].

The SNS hosts a variety of instruments that probe different time and length scales. For the measurements here, the beamline of choice was ARCS, the wide

angular-range chopper spectrometer, which offers energy and momentum resolution uniquely suited for studying vibrational spectra [6]. It is a time-of-flight direct geometry instrument (the initial energy of the neutron beam is selected) with an array of detectors arranged in a half cylinder. Two choppers, a T0 chopper to block the prompt pulse of fast (energy greater than thermal) neutrons, and a Fermi chopper are used to determine the incident energy of the neutron on the sample (see Fig. 2.10). Momentum transfer between scattered neutrons and the

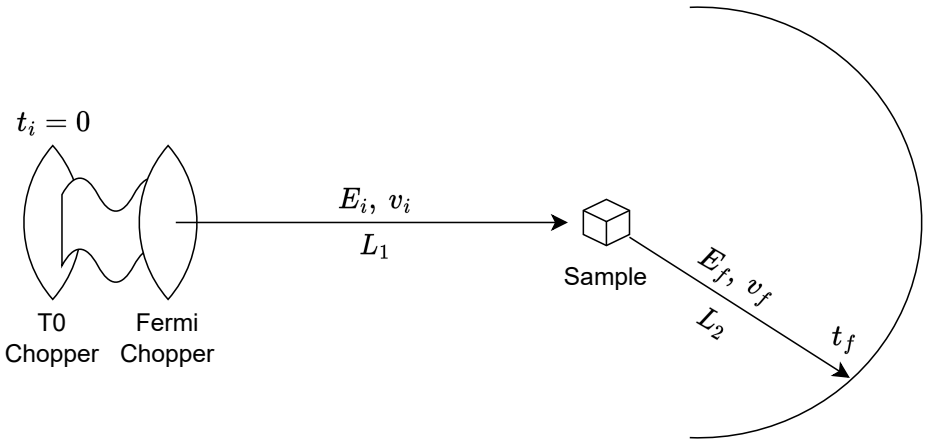

Figure 2.10: The flight path of a neutron beam at ARCS. An incident neutron beam with a spread of energies passes through a T_0 chopper, is monochromated (one energy is picked out) by a Fermi chopper, and scattered by the sample before being recorded by an array of detectors. Since the distances between the Fermi chopper and the sample (L_1) and the sample and the detectors (L_2) are known, the final energy of the neutron (and therefore the energy lost or gained by the sample, $\Delta E_s = E_i - E_f$) can be measured.

incident (forward) beam leverages detector placement (Fig. 2.11) — when an impact is detected, the location of the detector corresponds to an angle, which using the scattering triangle ($|\mathbf{Q}| = |\mathbf{k}_i - \mathbf{k}_f|$), gives momentum. Collecting all this data and removing the neutron contributions yields intensity as a function of energy and momentum, an $\mathcal{S}(Q, \omega)$!

However, this is not the end of the story. Scattering from an incident neutron beam contains elastic (static) and inelastic (dynamic) components. Vibrational spectra, specifically collective motion, which are the focus of this thesis, are purely inelastic, so a method of separating the two contributions is necessary. Some approaches to do this for ARCS data are outlined below.

Begin by envisioning a solid at equilibrium. Its atoms move about their minimum energy point in the PES but, on average, remain at their lattice points. Now,

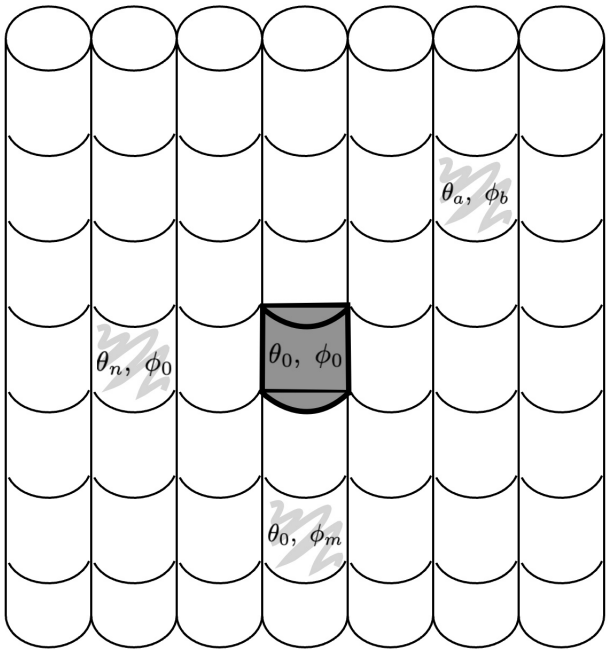

Figure 2.11: Flattened detector view from the sample where the forward beam is taken to arrive at $\theta_0,\ \phi_0$. Pixels within the detector are assigned a solid angle, represented by $\theta,\ \phi$, where θ represents the component in the plane parallel to the path of the incident neutrons, and ϕ designates those in the perpendicular plane.

divide these components into two categories: one constant in time (the lattice positions) and one changing with time (motion). The static part has the property that it will be the same at $t = 0$ and $t = \infty$. Movement, even if it is collective, cannot exist indefinitely and will decay to zero over time. These are correlation functions that describe the properties of a material on an atomic scale, so they must contribute to the scattering function. They do, and rewriting $\mathcal{S}(\mathbf{Q}, \omega)$ gives,

$$\begin{aligned} \mathcal{S}(\mathbf{Q}, \omega) &= \frac{1}{2\pi\hbar} \int_{-\infty}^{\infty} \langle \hat{A}^{\dagger} \hat{A}(t) \rangle \exp(-i\omega t) dt \\ &= |\langle \hat{A} \rangle|^2 \delta(\hbar\omega) + \tilde{\mathcal{S}}(\mathbf{Q}, \omega) \end{aligned} \tag{2.17}$$

where δ is the elastic (static) contribution and $\tilde{\mathcal{S}}(\mathbf{Q}, \omega)$ is the dynamic component of the response function. Figure 2.12 shows what these components look like from data taken at ARCS (and explains how to read an $\mathcal{S}(\mathbf{Q}, \varepsilon = \hbar\omega)$). In a solid, removing the elastic peak and analyzing the vibrational components gives the vibrational thermodynamics of materials. More on exactly what is wanted out of this analysis will follow.

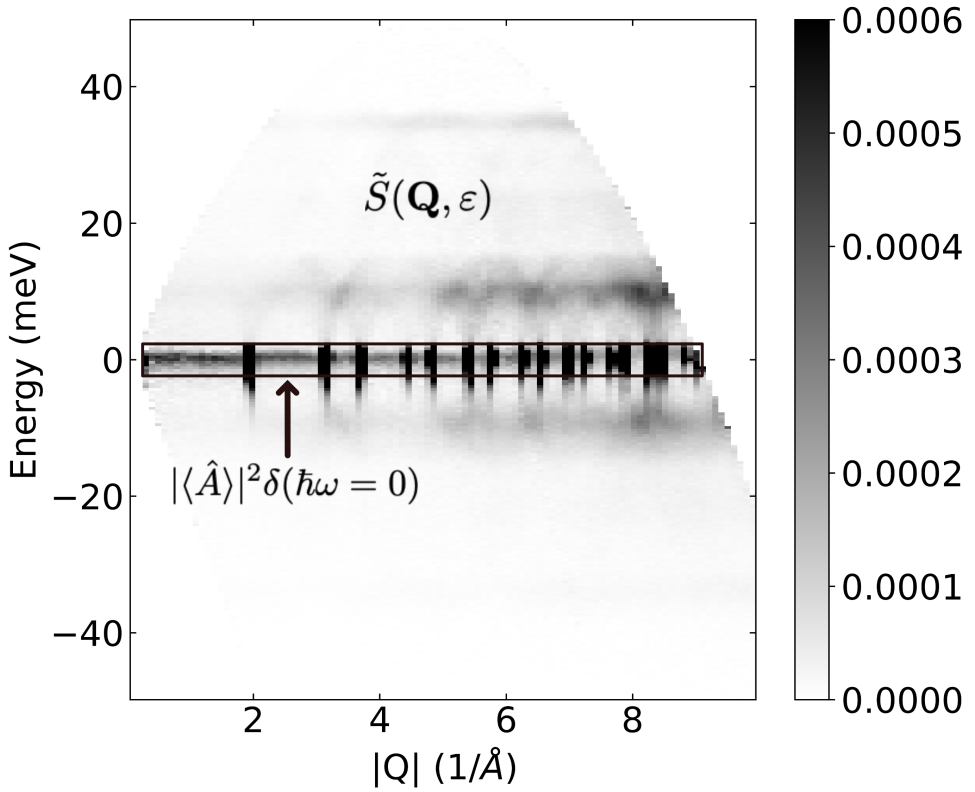

Figure 2.12: Scattering function, $\mathcal{S}(\mathbf{Q}, \varepsilon = \hbar\omega)$ for crystalline germanium (Ge) at ambient (room) temperature. Energy transfer to the sample is on the y-axis, and the x-axis is the magnitude of momentum transfer. The static part of the response function occurs at zero energy transfer (the boxed portion). It can be further divided into coherent (the dark vertical spots) and incoherent (the zero energy streak) elastic scattering, where the former has an intensity that is dependent on momentum transfer and the latter does not. Note that the measured "zero" energy transfer does have some intensity away from true zero—this is a result of instrument resolution (everything cannot be measured perfectly). Everything else is part of the dynamic response function, which is the focus of this work. It, too, contains coherent (curves around 10 meV) and incoherent (streak at approximately 35 meV) parts.

Interpreting neutron scattering spectra from liquids is more complicated. Since there is no elastic line (a liquid lacks fixed lattice positions in time), the response function is entirely dynamic. The two different types of dynamics that compete in a liquid, diffusion and collective motion, each contribute distinct intensities to the scattering spectra. It is the latter that is useful for understanding the vibrational properties of materials, so a way to separate these intensities is desirable. To do

so, start by recalling that diffusion is a random sequence of collisions that results in a rearrangement of atoms. The solution to the diffusion equation, 2.4, describes the probability of finding a particle at time t in a unit volume at displacement r from a point occupied by the same particle at $t = 0$, and is, therefore, a correlation function[10]. Performing a Fourier transform (a mathematical tool to "convert" to reciprocal space) on this equation yields

$$\mathcal{S}(Q,\omega) = \frac{1}{\pi}\frac{\hbar\Gamma(Q)}{(\hbar\omega)^2 + (\hbar\Gamma(Q))^2}\ , \tag{2.18}$$

a Lorentzian function with width Γ. For sufficiently small Q, $\Gamma = DQ^2$ where D is the diffusion coefficient. Physically, this makes sense. If a liquid is at equilibrium, the energy transferred during a single diffusion event rapidly dissipates throughout the system. This particular case of inelastic scattering, characterized by ($\varepsilon \approx 0$), is called quasielastic scattering (QENS), and it has features that resemble a broadened elastic line — this is exactly the Lorentzian from above. Notably, QENS broadening strongly depends on momentum transfer, unlike the elastic line in a solid. This adds an additional step of subtracting a Q dependent part of the inelastic spectra but doing so leaves behind the collective motion.

After measuring neutron scattering data and performing the abovementioned separation, it is *finally* time to relate it back to vibrational thermodynamics. To do this, recall equation 2.7, the vibrational entropy. The term in the square brackets (the entropy of a single oscillator with energy ε) is known for a given temperature and energy range. What is unknown is the vibrational density of states for a material[11]. Or is it? From Fig. 2.13, a DOS is a normalized representation of all the frequencies at which collective modes can be excited, i.e., the vibrational response of one neutron creating (or annihilating) a quantized oscillation. This is what the collective motion data from ARCS are, almost. Although the dynamic intensity from the measured partial differential cross-section is primarily from creating or annihilating a single quantum of oscillation, there is also a contribution from exciting more than one collective mode with a single neutron impact. The latter process is called multiphonon scattering (see Fig. 2.14). Such scattering does not provide an accurate representation of the energy of a quantized wave in a material because while the energy change in neutrons is detectable, there is

[10] It is assumed here that a classical description is accurate enough because $\hbar\omega << k_B T$ for most liquids.

[11] The vibrational DOS can be calculated within a harmonic approximation using the partition function, but the true value requires measurements or anharmonic theory.

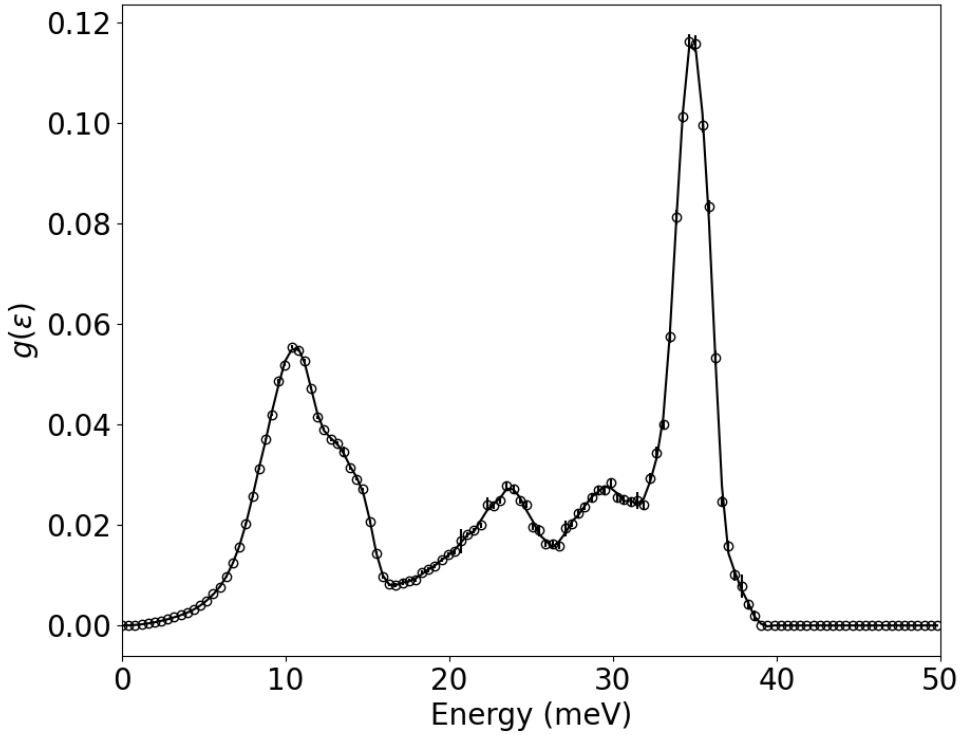

Figure 2.13: A vibrational density of states (DOS) of crystalline Ge at 300 K from data taken at ARCS. At each energy, the value of $g(\varepsilon)$ gives the relative number of vibrational states available. The sharp peaks in the spectra are the central energies of phonons. In order of increasing energy, for Ge, these are the transverse acoustic, longitudinal acoustic, longitudinal optical, and transverse optical modes.

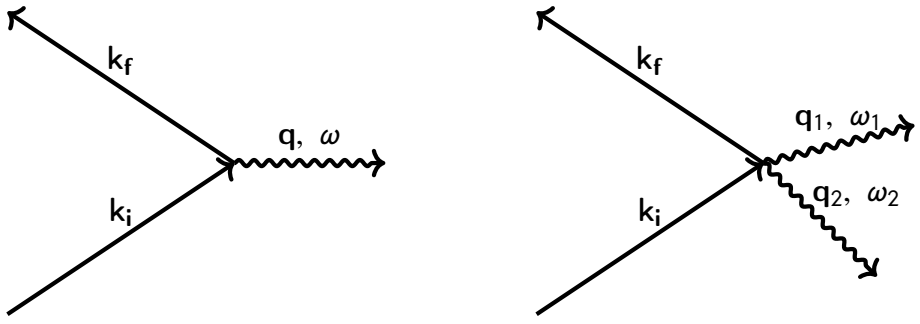

Figure 2.14: Illustrative comparison of single (left) versus double (right) collective mode excitation upon impact with a neutron.

no way to trace their exact path. This is a complicated way of saying that there is no way to tell whether a particular neutron creates or destroys more than one phonon. Thankfully, a mathematical representation of this multiphonon scattering (that relies on an approximation that is not derived here) makes removing this component possible. Once removed, the singly excited spectra are converted into a density of states, the vibrational entropy is calculated, and the vibrational effects on the behavior of the material are determined using the Helmholtz free energy.

2.3 Computational Thermodynamics

Computational methods complement experimental measurements. In addition to predicting the behavior of materials, different contributions from fundamental interactions can be "turned off" to better understand individual roles. The caveat is that simulations must accurately reproduce the real (measured) system. Therefore, such computations must include anharmonic effects, which are non-trivial[12]. Two frameworks that include anharmonicity are the temperature-dependent effective potential (TDEP) and the machine-learning interatomic potential (MLIP) [7, 8]. Both build upon density functional theory, which predicts the ground state (0 K) of materials using the full quantum mechanical relationships between atoms. Each is discussed in more detail below.

The premise of TDEP is the creation and mapping of a model Hamiltonian (a function that describes the total energy of a system) to that of a simulated material. Within TDEP, the model Hamiltonian is perturbative, i.e., the displacements from the equilibrium lattice positions are small[13]. This assumption allows an explicit Hamiltonian for a material to be written as

$$\begin{aligned}\mathcal{H} = U_0 + \sum_i \frac{p_i^2}{2m_i} + \frac{1}{2!}\sum_{ij\alpha\beta} \Phi_{ij}^{\alpha\beta} u_i^\alpha u_j^\beta \\ + \frac{1}{3!}\sum_{ijk\alpha\beta\gamma} \Phi_{ijk}^{\alpha\beta\gamma} u_i^\alpha u_j^\beta u_k^\gamma + \cdots,\end{aligned} \tag{2.19}$$

where the first line contains only harmonic terms. The ϕ are atomic force constants, similar to the ones introduced in Section 2.1, but ϕ_{ij} tracks the forces felt between atomic pairs, and ϕ_{ijk} represents forces from three atom interactions.

[12] Higher order anharmonicities are challenging to separate. For example, some quartic (x^4) contributions are inseparable from the quadratic (x^2) components. This lack of individual identification makes it difficult to explicitly include in a model.

[13] The assumption that atomic displacements are small means that TDEP cannot be used to predict properties of liquids.

Density functional theory offers one way to get these forces by performing a series of calculations on stochastically generated atomic configurations[14]. Once a sufficient sampling of the force constants in a system is obtained, they are fit to the model Hamiltonian using a minimization scheme.

In practice, getting a good representation of these atomic forces is a multi-step process. The first step is creating a grid of unit cells (the smallest repeating lattice) with different volumes (five is usually the minimum needed) for each temperature. Unit cells often cannot capture accurate interactions between atoms in a real system, so supercells, or structures consisting of more than one unit cell (see Fig. 2.15), are used. Next, temperature effects are introduced by generating atomic

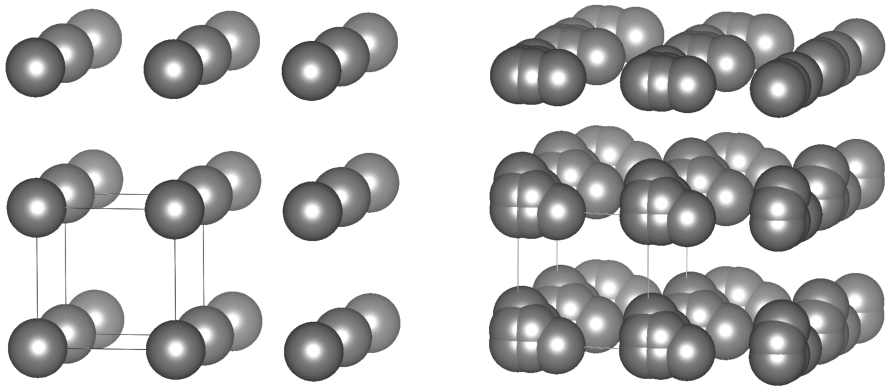

Figure 2.15: Two supercells of a simple cubic lattice, one (left) without any atomic displacements and the other (right) with atoms located at potential displacement positions for a fixed temperature, T. The unit cell is drawn with solid gray lines.

displacements based on Bose-Einstein statistics (plus some randomness). For each volume, up to twenty stochastically displaced supercells can be necessary. Forces from density functional theory calculations on the resulting supercells then get

[14]While density functional theory is itself a ground state method, it is possible to find the effects of temperature on the forces between atoms by introducing displacements using a thermodynamic ensemble.

mapped to Equation 2.19 using nonlinear least squares optimization. This process is iterative, or needs to be repeated, using force constants from either an initial guess or a previous run. Achieving convergence (the difference between one set of runs and the next is small) takes approximately three iterations. Altogether, this is a lot of calculations (~300 per temperature). The good news is that once these forces are known, a Fourier transform of the force constants yields the dynamical matrix, which contains the frequencies and, therefore, the energies of the collective motion (phonons). Since these were calculated from an effective potential that reflects a specific temperature, these quantized energies will include anharmonicity. The usual methods of obtaining S_{vib} are then used to determine the vibrational contributions to the behavior of materials.

Before discussing MLIP, it is best to introduce molecular dynamics (MD). At its core, molecular dynamics uses the position and velocities of atoms at an initial time to calculate the position and velocity of those same atoms at later times. From a quantum mechanical perspective, this is very computationally expensive, especially for large systems (anything over 1000 atoms, and for reference, about a *trillion* fit into the period at the end of this sentence). Instead, classical physics (based on Newtonian physics) with force fields, mathematical representations of the local energy landscape as a function of atomic coordinates, are used. The downside is that these force fields are often unstable, and for extended run times, which are necessary for watching how a system evolves with time, atoms can be "lost" or begin to act erratically. A middle ground with the accuracy of quantum mechanical calculations but the computational cost of classical simulations is needed. One solution is using machine learning to create a robust force field.

As implied by the name, MLIP relies on machine learning to model the energy landscape of materials. The general outline is to build an interatomic force field from an initial training set, use a combination of quantum mechanical and classical molecular dynamics simulations to actively select "good" configurations for a system (which updates the force field), and use the potential generated from this process to perform a long-time molecular dynamics calculation[15]. This final calculation will be representative of the observed material. An advantage of this framework is that a perturbative approximation is not assumed, so it can simulate liquids.

[15]The mathematical details of the training process are beyond the scope of this section, but it is worth mentioning that the initial training set uses high-accuracy density functional theory. More information on running classical molecular dynamics can be found at [9].

Outputs from molecular dynamics simulations with MLIP contain the velocities of atoms at any given time step. For a large enough system[16], having the velocities at time $t = 0$ and $t \neq 0$ is equivalent to knowing the vibrational response of a material since this information describes how the motion of an atom changes in time. And, recalling the neutron scattering section, this time evolution of velocity can be cast into an autocorrelation function, $\langle v(t) \cdot v(0) \rangle$. This particular correlation function, called the velocity autocorrelation function, is related to the vibrational density of states of a material by

$$g(\omega) = \frac{\int_{-\infty}^{\infty} \sum_i^N m_i \langle v_i(t) \cdot v_i(0) \rangle dt}{3Nk_B T}, \tag{2.20}$$

where N is the number of atoms in the simulation, k_B is Boltzmann's constant, and m_i and v_i are the velocity and mass of the ith atom. Notably, this is (in theory) a fully anharmonic density of states, which, when used in the expressions for S_{vib} and $F = U - TS$, yields the contribution of motion to the free energy of materials.

This background outlines how one can use experiments and computations to understand the fundamental (microscopic) processes that determine thermodynamic functions that control how materials behave on a macroscopic scale. The following chapters use a combination of these tools to explore the role of vibrational dynamics in pure elements, one beyond a magnetic transition, and the others across the melt.

[16] This is an informal way of ensuring statistical accuracy is achieved.

References

[1] G. L. Squires, *Introduction to the theory of thermal neutron scattering*, 3rd ed. (Cambridge University Press, 2012).

[2] A. Boothroyd, *Principles of neutron scattering from condensed matter* (Oxford University Press, 2020).

[3] B. Fultz, *Phase Transitions in Materials*, 2nd ed. (Cambridge University Press, Cambridge, 2020).

[4] B. Fultz, JOM **58**, 58 (2006).

[5] T. E. Mason, D. Abernathy, J. Ankner, A. Ekkebus, G. Granroth, M. Hagen, K. Herwig, C. Hoffmann, C. Horak, F. Klose, S. Miller, J. Neuefeind, C. Tulk, and X.-L. Wang, AIP Conf Proc **773**, 21 (2005).

[6] D. L. Abernathy, M. B. Stone, M. J. Loguillo, M. S. Lucas, O. Delaire, X. Tang, J. Y. Y. Lin, and B. Fultz, Rev. Sci. Instrum. **83**, 015114 (2012).

[7] O. Hellman, I. A. Abrikosov, and S. I. Simak, Phys. Rev. B **84**, 180301 (2011).

[8] I. S. Novikov, K. Gubaev, E. V. Podryabinkin, and A. V. Shapeev, Mach. Learn.: Sci. Technol. **2**, 025002 (2021).

[9] A. P. Thompson, H. M. Aktulga, R. Berger, D. S. Bolintineanu, W. M. Brown, P. S. Crozier, P. J. in 't Veld, A. Kohlmeyer, S. G. Moore, T. D. Nguyen, R. Shan, M. J. Stevens, J. Tranchida, C. Trott, and S. J. Plimpton, Comp. Phys. Comm. **271**, 108171 (2022).

Chapter 3

HIGH-TEMPERATURE PHONON THERMODYNAMICS OF CR

Adapted from "Nonharmonic contributions to the high-temperature phonon thermodynamics of Cr." [1].

3.1 Introduction

Understanding the vibrational, electronic, and magnetic interactions in condensed matter is fundamental to predicting the thermodynamic functions of materials such as free energy, internal energy, and entropy. These thermodynamic functions are essential for constructing phase diagrams, predicting thermal expansion, and explaining the temperature dependence of elastic constants, bulk moduli, and magnetization [2]. There are active investigations into these topics for their own sake, and for their importance to the structure and properties of materials [3–8].

One intriguing system is body-centered cubic (bcc) chromium, whose vibrational, electronic, and magnetic free energy contributions result in a transition from an antiferromagnet to a paramagnet, and show an apparent anharmonicity with increasing temperature [9]. Below the Néel transition temperature, $T_N = 311\,\mathrm{K}$, a single crystal of Cr is a conventional itinerant antiferromagnet [10]. At T_N, Cr retains the bcc structure but becomes paramagnetic [11, 12]. In general, the free energy of Cr, F, requires three contributions to the entropy

$$F(M,V,T) = U - T(S_{\mathrm{mag}} + S_{\mathrm{ele}} + S_{\mathrm{vib}}) \,, \tag{3.1}$$

where M is magnetization, V is volume, T is temperature, U is the internal energy, S_{mag} is the magnetic entropy, S_{ele} is the electronic entropy, and S_{vib} is the vibrational entropy. The S_{vib} gives most of the total entropy at higher temperatures, even in a harmonic model with fixed phonon frequencies, $\{\omega_s\}$ [2]. Phonon frequencies change with volume, and the "quasiharmonic" (QH) approximation assumes that phonon frequencies, $\omega_s(V(T))$, depend on temperature only through thermal expansion. The "anharmonic" (AH) approximation includes an independent change with T, i.e., $\omega_s(V,T)$.

The lattice dynamics of Cr show large anharmonic contributions at high temperatures [9]. Transitions from the antiferromagnetic to the paramagnetic states are

not well understood for Cr [13–17]. It has been suggested that magnetic fluctuations exist above 1000 K [16, 18]. These issues of magnetism and anharmonicity continue to drive work on the high-temperature thermodynamics of Cr. Calorimetric (JANAF) measurements and third-generation CALPHAD models provide values for the total entropy of Cr, $S_{tot}(T)$ [19, 20], but not the individual components of Eq. 3.1.

Here we use time-of-flight (TOF) inelastic neutron scattering (INS), Born-von Kármán (BvK) analyses, temperature-dependent effective potential modeling, and non-spin-polarized density functional theory (DFT) to determine the individual contributions S_{vib}, S_{ele}, and S_{mag}, from 330 to 1493 K. Our AH calculations, which include contributions from electrons and phonons, largely account for the values of $S_{tot}(T)$ observed with recent calorimetry measurements and match observed lattice expansion. The QH approximation also gives a vibrational entropy close to that observed with TOF INS, but this success is caused by a canceling effect of individual phonon branches. The BvK analyses of TOF data support AH phonon branch behavior. A comparison of TOF INS and anharmonic calculations reveals that AH computations capture most, but not all, experimentally observed phonon behavior. This additional nonharmonic behavior is unexplained but is not explicitly magnetic in origin. In summary, we find that temperature-broadened electronic and third-order anharmonic contributions reproduce experimental thermodynamic measurements well, and no purely magnetic interactions are needed to explain the thermodynamics of Cr above 330 K.

3.2 Methods

Inelastic neutron scattering

Inelastic neutron scattering (INS) measurements were performed on electrochemically deposited plates of polycrystalline 99.995% Cr purchased from Alfa Aesar. Two pieces of Cr that gave a large area for scattering were secured inside a niobium foil sachet surrounded by a frame of boron nitride[1]. All data were taken at the time-of-flight wide Angular-Range Chopper Spectrometer (ARCS) at the Spallation Neutron Source (SNS) at Oak Ridge National Laboratory (ORNL) [21]. The incident energy was 70 meV using Fermi chopper 2 at a frequency of 420 Hz and the T_0 chopper at 90 Hz. This gave a resolution of 2.9 meV at the elastic line. Sample temperatures varied from 6-1493 K. Below 330 K, a closed-cycle helium refrigerator was used. For measurements at higher temperatures, samples were

[1] Hillary L. Smith prepared the sample sachet described here.

transferred to the high-temperature MICAS furnace [22]. Data were reduced to phonon density of states (DOS) curves by subtraction of an empty Nb sachet and were corrected for multiphonon scattering with Mantid and the Multiphonon package [23, 24]. Integration to produce the phonon density of states was performed for values of 3.5 $Å^{-1}$ < Q < 10 $Å^{-1}$, where magnetic scattering contributes less than 1.5% of the total scattering. This ensured that the scattering intensity used to obtain the density of states was vibrational in origin. Additional corrections to account for sample curvature were performed in MCViNE [25] (see the Neutron Simulations with MCViNE section (3.6) of the Supplemental Material [26]) for more details).

Born-von Kármán Analysis

Analyses of TOF INS DOS were performed using the Born-von Kármán (BvK) model [27]. This model takes a crystal to be a set of nuclear masses whose interactions act like springs that provide restoring forces against the displacements of nuclei. By transforming the forces associated with these displacements into a dynamical matrix, the BvK model has often been used to fit phonon dispersions. Fitting phonon DOS spectra with the BvK model is more involved because the DOS are aggregates of all phonon modes in reciprocal space. To address this challenge, trial force constants[2] were used to construct a dynamical matrix, $D(\vec{q})$, using the underlying symmetries of the crystal lattice. A sufficiently dense set of q-points in the first Brillouin zone was used to collect the spectrum of phonon frequencies, ω, for each temperature:

$$M\omega^2\vec{\epsilon} = D(\vec{q})\vec{\epsilon}, \tag{3.2}$$

where M is the mass of the atom and $\vec{\epsilon}$ is the polarization of the phonon mode corresponding to reciprocal space vector $\vec{q}$. This BvK model was embedded in a genetic algorithm global optimization framework, where trial sets of force constants were generated randomly according to the differential evolution algorithm [28]. Each optimization was repeated several times to ensure convergence. The resulting DOS are compared with experimental data. For Cr, a BvK model including atomic interactions through the second nearest neighbors (four tensorial force constants) was found to be sufficient. More details of the fitting process are in the Tensorial and radial force constants portion (3.6) of the Supplemental Material [26].

[2] Trial force constants are calculated using uncorrelated supercell configurations generated from a canonical ensemble informed by the Debye temperature.

Computation

All density functional theory (DFT) calculations were performed with the Vienna *Ab Initio* Simulation Package (VASP) [29–31]. Plane-wave basis sets with a kinetic energy cutoff of 600 eV and projector-augmented-wave pseudopotentials [32, 33] were used with Perdew-Burke-Ernzerhof (PBE) exchange-correlation functionals [34, 35]. Each calculation used a 6×6×6 supercell consisting of 216 atoms. Monkhorst-Pack [36] k-point meshes of $4 \times 4 \times 4$ and $8 \times 8 \times 8$ were used for vibrational and electronic supercell calculations, respectively. We performed spin-polarized DFT calculations at 1000 K from initial paramagnetic, ferromagnetic, and antiferromagnetic spin configurations. Upon convergence, the magnetic polarizations in all cases were less than $0.08\,\mu_B$ on individual atoms and less than $0.05\,\mu_B$ in the orientational averages of spins. Calculations were performed for positive and negative dilations of the lattice, with no notable effect on the converged magnetic polarization. To balance computational cost with supercell size and complexity, non-spin-polarized calculations were used for the phonon dynamics.

Quasiharmonic

Phonon calculations within the quasi-harmonic approximation were conducted with Phonopy [37]. A finite atomic displacement was introduced into each supercell of a grid of minimized 0 K supercells scaled by $\pm 0.5\%, \pm 1\%, \pm 1.5\%$ volume. Static calculations of each were converged to within 10^{-7} eV for accurate force constant determination. The harmonic approximation from $T = 0 - 1500$ K was applied to each volume, and a grid of these free energy curves were fit to a Birch-Murnaghan equation of state. The minimized volumes at 330, 1000, and 1500 K were used to create corresponding dynamical matrices and predict phonon properties. A q-point mesh of $70 \times 70 \times 70$ was necessary for proper convergence, and the calculated phonon DOS were convoluted with a Gaussian of 1.0 meV to approximate the broadening at higher phonon energies from the instrumental resolution. Lattice and thermodynamic properties calculated within this approximation depend on temperature only through a volume mapping, $\omega = \omega(V(T))$. More details on this process are provided in the Supplemental Material (see 3.6) [26].

Anharmonic

Anharmonic contributions to thermodynamic properties were calculated using the stochastic Temperature Dependent Effective Potential Method (sTDEP) [38]. In

this procedure, the Born-Oppenheimer surface of a material at a given temperature is represented using a collection of static calculations on supercells of thermally displaced atoms. These displacements were generated by a stochastic sampling of a canonical ensemble at the temperature of interest. The energies, forces, and displacements of each configuration were tabulated and used to generate force constants with a least squares fit to a model Hamiltonian,

$$\mathcal{H} = U_0 + \sum_i \frac{p_i^2}{2m_i} + \frac{1}{2!}\sum_{ij\alpha\beta} \Phi_{ij}^{\alpha\beta} u_i^\alpha u_j^\beta + \frac{1}{3!}\sum_{ijk\alpha\beta\gamma} \Phi_{ijk}^{\alpha\beta\gamma} u_i^\alpha u_j^\beta u_k^\gamma, \tag{3.3}$$

where $u_{\{i,j,k\}}$ is the displacement of atom $\{i,j,k\}$ and α,β,γ are the Cartesian components. The temperature-dependent U_0 is a fit parameter for the baseline of the potential energy surface. The sum containing Φ_{ij}, the quadratic force constants, captures some anharmonic and electron-phonon effects at a given temperature, and the final sum includes phonon-phonon interactions through the cubic force constants, Φ_{ijk}. The latter two terms in the model Hamiltonian are used to calculate anharmonic shifts and broadenings of phonon modes with respect to temperature. The force constants computed with this method include explicit temperature and volume dependencies.

A grid of 36 volumes and temperatures was created. For each point on the grid, an ensemble of ten supercells was generated with stochastically-displaced atomic positions. DFT calculations were performed on each supercell to obtain energy-force-displacement data. The resulting energies were fit to the Birch-Murnaghan equation of state to find the optimized volume for a given temperature. This volume and the calculated force constants were used to create another set of configurations on the temperature volume grid, and the minimization process was repeated. In this way, the force constants are numerically converged with respect to the number of configurations and supercell size. The final minimized free energies were utilized to calculate the equilibrium volume at each temperature, and phonon properties were evaluated at these conditions. Renormalization of phonon frequencies due to anharmonicity was included in these evaluations. Using phonon self-energy corrections from many-body theory [27, 39], $\sum(\vec{\Omega}) = \Delta(\vec{\Omega}) + i\Gamma(\vec{\Omega})$, shifts and broadenings of the phonon DOS were calculated. Further details are provided in the Anharmonic Calculations section (3.6) of the Supplemental Material [26].

3.3 Results

Phonon densities of states (DOSs) from TOF spectra of Cr are shown in Fig. 3.1. Shifts of the phonon DOSs from 6-1493 K follow the expected trend of "softening," or reduction of energy, with an increase in temperature. Interestingly, above 600 K, the three defined mode peaks (low transverse, T_2, high transverse, T_1, and longitudinal, L) appear as two peaks. This is traced to a large thermal softening of approximately 8 meV of the high transverse mode between 6 and 1493 K.

Figure 3.2 shows the temperature dependence of the phonon dispersions between 6-1493 K, obtained by fitting the experimental DOSs to a BvK model [28]. We performed fits iteratively using a genetic algorithm optimization [40] (see 3.2). Along the $\Gamma \rightarrow H \rightarrow P \rightarrow \Gamma$ pathway, the transverse modes are degenerate and exhibit a similar softening as the longitudinal mode. From $N \rightarrow \Gamma$, there is a branch-dependent decrease in energy with respect to temperature. We illustrate these shifts relative to 330 K at each high symmetry point in Fig. 3.3. The largest softening (of approximately 17%) occurs in the high transverse mode between 330-1493 K. This behavior is consistent with the DOSs of Fig. 3.1.

Figure 3.4 shows the calculated and experimental DOS at 330, 1000, and 1500 K. Colored bars representing mode peaks fit to three Lorentzians show the average shift of each feature. Densities of states calculated with sTDEP show similar peak location, shape, and softening to the experimental spectra at 330 and 1500 K. Our quasi-harmonic predictions do not accurately reproduce the features in the DOS at these temperatures, indicating that anharmonicity is important for the thermal trends of phonons in Cr.

Our experimental and calculated phonon dispersions at 330, 1000, and 1500 K are plotted in Fig. 3.5. Quasi-harmonic and anharmonic calculations agree well with experimental data along most of the high-symmetry reciprocal space pathways. A notable exception is the $N \rightarrow \Gamma$ direction, where the QH low transverse modes show an anomaly at the N point, and the high transverse modes do not shift as strongly as expected. The AH and QH calculations also give different magnitudes of the longitudinal mode along the $\Gamma \rightarrow H$ path.

A way to assess the thermodynamic consequences of anharmonic phonon behavior is by calculating entropy. Figure 3.6 shows the electronic, vibrational, and electron-phonon components of entropy and their respective contributions to the total entropy as determined by JANAF [19].

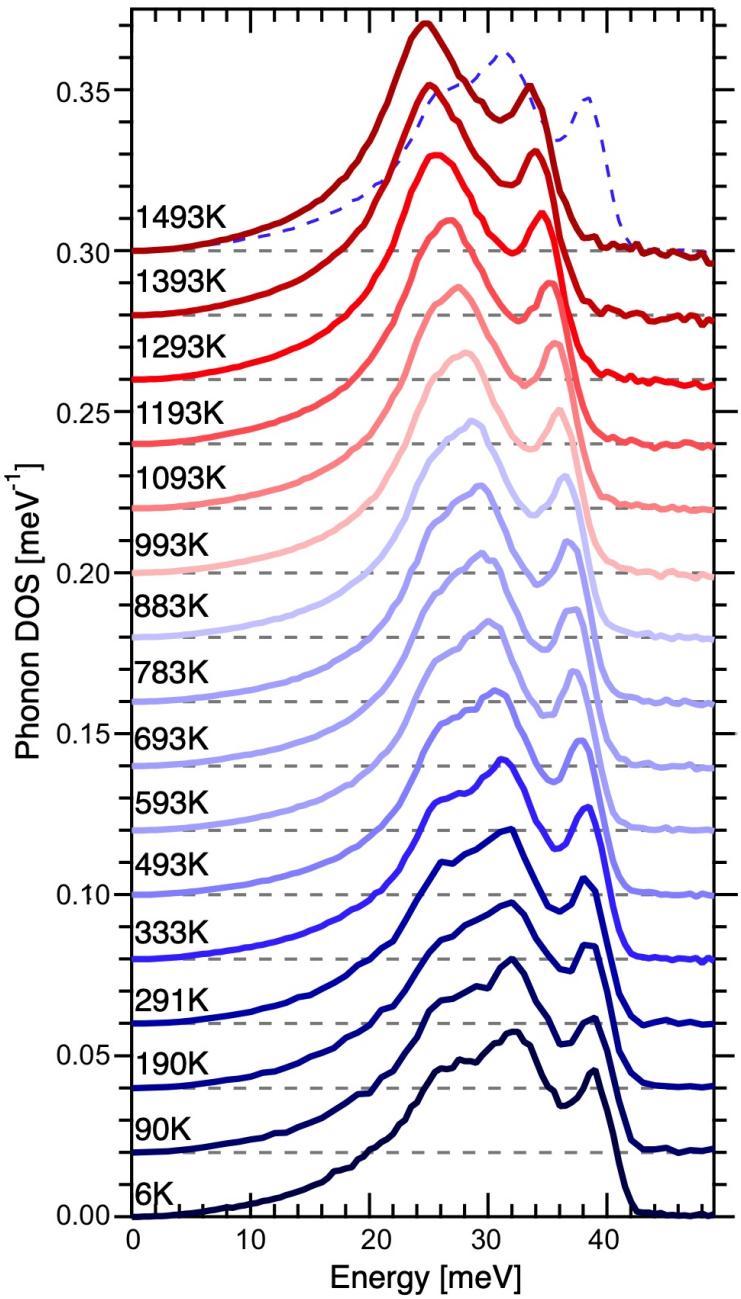

Figure 3.1: Cr phonon DOSs from 6-149 K measured by TOF. Curves are offset for clarity, and the 333 K dataset is overlaid with the 1493 K curve to show the magnitude of the shift between 333 and 1493 K. Experimental error bars (based on counting statistics) are not shown because their height is approximately the width of the line used to connect data points.

The calculated lattice expansions are compared to experimental results in Fig. 3.7. Both QH and sTDEP *ab initio* calculations are in agreement with lattice parameters

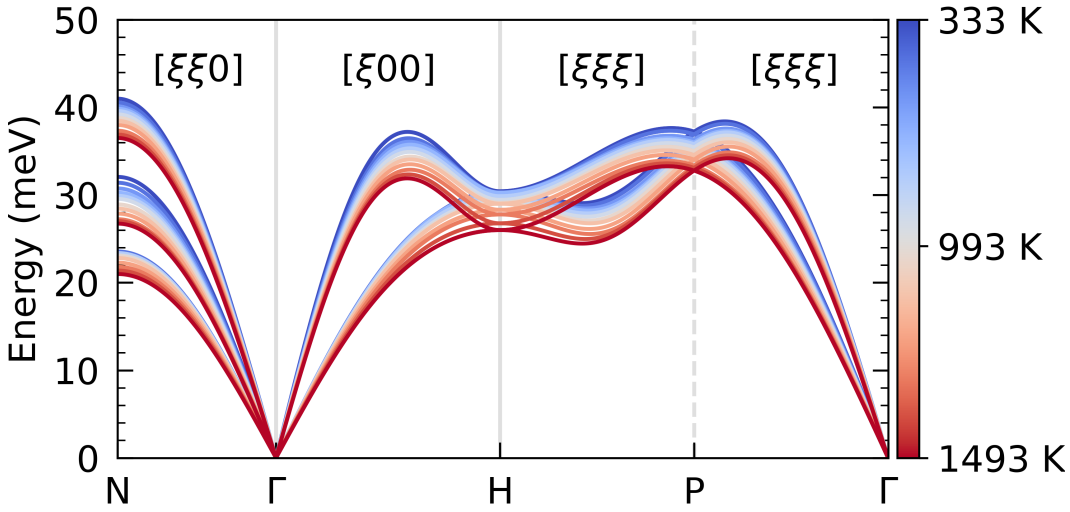

Figure 3.2: Phonon dispersion relations from force constant optimization of BvK fits of the experimental phonon DOSs (333-1493 K). Two nearest neighbors (four variables) were considered in the fit.

obtained from the elastic region of our neutron scattering measurements, and with previous experimental results that are labeled in the figure.

3.4 Discussion

Phonons

The experimental phonon DOSs of bcc Cr show significant softening at elevated temperatures, and the apparent disappearance of one of the Van Hove singularities in Fig. 3.1 is a result of this temperature dependence. Phonon dispersions calculated with fitted force constants show that the largest softening occurs in the high transverse mode. At the high symmetry points, Γ, H, and P, the two transverse branches are degenerate. At the N point near 1000 K, Fig. 3.3 shows a softening of the high transverse (T_1) mode and little softening of the low transverse (T_2) mode. The shift of the high transverse mode from ~32 to ~27 meV confirms that features in the phonon DOS with the largest thermal softening are associated with the $T_1[\xi,\xi,0]$ phonon branch. At the N point, this T_1 mode involves the opposing displacements of two neighboring (110) planes along the $[1\bar{1}0]$ direction [41]. The relatively small thermal softening of the low transverse mode, $T_2[\xi,\xi,0]$, up to 1000 K also may originate from interactions beyond the harmonic approximation.

At 330 K, the high transverse and longitudinal modes in the DOS have higher energies in the QH calculations than from TOF measurements and anharmonic sTDEP calculations. This overestimation of peak locations continues to 1500 K.

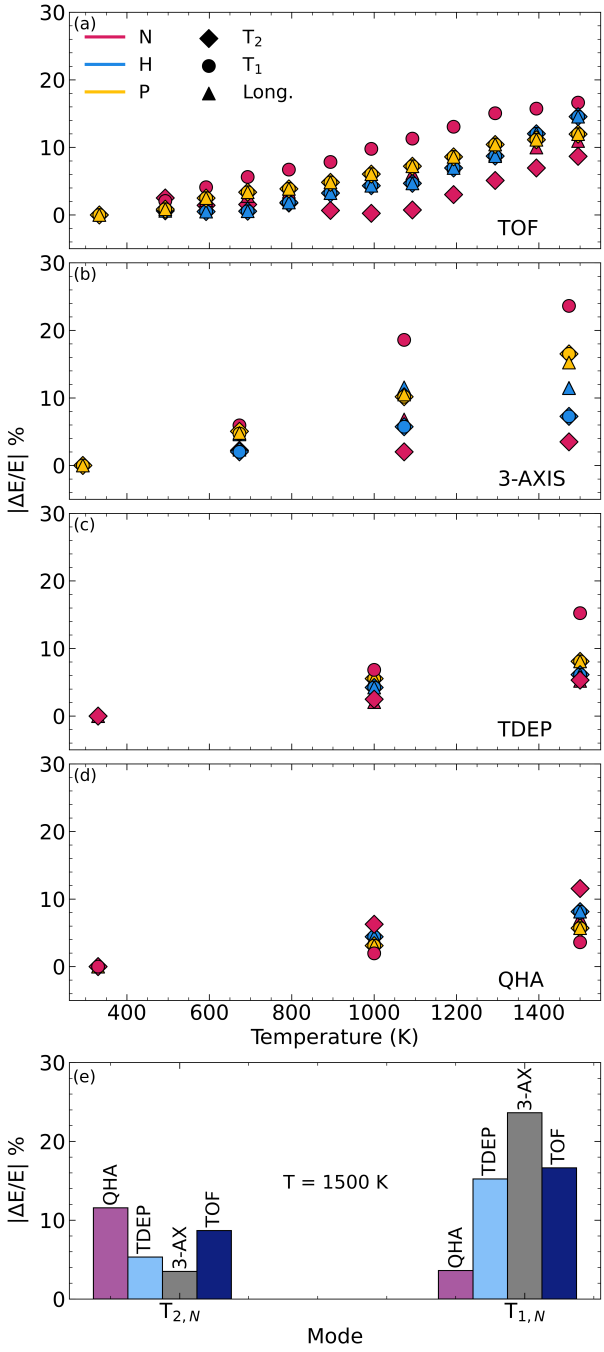

Figure 3.3: Thermal shifts, relative to ambient temperature, of the phonons in Cr at each non-Γ high symmetry point for a) our TOF measurements, b) previous triple axis experiments [41], c) AH calculations, d) and QH calculations. A comparison of the thermal shifts for each method at 1500 K for the T_1 and T_2 modes at the N point is shown in e).

Consequently, the shape of the DOS is skewed in the QH approximation, with more features appearing at higher energies than those found with measurements

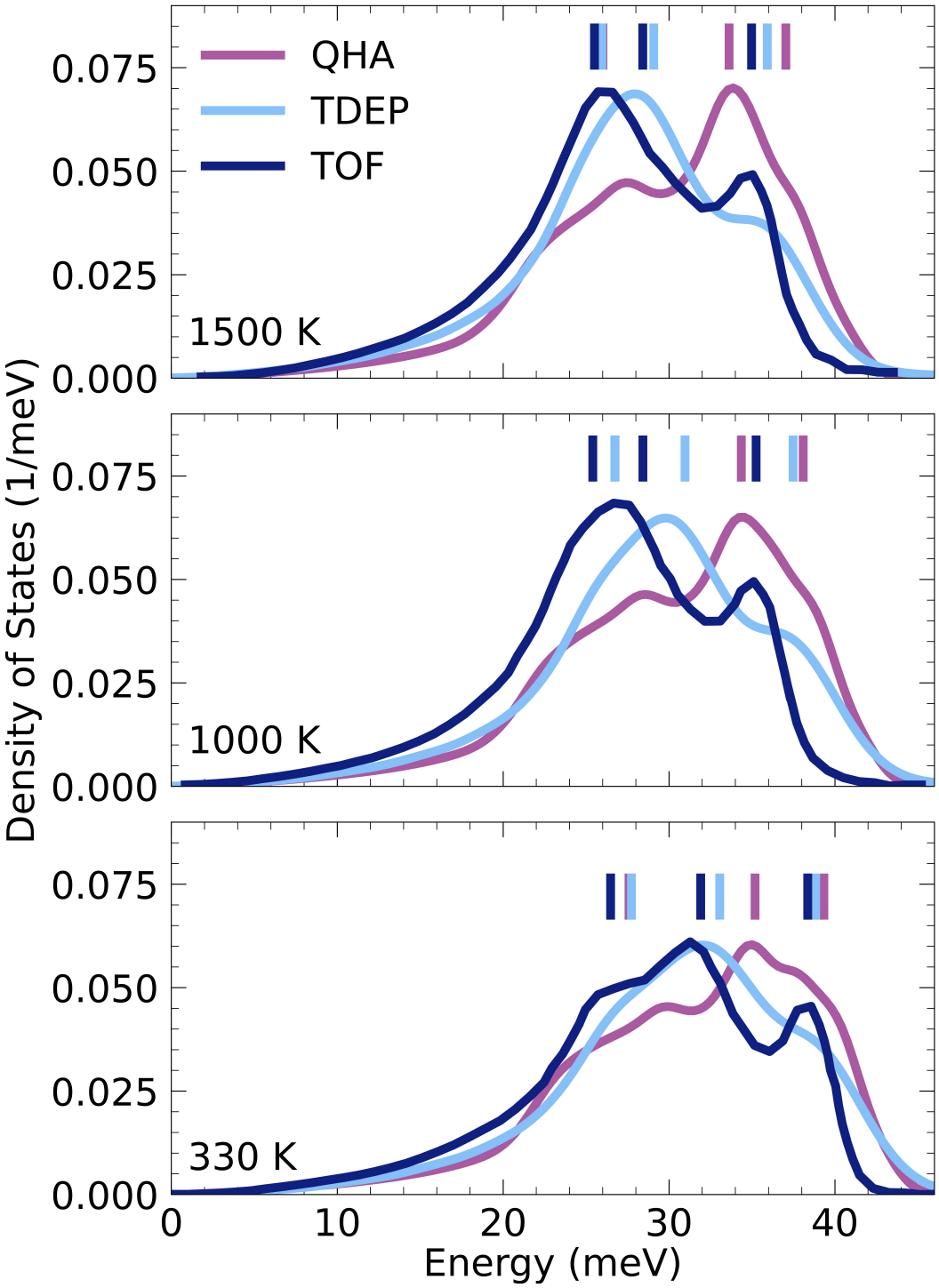

Figure 3.4: Phonon densities of states at 330 (bottom), 1000 (middle), and 1500 K (top). Each panel compares the experimental phonon DOS (dark blue) to the calculated DOSs from quasi-harmonic (purple) and anharmonic (light blue) approximations. The colored markers indicate peak locations from a Lorentzian fit to the features of the DOSs.

and sTDEP calculations. The agreement of the DOS calculated with the AH approximation and TOF measurements is excellent at 330 and 1500 K, despite some excessive broadening of the longitudinal Van Hove singularity.

There is a general agreement of phonon dispersions calculated with each model and experimental data at 330, 1000, and 1500 K along $\Gamma \rightarrow H \rightarrow P \rightarrow \Gamma$ (Fig. 3.5). However, the QH approximation inverts the energies of the T_1 and T_2 modes at the N point. This is accentuated by the anomaly in the low transverse branch behavior at N in the QH dispersions. This discrepancy is better seen with Fig. 3.3e. In the QH approximation, the low transverse branch shows the largest thermal softening at N. This disagrees with the general trend seen in the experimental data and AH calculations: the high transverse phonon branch has the larger thermal softening. Quasiharmonic models sometimes predict accurate macroscopic properties without capturing the underlying phonon physics [44, 45].

We attribute the failure of the QH approximation in Cr to the underlying assumption of noninteracting phonons. This assumption is known to fail at higher temperatures, where temperature-dependent phonon-phonon interactions begin to dominate [2, 46–48]. The QH model cannot capture these effects because the frequencies within this model, $\omega = \omega(V(T))$, incorporate temperature by shifting harmonic frequencies with changes in volume. This approach ignores terms beyond the quadratic phonon self energy, which are needed for lifetime broadening and purely temperature-dependent (AH) shifts. Our sTDEP calculations include cubic order corrections of the phonon-self energy, so $\omega = \omega(V, T)$.

The QH approximation did not successfully predict the thermal softenings of individual phonons, but there is reasonable agreement between the vibrational entropy calculated with QH and AH methods. The change in phonon frequency at the N point gives insight into why. Summing the fractional thermal shifts ($T_1 + T_2 + L$) from the QH calculations at the N zone boundary gives a change of about 22%. A similar sum for our AH calculations gives a change of 26%, which is comparable. This shows some cancellation of errors in the average behavior of phonon branches from the QH calculations, giving them better success with the vibrational entropy.

Likewise, a good prediction of thermal expansion does not validate the QH approximation for predictions of phonon physics. Using

$$\frac{\partial^2 F}{\partial V \partial T} = -\beta B_T \tag{3.4}$$

and $F(V,T) = U(V,T) - TS(V,T)$, it is evident that thermal expansion, β, and bulk modulus, B_T, are explicitly dependent on both volume and temperature. Any cancellation of errors introduced in calculated entropy will be present in predictions of thermal expansion (and bulk modulus). It is therefore plausible that the QH approximation can successfully reproduce the thermal expansion of Cr (Fig. 3.7), even with the wrong thermal trends of individual phonons.

There is an underestimation of 4% in the sTDEP vibrational entropy at 1500 K, illustrated in the middle panel of Fig. 3.6. This is caused by an overbinding in the generalized gradient approximation (GGA) for Cr [49], which also affects our ground state lattice parameter (a = 2.845Å). This is consistent with the ~4% average over-stiffening of the phonon dispersions (Fig. 3.5), and the slight underestimation of the lattice expansion (Fig. 3.7). A similar effect occurs in our QH calculations.

Entropy and free energy

The top panel in Fig. 3.6 shows that for temperatures up to 600 K, the phonon entropy from TOF INS experiments accounts for nearly all of the total entropy [19]. At 1500 K, the S_{vib} from TOF measurements or calculations accounts for over 89% of the total entropy of Cr. The remainder originates primarily from the occupancy of electronic states, the change of these states with temperature, and perhaps magnetic entropy [16, 18].

Figure 3.6 shows that an electronic entropy S_{ele}, calculated first by including the temperature dependence of the electronic entropy through the Fermi-Dirac distribution with the ground state electronic states, brings the sum of entropies S_{tot} closer to the JANAF thermodynamic data, where

$$S_{\text{tot}} = S_{\text{vib}} + S_{\text{ele}} + S_{\text{mag}} \ . \tag{3.5}$$

Thermal motions of atoms broaden the electronic states through electron-phonon interactions. This temperature dependence was calculated with supercells consisting of thermally displaced atoms obtained by sTDEP at 330, 1000, and 1500 K, and is shown in Fig. 3.6. The electronic entropy was also calculated by the simpler

process following Thiessen [50] and Grimvall [51], where the ground state electronic DOS, $\rho_{\mathrm{gnd}}(E)$, is convoluted with a function of Lorentzian form

$$\rho(E) = \rho_{\mathrm{gnd}}(E) * \mathcal{L}(2\Gamma) \,, \tag{3.6}$$

to approximate the effects of electron-phonon interactions on electronic DOS, $\rho(E)$. The amount of broadening, $2\Gamma = 2\pi\lambda k_{\mathrm{B}}T$, used a value of $\lambda = 0.5$ [52]. Figure 3.6 shows very good agreement between these two approaches.

Adding the thermally-broadened S_{ele} to the experimental and computational S_{vib} gives our best estimates of the total entropy of bcc chromium. Figure 3.6 shows that the sum of the measured TOF vibrational and electronic components gives excellent agreement with the JANAF data from calorimetric measurements. There is, however, something missing from the anharmonic phonon calculations, as seen by the inset at the top of Fig. 3.6. A similar discrepancy was found in previous anharmonic calculations [18], which proposed that the extra entropy required for agreement with calorimetry was magnetic in origin. However, the experimental phonon entropy is larger than these anharmonic calculations, and with the electronic entropy, the total entropy agrees well with calorimetry. The discrepancy is in the anharmonic calculations of the phonon DOS, which are stiffer and give a lower phonon entropy than the measurements. The additional non-harmonic contribution to the phonon self-energy is unexplained, but an effect from phonon-paramagnon interactions could be a candidate. Paramagnon energies were calculated recently by time-dependent density functional theory at 0 K [53]. These energies were found to be large, and may not change strongly with temperature. Showing the effects of paramagnons on phonon energies at high temperatures may require new computations. Nevertheless, a large, explicit contribution from magnetic entropy is not needed to account for the thermodynamic entropy of Cr at high temperatures.

3.5 Conclusions

The phonon DOS was measured on bcc chromium from 6 to 1493 K by TOF INS, and calculations of the phonons were performed with QH and AH approximations using Phonopy and sTDEP. To obtain detail on individual phonon branches, the experimental DOS were fit to a Born-von Kármán model using force constants adjusted with a global minimizer. Both measurements and computations showed significant thermal softening of the phonons, and a similar average phonon softening. However, the QH approximation predicted that the low transverse branch

would soften faster than the high transverse branch, whereas the opposite trend is found by AH sTDEP calculations, and by TOF results from the present work and a previous study. The thermodynamic entropy of chromium was obtained from the experimental phonon DOS, and the electronic entropy from *ab initio* calculations. Their sum gave an entropy for chromium that was in excellent agreement with JANAF results obtained by assessing calorimetric data. An explicit magnetic entropy contribution is not needed for temperatures above 330 K, but a paramagnon susceptibility may perturb phonon energies beyond the known effects of quasiharmonic, anharmonic, and electron-phonon interactions.

3.6 Supplemental Information

Multiple Scattering

The experiment was designed to minimize the effects of multiple scattering. This was achieved by choosing a sufficiently thin sample of Cr. The ratio of double (multiple) scattering to single scattering is

$$1/2\,(t/\tau), \tag{3.7}$$

where t is the sample thickness and τ is the characteristic scattering length of

$$\tau = 1/(\rho\sigma). \tag{3.8}$$

Here $\sigma = 3.5$ barns for the total scattering of a Cr nucleus and $\rho = 8.3 \times 10^{22}$ nuclei/cm^3. For the Cr pieces in this experiment, which were ~0.15 cm thick, the ratio of single to double scattering is 0.022, or 2%. Despite some directions in the sample where the neutron paths were longer, the sample is still thin enough to neglect multiple scattering.

Quasi-harmonic Calculations

Phonon calculations with the quasi-harmonic (QH) approximation used the Phonopy package [37]. The finite difference method was used to generate forces on atoms. Force constant matrices were constructed and transformed into the dynamical matrix,

$$D(\mathbf{q})\mathbf{e}_{\mathbf{q}s} = \omega^2_{\mathbf{q}s}\mathbf{e}_{\mathbf{q}s}, \tag{3.9}$$

where $D(\mathbf{q})$ is the dynamical matrix, $\mathbf{q}$ is the phonon wave vector, s is the phonon band index, $\omega_{\mathbf{q}s}$ and $\mathbf{e}_{\mathbf{q}s}$ are the frequency and polarization vector of the phonon mode with $\mathbf{q}$, s. With all $\{\omega_{\mathbf{q}s}\}$, the vibrational contribution to the free energy is

$$F_{\text{vib}} = \frac{1}{2}\sum_{\mathbf{q}s}\hbar\omega_{\mathbf{q}s} + k_{\text{B}}T\sum_{\mathbf{q}s}\ln\left[1 - \exp\left(-\hbar\omega_{\mathbf{q}s}/k_{\text{B}}T\right)\right]. \tag{3.10}$$

Temperatures from 0-1500 K were considered using a grid of 0 K supercells scaled in volume by $\pm 0.5\%, \pm 1\%, \pm 1.5\%$. The Helmholtz free energy for each volume was calculated and minimized at different temperatures using the Birch-Murnaghan equation of state. Minima of the fitted free energy curves gave the QH volumes at the temperatures of interest. Quasi-harmonic phonon properties were calculated with these volumes. The calculated phonon density of states was convoluted with a Gaussian of 1.0 meV to approximate the broadening due to instrumental resolution.

Anharmonic Calculations

Phonon calculations with the anharmonic (AH) approximation used the stochastic Temperature Dependent Effective Potential Method (sTDEP) [38]. Supercells with displaced atoms were created by stochastic sampling. For a cell of N_a atoms with mass m_i, the atomic positions, $\{u_i\}$, were created using a harmonic normal-mode transformation,

$$u_i = \sum_{s=1}^{3N_a} \mathbf{e}_{is} \langle A_{is} \rangle \sqrt{-2 \ln \xi_1} \sin(2\pi \xi_2), \tag{3.11}$$

where ξ_n are uniformly distributed numbers between 0 and 1 (the Box-Muller transform). The thermal amplitude, $\langle A_{is} \rangle$, of normal mode s with eigenvector $\mathbf{e}_{is}$ is

$$\langle A_{is} \rangle = \frac{1}{\omega_s} \sqrt{\frac{\hbar \omega_s (n_s + \frac{1}{2})}{m_i}} \approx \frac{1}{\omega_s} \sqrt{\frac{k_\mathrm{B} T}{m_i}}, \tag{3.12}$$

where $n_s = (e^{\hbar \omega_s / k_\mathrm{B} T} - 1)^{-1}$ is the thermal occupation of phonon mode s and $\hbar \omega \ll k_\mathrm{B} T$ denotes the classical limit at high temperatures.

Energies and forces from calculations of an ensemble of supercells with thermally displaced atoms were obtained with a least squares fit to a model Hamiltonian. A grid of four temperatures, $\{0, 330, 1000, 1500\}$ K, and nine volumes was created. For each volume-temperature point, ten thermally displaced supercells were stochastically generated using force constants from a model pair potential. Static calculations were performed on each supercell to obtain energy-force-displacement data. Quadratic and cubic force constants were re-generated for each temperature using these data sets. The free energy surface,

$$F(V, T) = U_0(V, T) + F_\mathrm{vib}(V, T), \tag{3.13}$$

for each volume-temperature point was calculated using sTDEP. The baseline, $U_0(V, T)$, and the free energy from lattice vibrations,

$$F_\mathrm{vib} = \int_0^\infty g(\omega) \left\{ k_\mathrm{B} T \ln \left[1 - e^{-\frac{\hbar \omega}{k_\mathrm{B} T}} \right] + \frac{\hbar \omega}{2} \right\} d\omega, \tag{3.14}$$

depend explicitly on volume and temperature. These free energies were fit to the Birch-Murnaghan equation of state to find the optimized volume for a given temperature.

The phonon DOS,

$$g(\omega) = \sum_s \delta(\omega - \omega_s), \tag{3.15}$$

also depends explicitly on volume and temperature.

Shifts, Δ_s, and linewidths, Γ_s, of phonons arise from AH, or phonon-phonon, interactions. To calculate these renormalized frequencies, results from many-body perturbation theory were used. The self-energy correction of phonons is

$$\sum(\Omega) = \Delta(\Omega) + i\Gamma(\Omega), \tag{3.16}$$

where $E = \hbar\Omega$ is a probing energy. Linewidths are obtained from the imaginary component,

$$\begin{aligned}\Gamma_s(\Omega) = \frac{\hbar\pi}{16} \sum_{s's''} &|\Phi_{ss's''}|^2 \\ &\times \{(n_{s'} + n_{s''} + 1)\delta(\Omega - \omega_{s'} - \omega_{s''}) + (n_{s'} - n_{s''}) \\ &\times [\delta(\Omega - \omega_{s'} + \omega_{s''}) - \delta(\Omega + \omega_s - \omega_{s''})]\}.\end{aligned} \tag{3.17}$$

This sum is taken over all possible three-phonon interactions, where $\Phi_{ss's''}$ is the three-phonon matrix element obtained from the cubic force constants.

A Kramers-Kronig transformation was used to get the frequency shifts,

$$\Delta(\Omega) = \frac{1}{\pi} \int \frac{\Gamma(\omega)}{(\omega - \Omega)} d\omega. \tag{3.18}$$

As shown in Eq. 3.16, these shifts are the real part of the phonon self-energy.

Anharmonic phonon densities of states curves were calculated using the real and imaginary parts of the phonon-self energy,

$$g_{\text{anh}}(\omega) = \sum_s \frac{2\omega_s\Gamma_s(\omega)}{[\omega^2 - \omega_s^2 - 2\omega_s\Delta_s(\omega)]^2 + 4\omega_s^2\Gamma_s^2(\omega)}. \tag{3.19}$$

In the limit where $\Delta, \Gamma \to 0$ Eq. 3.19 reduces to Eq. 3.15.

Born-von Kármán modeling

The Born-von Kármán formalism relates interatomic force constants of crystalline solids to phonon frequencies. To solve for phonon frequencies, the interatomic

interactions in the dynamical matrix are truncated to the first few nearest-neighbor interactions. Below is a description of how the force constants are extracted from the DOS of body-centered cubic (bcc) Cr using a genetic algorithm to obtain temperature-dependent tensorial and radial force constants [40].

Genetic algorithm

A genetic algorithm optimization was performed to obtain interatomic force constants from experimental phonon DOS employing the open-source package mystic [54]. To begin, the algorithm was used to generate many candidate solutions called a population. Each population consisted of a potential set of force constants that was randomly generated within a set of reasonable force constant bounds, where

$$K_{1NN} = \begin{pmatrix} 1\mathrm{XX} & 1\mathrm{XY} & 1\mathrm{XY} \\ 1\mathrm{XY} & 1\mathrm{XX} & 1\mathrm{XY} \\ 1\mathrm{XY} & 1\mathrm{XY} & 1\mathrm{XX} \end{pmatrix}, \qquad K_{2NN} = \begin{pmatrix} 2\mathrm{XX} & 0 & 0 \\ 0 & 2\mathrm{YY} & 0 \\ 0 & 0 & 2\mathrm{YY} \end{pmatrix} \tag{3.20}$$

are the first and second nearest-neighbor tensorial force constant matrices. The dynamical matrix was constructed from each population (set of force constants) and used to generate a DOS. These DOS are compared with the experimental DOS, and solutions that best reproduce the experimental DOS (by minimizing the mean squared error) are selected as the parents of the next generation. The parent solutions seeded the next population of potential force constants by selecting random combinations of parent parameters and also introducing random changes, or mutations. Least squares fitting and comparison to experiments were repeated until the population converged on a set of force constants that provided the best fit to the experimental density of states (Fig. 3.8). Throughout this process, solutions that generated negative frequencies were discarded due to their implication of dynamical instability in the lattice. Fully optimized force constants were then used to generate phonon dispersions with q-space resolved information.

Tensorial and radial force constants

Tensorial force constants from the genetic algorithm optimization, previous experiments, and computations are presented in Table 3.1. To visualize the effects

of temperature on nearest-neighbor interactions, each matrix (K_{1NN}, K_{2NN}) was projected onto their respective bond directions (Fig. 3.9). Longitudinal and average transverse force constants are obtained, which describe the forces parallel and perpendicular to the bond direction. The longitudinal force constants are significantly higher than the average transverse force constants. Second nearest-neighbor longitudinal force constants dominate over the first nearest-neighbors, but both show a large decrease with an increase in temperature, as generally expected. The second nearest-neighbor transverse force constants remain relatively constant with temperature, while the first nearest-neighbor average transverse force constants exhibit an unusual temperature dependence.

The radial force constants from the BvK analysis, sTDEP, the QH approximation, and previous experiments are shown in Fig. 3.9. There is good agreement between our TOF INS experiments, previous measurements, and sTDEP calculations. QH calculations predict the nearest neighbor longitudinal force constants to be much lower than the other methods. This approximation also overestimates the values for the nearest neighbor transverse force constants. The inability of the QH approximation to capture the values of the 1NN force constants originates from its drastic underestimation of the ϕ_{1xy} tensorial matrix component (see Table 3.1).

Neutron Simulations with MCViNE

The MCViNE (Monte-Carlo VIrtual Neutron Experiment) software package was used to simulate neutron scattering from a chromium plate measured on the wide Angular-Range Chopper Spectrometer (ARCS) instrument at room temperature and above. MCViNE is a neutron ray-tracing simulation package that tracks the pathway of neutrons through the interaction with instrument optical components, scattering from the sample, interception by the detectors, and reduction to an experimentally equivalent format [25]. The sample was described with a "composite neutron scatterer," which consisted of five rectangular slabs: the Cr sample plate, two thin Nb foils in front and behind the sample plate, and the absorbing BN frame to the left and right of the sample plate. An additional composite neutron scatterer was placed around the sample to simulate scattering from the MICAS furnace and between the sample and furnace. The design and testing of this furnace composite is described elsewhere [22].

The chromium sample is modeled with dimensions matching the sample used in the ARCS experiment and oriented at 45 degrees to the incident beam. Phonon

Tensor Force Constants (N/m)				
Temp. (K)	Φ_{1xx}	Φ_{1xy}	Φ_{2xx}	Φ_{2yy}
293[41]	14.35	6.93	37.70	-0.77
300[55]	13.526	6.487	35.915	-1.564
330^a	14.369	-1.464	-4.460	21.093
330^b	13.878	6.765	43.040	-2.991
334	11.53	8.12	42.78	1.62
493	11.39	8.19	40.28	2.41
592	11.42	8.24	38.62	2.12
673[41]	12.40	9.99	27.52	1.18
693	11.40	8.37	37.38	2.16
894	10.80	8.27	35.88	2.53
993	10.55	8.32	34.55	2.66
1000^a	13.423	-1.108	44.077	-4.254
1000^b	12.678	7.808	38.841	-3.250
1073[41]	11.30	9.45	27.44	-1.30
1093	10.47	8.34	33.55	2.48
1193	9.98	8.29	32.93	2.39
1294	9.61	8.12	31.76	2.23
1394	8.93	7.85	31.79	2.46
1473[41]	11.02	9.60	23.16	-1.31
1495	8.42	7.70	31.61	2.55
1500^a	12.661	-0.823	42.124	-4.108
1500^b	12.004	8.447	34.472	-2.656

Table 3.1: Tensorial force constants from previous experiments [41, 55] and computation. Non-labeled force constants correspond to current measurements, and those labeled *a*, *b*, are Phonopy and sTDEP calculations, respectively.

scattering was simulated for the phonon energies E and momenta Q by starting with a BvK model employing force constants tabulated by Trampenau et al. at 300 K [41]. A polycrystalline average of the phonon scattering was obtained by performing an average of phonon dispersions from all orientations of a single crystal. The simulated inelastic spectra were obtained from 10^9 neutron packets emitted from the moderator and passed through the simulated instrument with chopper settings matching those used in the ARCS experiment. The resulting event-mode NeXus file is reduced identically to the experimental data, using the same data reduction tools [23].

This simulated process revealed the effect of the sample curvature on the $S(Q, E)$ experimental inelastic spectra. The simulation allows for contributions from multi-

phonon scattering and multiple scattering to be turned on or off, allowing isolation of contributions to the $S(Q, E)$ from these effects. After reduction of experimental $S(Q, E)$ to a phonon DOS, an unexpected intensity is observed above the phonon cutoff near 40-45 meV. Based on comparison to the phonon DOS obtained from the simulated plate, this feature is attributed to scattering resulting from the sample curvature. A 2D correction matrix was calculated from the simulated data and applied to the experimental data across the full temperature range. This correction had the effect of eliminating the unexpected intensity above the phonon cutoff.

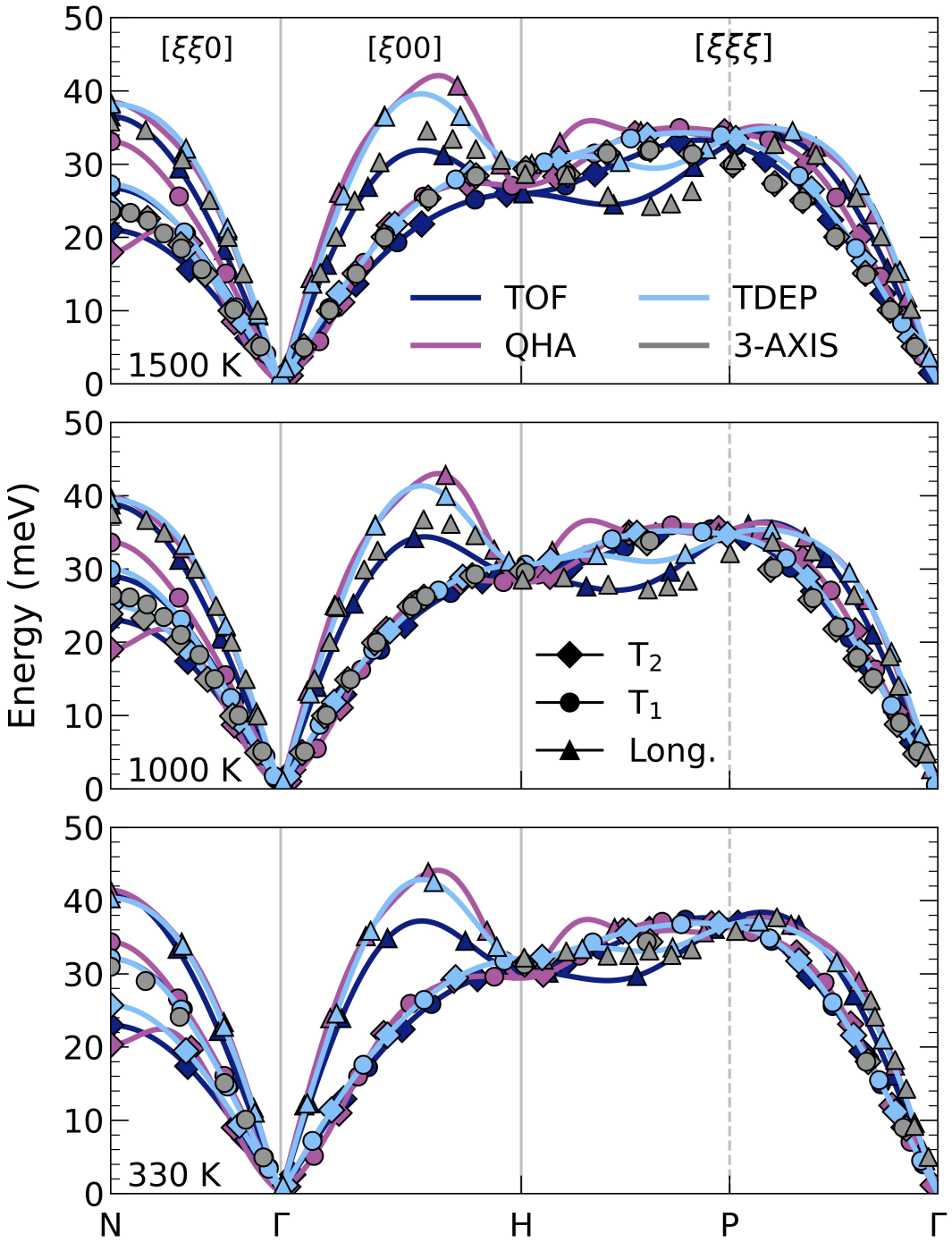

Figure 3.5: Comparison of experimental and calculated phonon dispersion relations at 330K (bottom), 1000K (middle), and 1500K (top). Symbols to distinguish the low transverse (diamonds), high transverse (circles), and longitudinal (triangles) phonon branches are also shown. Anharmonic (light blue) and quasi-harmonic (purple) dispersions are in good agreement with a BvK fit to experimental data (dark blue) and existing triple-axis data (gray) [41]. The anharmonic calculations capture behavior along the H to P high symmetry path better than the quasiharmonic simulations.

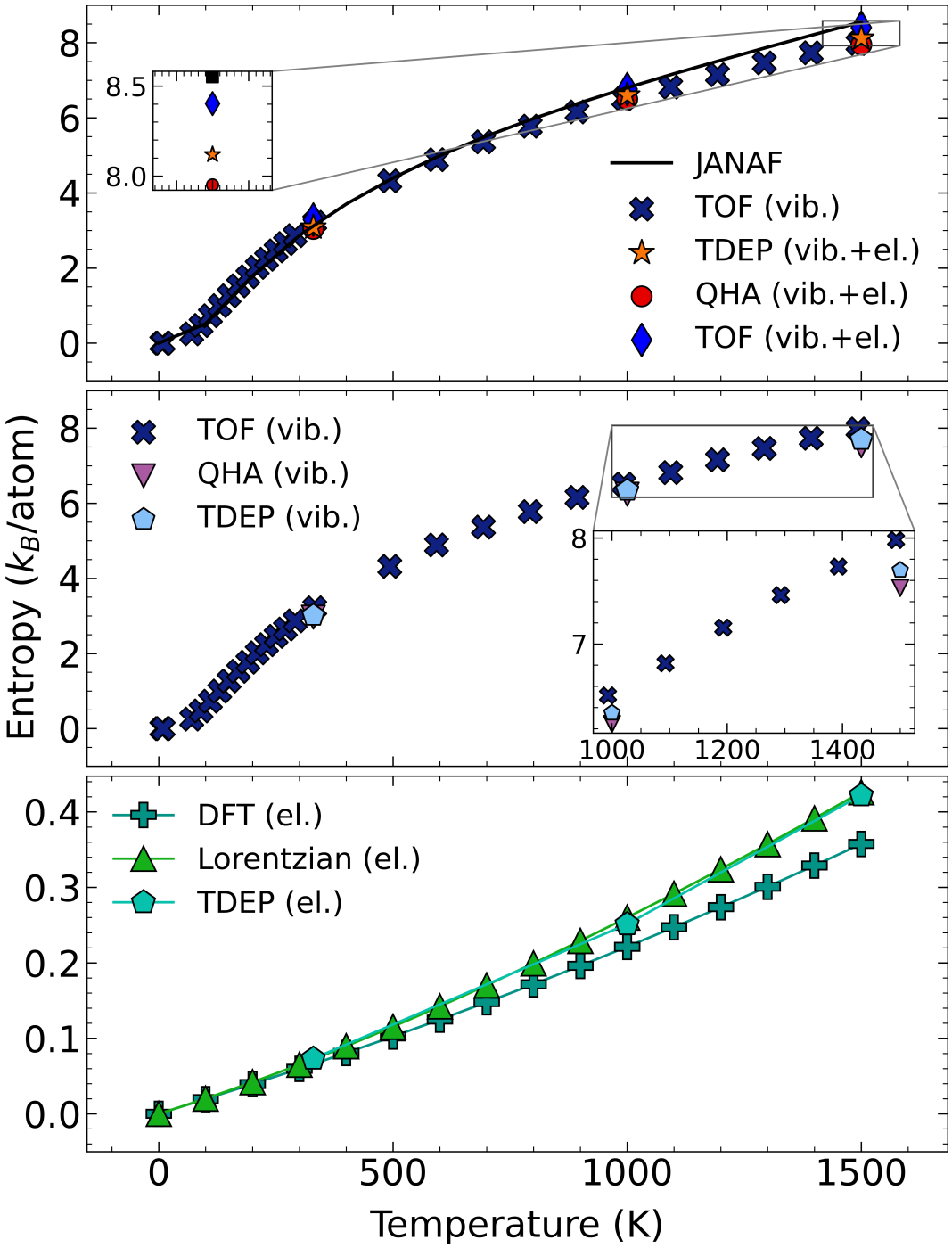

Figure 3.6: Components of entropy compared to the total JANAF entropy [19]. (Bottom) Electronic entropy including temperature-dependent electron-phonon coupling. (Middle) Vibrational entropy calculated from DOSs using TOF INS, a quasi-harmonic approximation, and an anharmonic approximation. (Top) Sum of the electronic and vibrational components of entropy from experiment and computations versus the calorimetric total entropy.

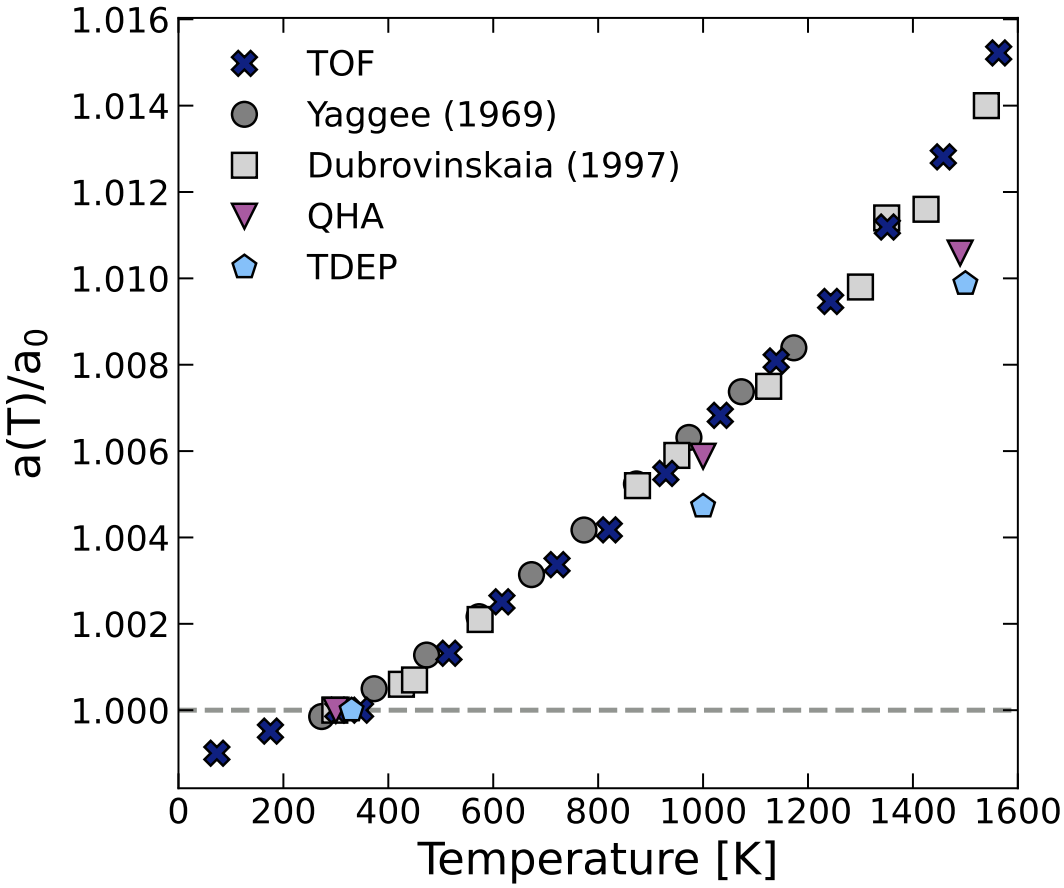

Figure 3.7: Lattice expansion of Cr from 6-1500 K with respect to ambient temperature. Previous lattice expansions are reproduced from [42, 43]

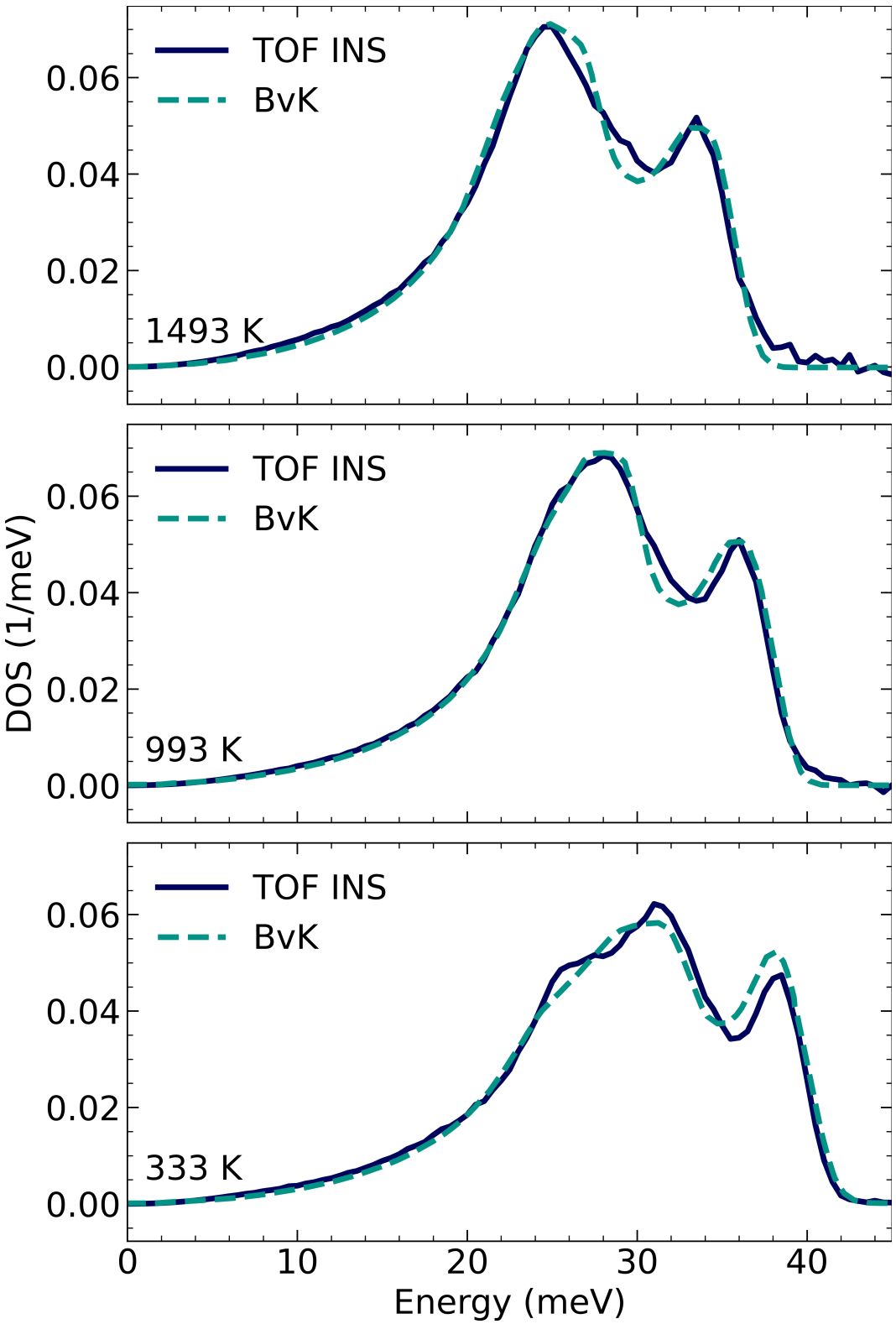

Figure 3.8: TOF INS phonon density of states and the BvK DOS from a second nearest-neighbor fit for 333, 993, and 1493 K. The BvK fit was convoluted with the instrument resolution function.

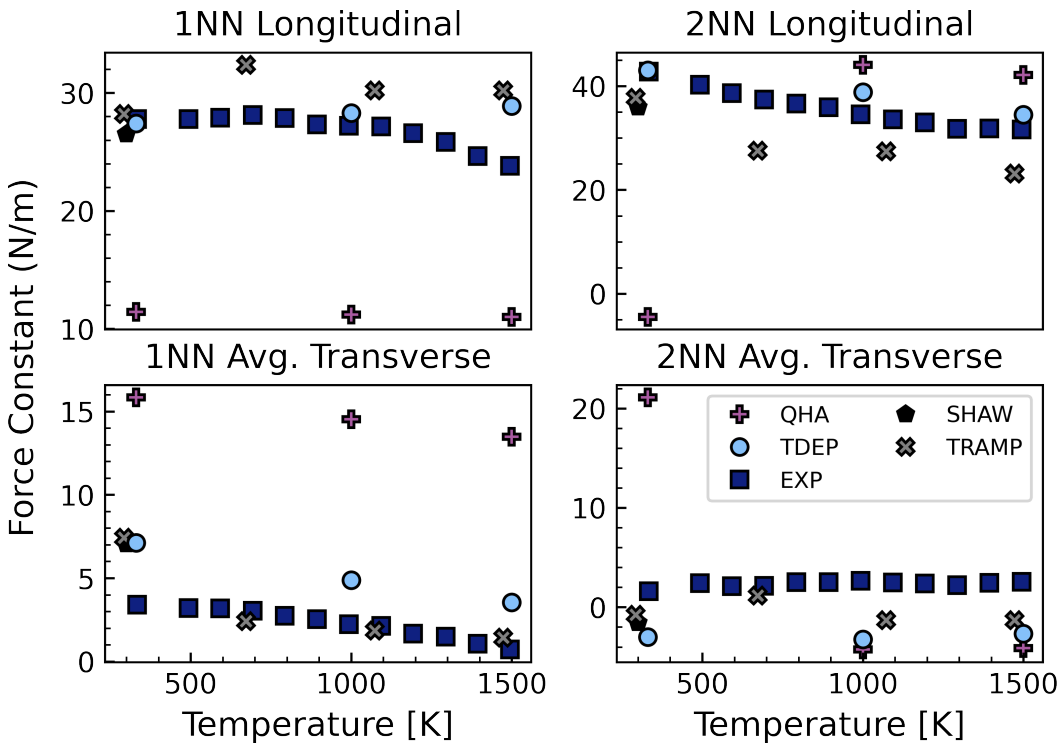

Figure 3.9: Temperature dependence of radial force constants from TOF INS data (squares), TDEP (circles) and QHA (diamonds) calculations, and previous experimental reports (pentagons and crosses) assuming Born-von Kármán boundary conditions. Units for the vertical axis are N/m.

References

[1] C. M. Bernal-Choban, H. L. Smith, C. N. Saunders, D. S. Kim, L. Mauger, D. L. Abernathy, and B. Fultz, Phys. Rev. B **107**, 054312 (2023).

[2] B. Fultz, Prog. Mater. Sci. **55**, 247 (2010).

[3] D. Lamago, M. Hoesch, M. Krisch, R. Heid, K.-P. Bohnen, P. Böni, and D. Reznik, Phys. Rev. B **82**, 195121 (2010).

[4] N. Shulumba, B. Alling, O. Hellman, E. Mozafari, P. Steneteg, M. Odén, and I. A. Abrikosov, Phys. Rev. B **89**, 174108 (2014).

[5] A. R. Natarajan, P. Dolin, and A. Van der Ven, Acta Mater. **200**, 171 (2020).

[6] L. Hao, A. Ruban, and W. Xiong, Calphad **73**, 102268 (2021).

[7] M. Heine, O. Hellman, and D. Broido, Phys. Rev. B **103**, 184409 (2021).

[8] S. Anzellini, D. Errandonea, L. Burakovsky, J. E. Proctor, R. Turnbull, and C. M. Beavers, Sci. Rep. **12**, 6727 (2022).

[9] O. Eriksson, J. M. Wills, and D. Wallace, Phys. Rev. B **46**, 5221 (1992).

[10] L. Néel, Ann. Phys. (Paris) **5** (1936).

[11] M. K. Wilkinson, E. O. Wollan, W. C. Koehler, and J. W. Cable, Phys. Rev. **127**, 2080 (1962).

[12] B. H. Grier, G. Shirane, and S. A. Werner, Phys. Rev. B **31**, 2892 (1985).

[13] K. Thurnay, *Thermal properties of transition metals* (1998), p. 137.

[14] C. Y. Young and J. B. Sokoloff, J. Phys. F: Met. Phys. **4**, 1304 (1974).

[15] J. O. Andersson, Int. J .Thermophys. **6**, 411 (1985).

[16] G. Grimvall, J. Häglund, and A. Fernández Guillermet, Phys. Rev. B **47**, 15338 (1993).

[17] W. Xiong, M. Selleby, Q. Chen, J. Odqvist, and Y. Du, Crit. Rev. Solid State Mater. Sci. **35**, 125 (2010).

[18] F. Körmann, B. Grabowski, P. Söderlind, M. Palumbo, S. G. Fries, T. Hickel, and J. Neugebauer, J. Phys. Condens. Matter **25**, 425401 (2013).

[19] M. W. Chase Jr., *NIST-JANAF thermochemical tables*, 4th edition (Washington, DC: American Chemical Society; New York: American Institute of Physics for the National Institute of Standards and Technology, 1998).

[20] A. Obaied, B. Bocklund, S. Zomorodpoosh, L. Zhang, R. Otis, Z.-K. Liu, and I. Roslyakova, Calphad **69**, 101762 (2020).

[21] D. L. Abernathy, M. B. Stone, M. J. Loguillo, M. S. Lucas, O. Delaire, X. Tang, J. Y. Y. Lin, and B. Fultz, Rev. Sci. Instrum. **83**, 015114 (2012).

[22] J. L. Niedziela, R. Mills, M. J. Loguillo, H. D. Skorpenske, D. Armitage, H. L. Smith, J. Y. Y. Lin, M. S. Lucas, M. B. Stone, and D. L. Abernathy, Rev. Sci. Instrum. **88**, 105116 (2017).

[23] O. Arnold, J. C. Bilheux, J. M. Borreguero, A. Buts, S. I. Campbell, L. Chapon, M. Doucet, N. Draper, R. Ferraz Leal, M. A. Gigg, V. E. Lynch, A. Markvardsen, D. J. Mikkelson, R. L. Mikkelson, R. Miller, K. Palmen, P. Parker, G. Passos, T. G. Perring, P. F. Peterson, S. Ren, M. A. Reuter, A. T. Savici, J. W. Taylor, R. J. Taylor, R. Tolchenov, W. Zhou, and J. Zikovsky, Nucl. Instrum. Methods. Phys. Res. A **764**, 156 (2014).

[24] F. Akeroyd, S. Ansell, S. Antony, O. Arnold, A. Bekasovs, J. Bilheux, J. Borreguero, K. Brown, A. Buts, S. Campbell, D. Champion, L. Chapon, M. Clarke, S. Cottrell, R. Dalgliesh, D. Dillow, M. Doucet, N. Draper, R. Fowler, M. A. Gigg, G. Granroth, M. Hagen, W. Heller, A. Hillier, S. Howells, S. Jackson, D. Kachere, M. Koennecke, C. Le Bourlot, R. Leal, V. Lynch, P. Manuel, A. Markvardsen, R. McGreevy, D. Mikkelson, R. Mikkelson, R. Miller, S. Nagella, T. Nielsen, K. Palmen, P. G. Parker, M. Pascal, G. Passos, T. Perring, P. F. Peterson, F. Pratt, T. Proffen, P. Radaelli, J. Rainey, S. Ren, M. Reuter, L. Sastry, A. Savici, J. Taylor, R. J. Taylor, M. Thomas, R. Tolchenov, R. Whitley, M. Whitty, S. Williams, W. Zhou, and J. Zikovsky, 10.5286/SOFTWARE/MANTID (2013).

[25] J. Y. Y. Lin, H. L. Smith, G. E. Granroth, D. L. Abernathy, M. D. Lumsden, B. Winn, A. A. Aczel, M. Aivazis, and B. Fultz, Nucl. Instrum. Methods. Phys. Res. A **810**, 86 (2016).

[26] See Supplementary Material for more information on experimental design, computational modeling, fitting methods, and corrections for sample curvature.

[27] D. Wallace, *Thermodynamics of crystals*, Dover Books on Physics (Dover Publications, 1998).

[28] L. Mauger, M. S. Lucas, J. A. Muñoz, S. J. Tracy, M. Kresch, Y. Xiao, P. Chow, and B. Fultz, Phys. Rev. B **90**, 064303 (2014).

[29] G. Kresse and J. Hafner, Phys. Rev. B **47**, 558 (1993).

[30] G. Kresse and J. Hafner, Phys. Rev. B **49**, 14251 (1994).

[31] G. Kresse and J. Furthmüller, Phys. Rev. B **54**, 11169 (1996).

[32] G. Kresse and D. Joubert, Phys. Rev. B **59**, 1758 (1999).

[33] P. E. Blöchl, Phys. Rev. B **50**, 17953 (1994).

[34] J. P. Perdew, K. Burke, and M. Ernzerhof, Phys. Rev. Lett. **77**, 3865 (1996).

[35] J. P. Perdew, K. Burke, and M. Ernzerhof, Phys. Rev. Lett. **78**, 1396 (1997).

[36] H. J. Monkhorst and J. D. Pack, Phys. Rev. B **13**, 5188 (1976).

[37] A. Togo and I. Tanaka, Scr. Mater. **108**, 1 (2015).

[38] O. Hellman, I. A. Abrikosov, and S. I. Simak, Phys. Rev. B **84**, 180301 (2011).

[39] A. A. Maradudin, A. E. Fein, and G. H. Vineyard, Phys Status Solidi B Basic Res **2**, 1479 (1962).

[40] L. M. Mauger, PhD thesis (California Institute of Technology, Pasadena, CA, USA, May 2015).

[41] J. Trampenau, W. Petry, and C. Herzig, Phys. Rev. B **47**, 3132 (1993).

[42] F. L. Yaggee, E. R. Gilbert, and J. W. Styles, J. Less-common Met. **19**, 39 (1969).

[43] N. A. Dubrovinskaia, L. S. Dubrovinsky, S. K. Saxena, and B. Sundman, Calphad **21**, 497 (1997).

[44] D. S. Kim, H. L. Smith, J. L. Niedziela, C. W. Li, D. L. Abernathy, and B. Fultz, Phys. Rev. B **91** (2015).

[45] C. N. Saunders, D. S. Kim, O. Hellman, H. L. Smith, N. J. Weadock, S. T. Omelchenko, G. E. Granroth, C. M. Bernal-Choban, S. H. Lohaus, D. L. Abernathy, and B. Fultz, Phys. Rev. B **105**, 174308 (2022).

[46] Y. Shen, C. N. Saunders, C. M. Bernal, D. L. Abernathy, M. E. Manley, and B. Fultz, Phys. Rev. Lett. **125**, 085504 (2020).

[47] T. Lanigan-Atkins, S. Yang, J. L. Niedziela, D. Bansal, A. F. May, A. A. Puretzky, J. Y. Y. Lin, D. M. Pajerowski, T. Hong, S. Chi, G. Ehlers, and O. Delaire, Nat. Commun. **11**, 4430 (2020).

[48] F. Knoop, T. A. R. Purcell, M. Scheffler, and C. Carbogno, Phys. Rev. Mater. **4**, 083809 (2020).

[49] R. Hafner, D. Spišák, R. Lorenz, and J. Hafner, Phys. Rev. B **65**, 184432 (2002).

[50] M. Thiessen, Int. J. Thermophys. **7**, 1183 (1986).

[51] G. Grimvall, *Thermophysical properties of materials* (Elsevier, Amsterdam, 2008).

[52] G. Grimvall, *The Electron-Phonon Interaction in Metals* (North-Holland Publishing Company, 1981).

[53] K. Cao, H. Lambert, P. G. Radaelli, and F. Giustino, Phys. Rev. B **97**, 024420 (2018).

[54] M. M. McKerns, L. Strand, T. Sullivan, A. Fang, and M. A. G. Aivazis, arXiv: 1202.1056 (2012).

[55] W. M. Shaw and L. D. Muhlestein, Phys. Rev. B **4**, 969 (1971).

Chapter 4

THE COMPONENTS OF ENTROPY IN THE LATENT HEAT OF MELTING

4.1 Introduction

Melting is the iconic first-order phase transition where a material changes from a solid to a liquid at the melting temperature, T_m. In thermodynamics, this occurs when the Gibbs free energy [1],

$$G = U - TS + PV, \tag{4.1}$$

of the solid becomes equal to that of the liquid. The energy absorbed at T_m, the latent heat, is defined as $L = T_m \Delta S_{fus}$, where ΔS_{fus} is the entropy of fusion. The definition of L is consistent with the condition $\Delta G = G_l - G_s = 0$, and ΔS_{fus} is from the inequality of $\partial G/\partial T$ for the solid and liquid at T_m.

Predicting T_m has motivated many investigations [2–5]. One of the most well-known ideas is the Lindemann criterion, which is that melting occurs when the square root of the mean-squared atom displacement reaches approximately 10% of the interatomic distance [6]. While it has had some success, this criterion is based on the solid phase alone [7–9]. An effort to include the thermodynamics of the liquid in this criterion was attempted, with mixed results [10]. Recent advances in computational methods [11, 12] have allowed for increasingly accurate melting temperature predictions for various materials [13–15].

Despite the increase in the number and accuracy of melting temperature predictions, work remains to understand the thermodynamics of melting using atomic-scale contributions to ΔS_{fus}. To date, a common "rule" for the entropy of fusion is the empirical Richard's rule, which states $\Delta S_{fus} \approx 1.1 k_B$/atom for monatomic systems [16]. Elements that do not have entropies of fusion near this value are considered to melt "anomalously" (see Fig. 4.1) [17]. Recently, efforts to explain these anomalies have implied a separation of the entropy of fusion into three components from changes in atomic vibrations, configurations, and electronic excitations [18–20]

$$\Delta S_{fus} = \Delta S_{fus,vib} + \Delta S_{fus,config} + \Delta S_{fus,el}. \tag{4.2}$$

Experimentally quantifying these atomic components of the entropy of fusion remains a challenge. However, methods that measure the dynamic response function, such as neutron or x-ray scattering, show promise for identifying and analyzing vibrational motion in liquids [21–23]. In solids, analysis of the vibrational, and to some degree, configurational, components are well-established using these techniques [24–26]. Analysis of the liquid state is more difficult due to the quasielastic ($\varepsilon \approx 0$ meV) scattering from diffusion, which shows up as a broadening of the elastic peak because the self-diffusion of atoms occurs on relatively long time scales. This obfuscates the vibrational spectra in the low-energy regime due to the intersection of time scales (and therefore energies) between atomic vibrations and transitions in or around their instantaneous potential. In fact, most neutron studies on liquid dynamics focus on self-diffusion and pair-based cluster distributions. Only lately have significant advances in instrument resolution and flux allowed for studies into the vibrational modes in liquids [27–29].

Here, we use these recent advances in experimental and computational methods to quantify the thermodynamic contributions to the entropy of fusion in monatomic systems. We perform time-of-flight (TOF) inelastic neutron scattering (INS) measurements on Ge, Bi, Sn, and Pb, which span the range of total entropies of fusion, to obtain the vibrational entropy across the melt. Our measurements are complemented by molecular dynamics calculations with machine-learning interatomic potentials for Ge, Si, Pb, and Li. To the best of our knowledge, this is the first experimental quantification of the vibrational contribution to melting, and it accounts for most of the "anomalous" deviation from Richard's rule.

4.2 Materials and Methods

Inelastic Neutron Scattering

Inelastic neutron scattering experiments were performed on high-quality polycrystalline granules of Ge (99.999%), Bi (99.997%), Sn (99.99%), and Pb (99.99%) encapsulated in vacuum-sealed quartz tubes. Depending on the neutron cross-section of each element, the inner diameter of the quartz tubes varied from 3-4 mm. Ampules of each material were arranged in parallel and enclosed in a vanadium sachet to provide optimal flux on a large, relatively flat volume. The high-temperature furnace MICAS was used to heat the samples to ~200 K above their melting temperatures, allowing data collection in the solid and liquid phases [30]. Data from an empty sample sachet were collected at the temperatures of interest. All spectra were measured using the time-of-flight direct geometry wide-angular

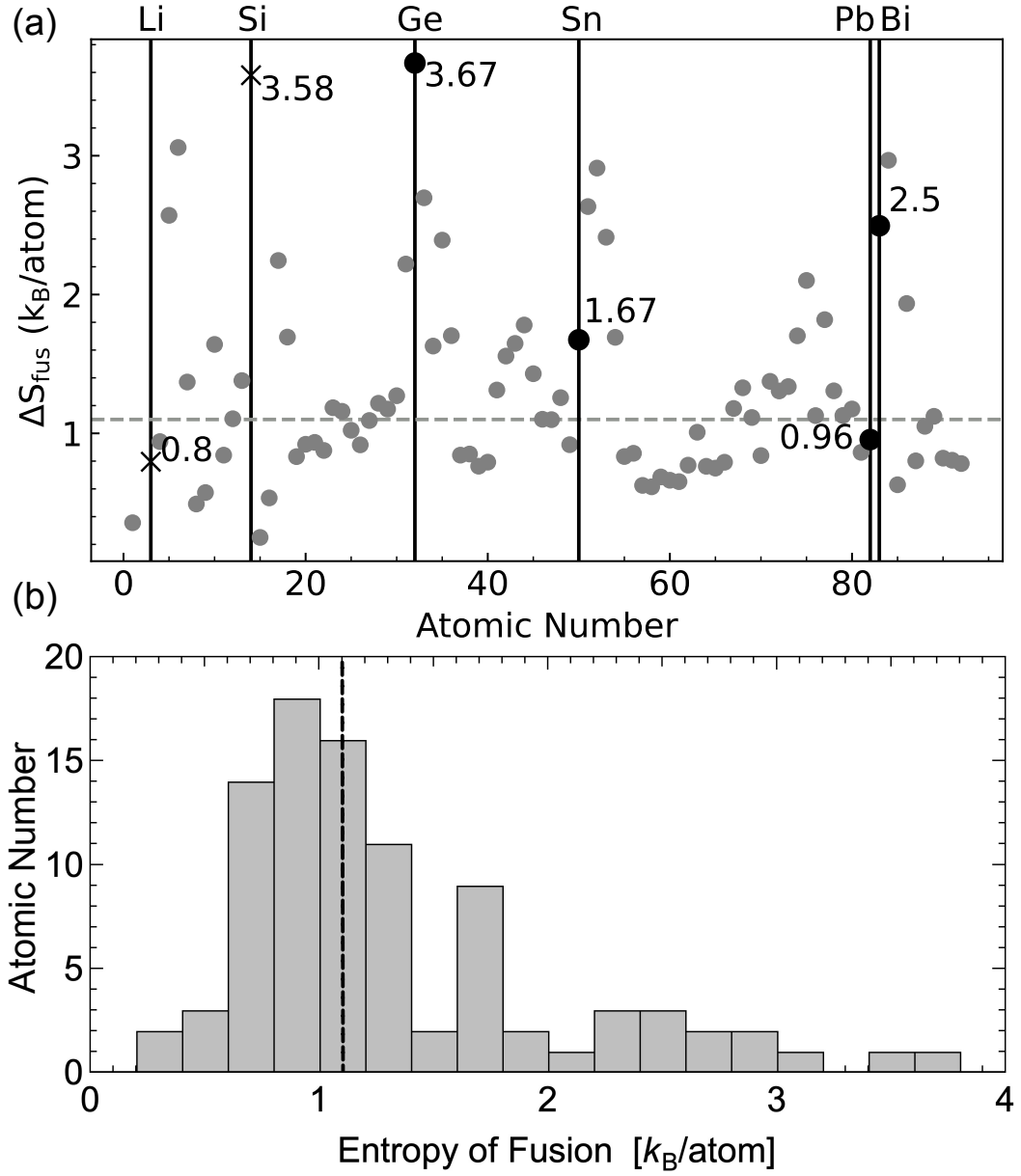

Figure 4.1: Entropies of fusion for elements up to uranium, plotted versus atomic number (a). The elements chosen for this study are indicated by a vertical line and are annotated with the value of their entropy of fusion. Circles (crosses) designate experimentally (computationally) studied elements. (b) Distribution of ΔS_{fus} for the first 92 elements. The dashed lines in (a) and (b) show Richard's rule of $1.1 k_{\text{B}}$/atom.

range chopper spectrometer (ARCS) at the Spallation Neutron Source at Oak Ridge National Laboratory [27]. Single phonon scattering and vibrational densities of states (DOS) for the crystalline solids were obtained using the Mantid and multiphonon packages [31, 32]. More details on the incident energies, chopper settings, and maximum temperature for each sample are reported in Table 4.4 in the Supporting Information.

Thermodynamic integration with MTP

To reproduce dynamics across the melting transition, machine-learned moment tensor potentials (MTP) [33] for Ge, Si, Pb, and Li were trained on DFT data following [34]. For each element, the MTP potentials were actively trained on the fly by running MD simulations for a grid of volumes and temperatures near melting conditions. The interatomic potentials from this procedure were used to calculate the total change in entropy between the solid and liquid phases of each element with Bayesian learning thermodynamic integration [35]. The vibrational entropy contribution of each phase was estimated from the phonon density of states (PDOS) obtained from velocity autocorrelation function analyses [36]. For the liquid phase, the quasielastic peak was subtracted from the total PDOS. The Supporting Information provides additional details on MLIP construction and computational data analyses (see the Moment Tensor Potential training section 4.7).

4.3 Analysis

For a time-of-flight (TOF) Fermi chopper spectrometer, accessing a sufficient Q range to capture the structure and dynamics in liquids using neutron scattering presents a challenge due to the balance between energy resolution and the kinematic cutoff to the measurable range of reciprocal space. An incident energy of 50 meV provided a sufficiently fine resolution (approximately 2 meV at the elastic peak) and Q-cuts from 0.8-5 $Å^{-1}$. Each dataset was collected until excellent statistical quality was achieved (see Data Acquisition paragraph in the Supporting Information 4.7).

After subtracting the signal from the empty sample holder, the scattering intensities were separated into diffusive and vibrational components. First, the intensities were symmetrized using the condition of detailed balance and normalized with respect to the structure factor, yielding $\mathcal{S}(Q_n, \varepsilon)/\mathcal{S}(Q)$, where Q_n is a fixed Q

value and ε is the energy. The quasielastic peak was then fit to the well-established incoherent dynamic structure factor form,

$$\mathcal{S}(Q,\varepsilon) = \frac{1}{\pi}\frac{\hbar\Gamma(Q)}{\varepsilon^2 + (\hbar\Gamma(Q))^2} * R(Q,\varepsilon), \tag{4.3}$$

where Γ represents the peak width and $*R(Q,\varepsilon)$ denotes the convolution with the Q and ε dependent resolution function (determined from measurements on a vanadium standard at equivalent energy and chopper settings). This fit was then subtracted from the observed intensity because diffusion does not describe atomic vibrations and, therefore, will not contribute to the vibrational entropy [37].

Within the hydrodynamic regime (where $Q < Q_0/2$ and Q_0 is the location of the first peak in the structure factor, $\mathcal{S}(Q)$), these fits agree with previously reported self-diffusion coefficients, D, from the relationship $\Gamma = DQ^2$ [38–41]. Due to the increasing intensity of quasielastic scattering near the structure factor maximum (typically $\sim 2.5\text{Å}^{-1}$, as seen from the liquid spectra in Fig.4.2), a clear distinction between the diffusive and vibrational motion was not possible for all values of Q. Vibrational intensities were discernible below $Q = 1.65\text{Å}^{-1}$ (Ge), $Q = 1.55\text{Å}^{-1}$ (Bi, Sn, and Pb) and between $Q = 3.15-3.55\text{Å}^{-1}$ (Bi and Sn) and $Q = 2.85-3.25\text{Å}^{-1}$ (Pb). Spectra at these Q-cuts were selected for further analysis. Using this method to obtain these data allowed for minimal assumptions about the nature of atomic vibrations in the liquid phase.

To analyze the range of Q-cuts with distinct vibrational dynamics, a $\mathcal{S}(Q_n,\varepsilon)$ specific density of states (DOS) algorithm was developed (see corresponding section, 4.7, in the Supporting Information). Individual Q-cut DOSs for each element in the liquid were summed together and normalized to obtain the total vibrational density of states, $g(\varepsilon)$. This workflow was repeated on the solid for the same Q-cuts. The entropy difference between these was then calculated using $S_{l,\text{vib}} - S_{s,\text{vib}}$ where

$$S_{\text{vib}} = 3k_B \int g(\varepsilon)[(n(\varepsilon)+1)\ln(n(\varepsilon)+1) - n(\varepsilon)\ln(n(\varepsilon))]d\varepsilon, \tag{4.4}$$

is a relationship that has been tested with success for solids with large anharmonicity at high temperatures and was used (in the classical limit) to develop the vibrational-transit theory of liquids [16, 42–48].

A concern of this process is the limited Q-range where vibrational motion is distinguishable from diffusive motion. The main difficulty is that the transverse modes

are partially hidden by the resolution-broadened elastic peak or are not visible at low Q where $\vec{Q} \perp \vec{e}$ ($\vec{e}$ is the atom displacement in the vibrational mode) [49, 50]. This means that the DOSs generated from the sampled Q-cuts are not fully representative of the thermodynamic $g(\varepsilon)$. Two scalings procedures (see Supporing Information) were performed on these DOSs to demonstrate that the calculated vibrational entropy difference between the liquid and solid phase of each element is thermodynamically representative, even using subsets of Q. The deviations in ΔS_{vib} from these scalings were used as error bars in Fig. 4.4.

4.4 Results

The left columns of Figure 4.2 (a), (b) show background corrected inelastic neutron scattering spectra for polycrystalline and liquid Ge and Pb near their respective melting temperatures, $T_{\text{m,Ge}}$ = 1211 K and $T_{\text{m,Pb}}$ = 601 K. Intensities for each element are on the same scale so that a direct comparison of features between the solid and liquid phases is possible.

Selected constant-Q slices for liquid Ge and Pb are shown in the right column of Fig 4.2 (a), (b). Gray error bars show the excellent statistical quality of the collected data (the error bars are often smaller than the marker size). Dashed lines illustrate the resolution convoluted quasielastic fits of Eqn. 4.3. Each matches the expected Lorentzian shape and intensities well [39, 51–53].

In agreement with previous studies [54–56], non-diffusive contributions to the scattering intensities are observed in Q-cuts from both Ge and Pb (see Fig.4.2). Similar intensities are also found for Bi and Sn (see Fig.4.9 Supporting Information). After quasielastic, multiple scattering (MS), and multiphonon (MP) intensities are corrected for (see section 4.7 in the Supporting Information), only vibrational spectra remain. These are used to obtain the Q-weighted densities of states (DOSs) in Fig. 4.3 for Pb, Sn, Bi, and Ge. For comparison, crystalline solid DOSs obtained from the same Q values are plotted.

The upper vibrational modes in liquid Pb extend to energies higher than those of solid Pb, showing a "stiffening" from approximately 10 to 12 meV. This is unexpected since most materials exhibit the opposite behavior with increasing temperature. A more expected picture is observed in Sn, where there is a small "softening" of the vibrational spectrum upon melting. Despite this, the overall shapes of both solid and liquid DOS curves for Pb and Sn are similar. The elements Bi and Ge, which have appreciable deviations from Richard's rule, exhibit distinct

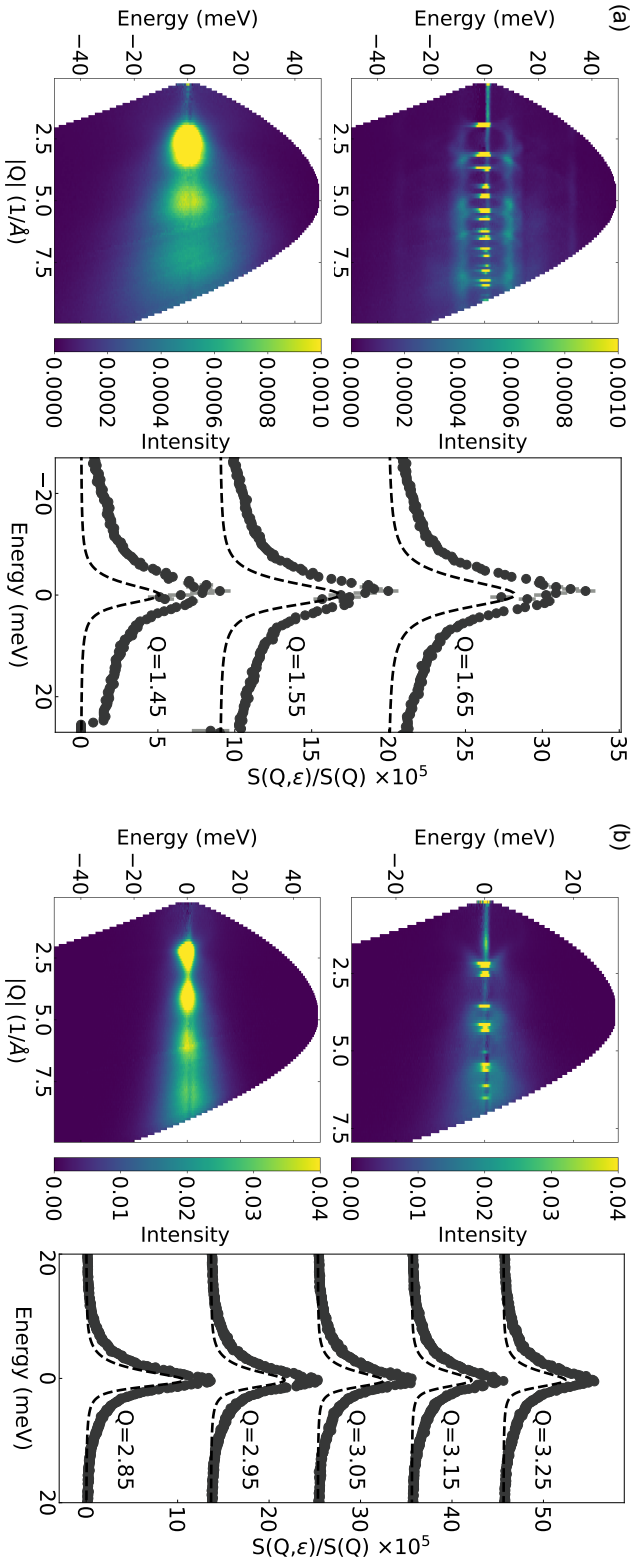

Figure 4.2: Total $\mathcal{S}(Q,\varepsilon)$ in the crystalline solid (top left) and liquid (bottom left) phases and selected $\mathcal{S}(Q_n,\varepsilon)$ (right) normalized to $\mathcal{S}(Q)$ for (a) Ge and (b) Pb near their respective melting temperatures. The dashed lines under the constant Q cuts are quasielastic fits to the data that include a convolution with the Q and ε-dependent instrument resolution function. The $\mathcal{S}(Q,\varepsilon)$ intensity for each element is identical and is shown on a log scale.

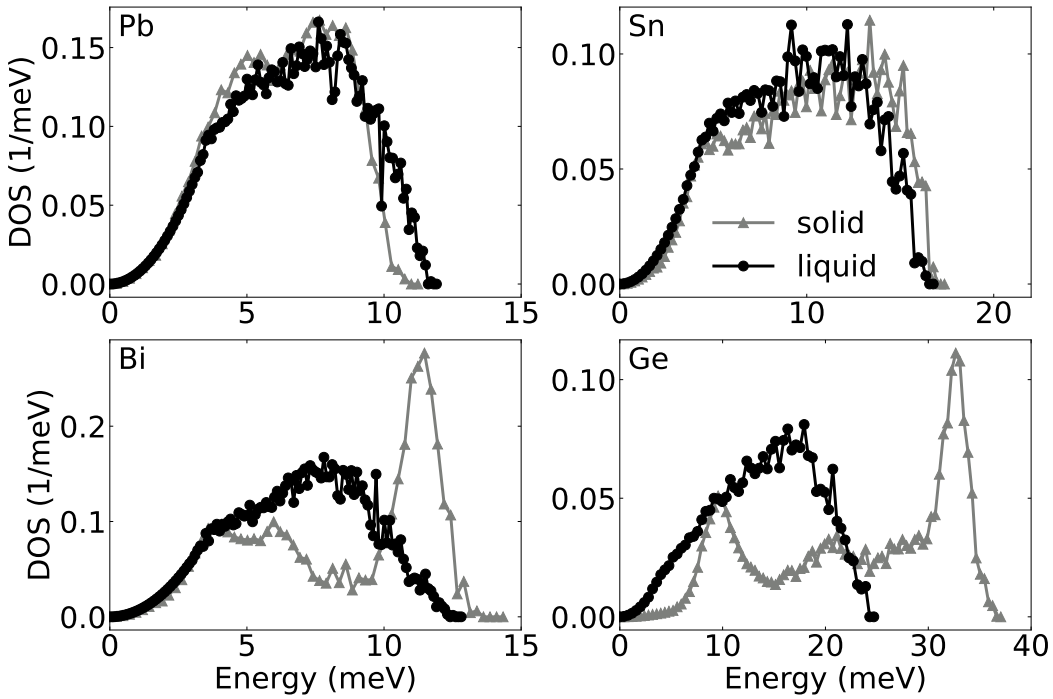

Figure 4.3: DOS curves from Q-cuts of Pb, Sn, Bi, and Ge in the crystalline solid (gray triangles) and liquid (black circles) from ARCS. Note the large softening in liquid Ge and the small stiffening in Pb. All DOSs are normalized to one.

differences in their vibrational DOSs between the crystalline and liquid phases. The highest vibrational peak in Bi softens from 11.4 to 8 meV. Ge shows an even greater decrease in energy between its solid and liquid states (32.8 to 17.2 meV). Computational DOSs (reported in Fig. 4.10 of the Supporting Information) confirm these behaviors.

Figure 4.4(a) shows the vibrational contributions to the entropy of fusion in Ge, Bi, Sn, and Pb from current inelastic neutron scattering measurements. The difference between the total and vibrational entropies of fusion, denoted ΔS_{extra}, for each element is also shown. Computational results for Ge, Si, Pb, and Li are illustrated alongside experimental results in Fig 4.4(b). The dashed horizontal line depicts the total entropy according to Richard's rule. Where available, there is excellent agreement between the vibrational components of these simulations and experiments (see Table 4.1).

4.5 Discussion

Changes in the DOSs of Fig. 4.3 give changes in the vibrational entropy across the melt (see Fig. 4.4(a)). In Ge, which has the most significant softening between

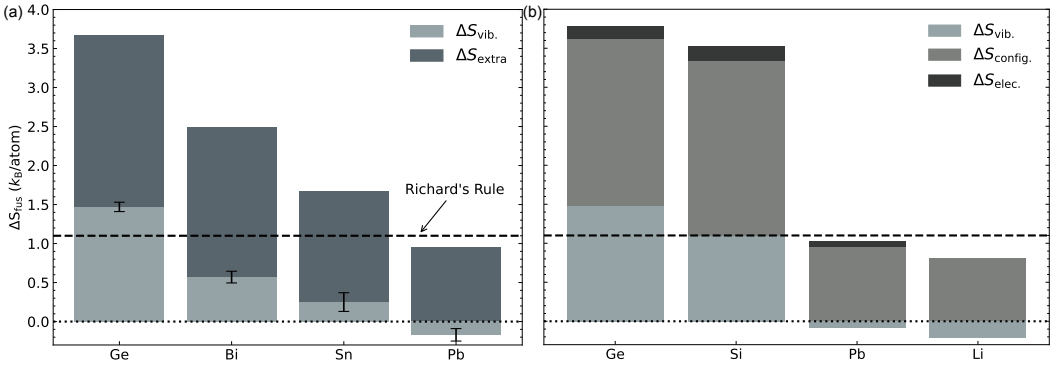

Figure 4.4: Vibrational (cool gray), and extra (gray) contributions to the entropies of fusion in Ge, Bi, Sn, and Pb determined from neutron-weighted densities of states at the best sampling of accessible reciprocal space (a). Error bars were estimated by scaling the neutron-weighted density of states (see details in Analysis). (b) Vibrational (cool gray), configurational (gray), and electronic (black) contributions to the entropies of fusion in Ge, Si, Pb, and Li from computations. The horizontal dashed line is the total entropy of fusion, $\Delta S_{fus} = 1.1 k_B$/atom, according to Richard's rule.

Table 4.1: Thermodynamic contributions to the entropy of fusion from experimental | computational methods.

Element **exp.|comp.**	ΔS_{fus} (k_B/atom)	$\Delta S_{fus,vib}$ (k_B/atom)	$\Delta S_{fus,config}$ (k_B/atom)	$\Delta S_{fus,el}$ (k_B/atom)
Ge	3.67|3.78	1.47|1.48	–|2.14	–|0.16
Si	3.58|3.51	–|1.09	–|2.24	–|0.19
Bi	2.50|–	0.57|–	–|–	–|–
Sn	1.67|–	0.25|–	–|–	–|–
Pb	0.95|1.03	-0.17|-0.08	–|1.03	–|0.07
Li	0.80|0.81	–|-0.21	–|1.02	–|0.00

Table 4.2: Physical properties of the elements investigated across the melt from measurements | simulations.

Element exp.|comp.	T_{melt} (K)	$V_{l\to s}$ (Å^3)	$\rho_{l\to s}$ (g/cm^3)	$\Delta z_{l\to s}$
Ge [57, 58]	1211|978	–|-1.74	–|0.29	3|–
Si [57, 59]	1683|1452	–|-2.17	–|0.20	2-3|–
Bi [60, 61]	545|–	–|–	–|0.32	3|–
Sn [62]	505|–	–|–	–|-0.21	2-3|–
Pb [63, 64]	601|663	–|1.46	–|-0.36	-1|–
Li [65]	454|476	–|0.30	–|–	5|–

solid and liquid, the vibrational entropy of melting accounts for 41% of the total entropy of fusion. Bi, as expected from the change in its DOS across the melt, shows a smaller but still significant vibrational contribution to ΔS_{fus}. In Sn, where the DOS shows minor changes, the contribution of vibrations to the entropy of fusion is small. Interestingly, Pb, which is generally considered to obey Richard's rule, exhibits a small but negative vibrational change in entropy upon melting. This result agrees with the DOS behavior (the slight stiffening of Fig. 4.3). Interestingly, within error bars, these results show that the vibrational contributions to the melting of each element scale with the total entropy of fusion, as plotted in Fig. 4.5.

The Ge simulations show a vibrational component nearly identical to that observed. These calculations also confirm the small negative value for ΔS_{vib} in Pb (see Table 4.1). Excellent agreement between experimental and computational results for Ge and Pb encouraged additional simulations of Si and Li, which were not measured experimentally. Having the vibrational contributions across the melt for these elements adds confidence to the emerging correlation between the total and vibrational entropies of fusion.

Simulations of the melt also gave insight into the non-vibrational entropic contributions, defined as the "extra" entropy in Fig. 4.4(a). From Eqn. 4.2,

$$\begin{aligned} \Delta S_{\text{fus,extra}} &= \Delta S_{\text{fus}} - \Delta S_{\text{fus,vib}} \\ &= \Delta S_{\text{fus,config}} + \Delta S_{\text{fus,el}} \ . \end{aligned} \tag{4.5}$$

As expected, transitioning from the ordered crystalline solid to a disordered liquid increases configurational entropy. (In contrast, the electronic entropy of fusion is nearly negligible for all elements calculated.) For Ge and Si, this configurational component is well above the value predicted by Richard's rule (see Table 4.1). Figure 4.1 shows additional deviations in Richard's rule and illustrates that the actual values of ΔS_{fus} span nearly an order of magnitude. Therefore, although Richard's rule helps estimate the entropy of melting, it is an approximation in search of physical underpinnings. A step beyond this rule has been taken by classifying melting as "normal" and "anomalous" based on whether materials do or do not follow Richard's rule. This adds more detail while keeping the convenience of a simple rule. Unfortunately, Fig. 4.1(b) shows this classification describes a wide range of materials, and that more insight into the atomistic components of melting is essential.

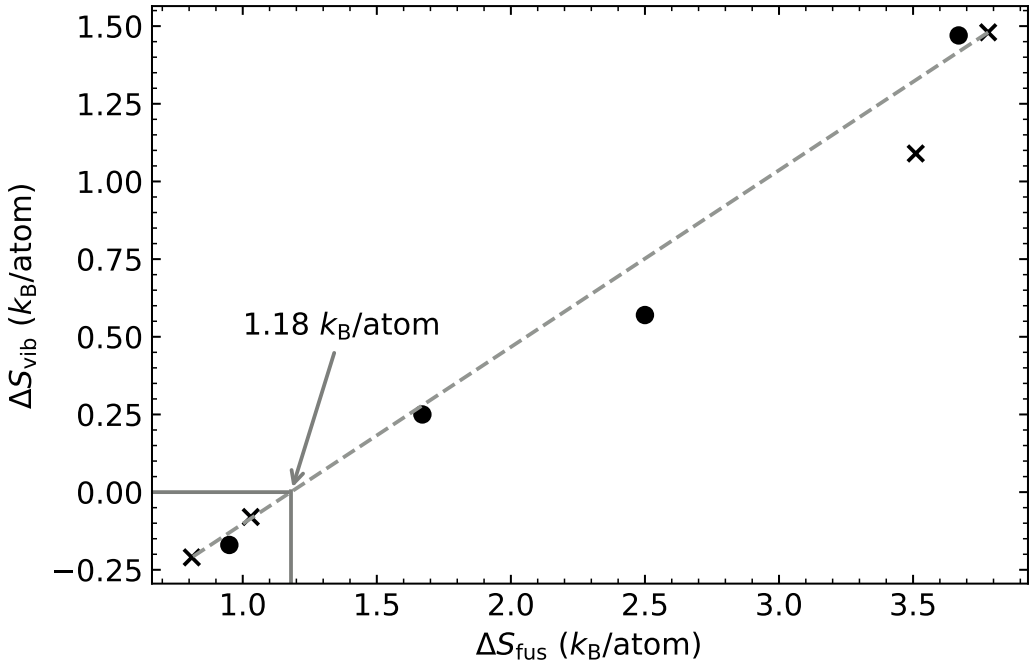

Figure 4.5: Vibrational entropies across the melt versus the total entropy of fusion. Circles (crosses) are from experimental (computational) results. The intercept at $\Delta S_{\text{fus,vib}} = 0$ occurs at $\Delta S_{\text{fus}} \approx 1.18\ k_{\text{B}}$/atom, near the value of Richard's rule.

Potential energy landscape (PEL) theory offers a convenient statistical thermodynamics framework to assess the relationship between the configurational, vibrational, and electronic components across the melt [66–68]. The PEL for a liquid has a large number of basins, $\Omega_{l,\text{b}}$. (Vibration-transit (V-T) theory associates these basins with intersecting valleys in the PEL [43, 44].) Atoms in the liquid make transitions between these basins, resulting in many possible equilibrium configurations. During the time spent in a basin, the N atoms undergo thermal vibrations (there is evidence that these vibrations are approximately harmonic, but this is not essential for the following discussion [44]). These vibrational dynamics explore a volume in the phase space of momentum, $\vec{p}$ and position $\vec{q}$, where the vector notation indicates that there are $3N$ independent coordinates of each. The number of vibrational states, $\Omega_{l,\vec{p}}\,\Omega_{l,\vec{q}}$, available to the material is proportional to this $6N$-dimensional volume. Metallic liquids also have a number $\Omega_{l,\text{el}}$ of states accessible to thermally-excited electrons. Using these components, the total number of states available to the liquid, Ω_{l}, is

$$\Omega_l = \Omega_{l,\text{b}}\Omega_{l,\vec{p}}\,\Omega_{l,\vec{q}}\,\Omega_{l,\text{el}}\ . \tag{4.6}$$

Thermally accessible states for the crystal are enumerated similarly, with the big difference of $\Omega_{s,\mathrm{b}} = 1$ because there is only one equilibrium structure for atoms in the crystal. The total number of states accessible to the crystalline solid at T_m is then

$$\Omega_s = \Omega_{s,\vec{p}}\,\Omega_{s,\vec{q}}\,\Omega_{s,\mathrm{el}}\ . \tag{4.7}$$

The kinetic energy of the atoms in both phases is the thermal energy, $3N\,k_\mathrm{B}T/2$.

Using this formalism and the Boltzmann entropy, $S = k_\mathrm{B}\ln\Omega$, the relationship between these microstates and the entropy of fusion can be developed by recognizing $\Delta S_\mathrm{fus} = S_l(T_\mathrm{m}) - S_s(T_\mathrm{m}) = k_\mathrm{B}\ln(\Omega_l/\Omega_s)$. Begin by taking the ratio

$$\frac{\Omega_l}{\Omega_s} = \frac{\Omega_{l,\mathrm{b}}\,\Omega_{l,\vec{q}}\,\Omega_{l,\mathrm{el}}}{\Omega_{s,\vec{q}}\,\Omega_{s,\mathrm{el}}}\ , \tag{4.8}$$

where because the atom masses are the same in both the solid and liquid, the ranges explored in momentum space are equal, and the degrees of freedom associated with momentum cancel. Next, the relationship between atomic vibrations and position space is addressed.

Whether considered from a local or non-local perspective, the complete set of vibrational modes must account for the simultaneous vibrations of all N atoms. A linear transformation from atom coordinates, $\vec{q}$, to vibrational modes preserves the number of $3N$ independent modes. In this representation, a mode j with lower frequency ω_j has a large amplitude of vibration for a fixed energy. At high temperatures, when atoms execute thermal vibrations as harmonic oscillators, the range explored in $\vec{q}$-space is proportional to $\prod_j^{3N}(1/\omega_j)$ [16], yielding

$$\frac{\Omega_l}{\Omega_s} = \frac{\Omega_{l,\mathrm{b}}\left\{\prod_j^{3N}(1/\omega_{l,j})\right\}\Omega_{l,\mathrm{el}}}{\left\{\prod_j^{3N}(1/\omega_{s,j})\right\}\Omega_{s,\mathrm{el}}}\ . \tag{4.9}$$

Then,

$$\begin{aligned}\Delta S_\mathrm{fus} &= S_{l,\mathrm{b}} + S_{l,\mathrm{vib}} + S_{l,\mathrm{el}} - S_{s,\mathrm{vib}} - S_{s,\mathrm{el}} \\ &= k_\mathrm{B}\left[\ln(\Omega_{l,\mathrm{b}}) + \ln\left(\frac{\prod_j^{3N}(1/\omega_{l,j})}{\prod_j^{3N}(1/\omega_{s,j})}\right) + \ln\left(\frac{\Omega_{l,\mathrm{el}}}{\Omega_{s,\mathrm{el}}}\right)\right] \\ &= \Delta S_\mathrm{fus,config} + \Delta S_\mathrm{fus,vib} + \Delta S_\mathrm{fus,el}\ ,\end{aligned} \tag{4.10}$$

where the entropy from the number of basins in the liquid is relabeled as a configurational entropy, $S_{l,\mathrm{config}}/k_\mathrm{B} = \ln\Omega_{l,\mathrm{b}}$ (again, this is negligible for a crystal of

a pure element). This is possible since diffusional processes in a liquid move the atoms between basins in the PEL, allowing the equilibrium value of $S_{l,\mathrm{config}}$ from $\Omega_{l,\mathrm{b}}$ to be reached. There is a long history of work to extract an $S_{l,\mathrm{config}}$ from the pair distribution function (PDF) of a liquid [43], but the PDF is a one-dimensional quantity that cannot fully account for three-dimensional structures.

For the vibrational entropy component, Eqn. 4.4 is used as the product function ($\prod_j^{3N}$). The current analysis of inelastic neutron scattering data was designed to evaluate the change in vibrational entropy across melting from the DOS above approximately $\hbar\omega = 3\,\mathrm{meV}$. This accounts for most of the vibrational modes in the material, but there could be errors from vibrational modes at lower energy (and an issue with transverse modes mentioned in the Analysis section). Our computational work obtained $S_{l,\mathrm{config}}$ such that

$$S_{l,\mathrm{config}} = \Delta S_{\mathrm{fus}} - \Delta S_{\mathrm{fus,vib}} - \Delta S_{\mathrm{fus,el}}. \tag{4.11}$$

The $\Delta S_{\mathrm{fus,config}}$ for melting is always positive, as expected because $\Omega_{l,\mathrm{b}}$ is much larger than 1. There is some variation in the magnitude of $\Delta S_{\mathrm{fus,config}}$ – approximately a factor of two for the elements studied here. Nevertheless, the change in vibrational entropy can be comparably large, or even negative. (The negative values of ΔS_{vib} are bounded because ΔS_{fus} must be positive.) Following prior observations that elements with large ΔS_{fus} (e.g., Si and Ge) undergo large changes in local structure upon melting [17], we might expect a correlation between ΔS_{fus} and the change in coordination number Δz of Table 4.2. This correlation is not so compelling, however, since the chemical potential also depends on bond distances and angles.

Figure 4.5 shows a trend for all our results. We note that the ΔS_{vib} is zero for $\Delta S_{\mathrm{fus}} \approx 1.2\,k_{\mathrm{B}}$/atom, which is close to the value used for Richard's rule. The linear relationship shows that the extra (denoted δ) configurational entropy is proportional to the extra vibrational entropy as

$$\delta S_{\mathrm{config}} = 0.77\,\delta S_{\mathrm{vib}}\ , \text{ so} \tag{4.12}$$

$$\Delta S_{\mathrm{fus}} - 1.2 = 1.77\,\Delta S_{\mathrm{vib}}\ , \tag{4.13}$$

in units of k_{B}/atom. Since larger vibrational entropy corresponds to potential wells having lower curvatures, Eqn. 4.12 makes an unexpected statement about the PEL. Upon melting, the number of basins (or configurations) accessible to the liquid is inversely proportional to the change in curvature of the basins (with respect to the solid).

4.6 Summary and Conclusions

Methods of inelastic neutron scattering (INS) were developed for measuring vibrational spectra of materials across melting transitions. Quasielastic scattering from diffusional processes confined the data analysis to lower values of momentum transfer or those slightly above the maximum intensity of the structure factor. Accounting for quasielastic scattering, multiple scattering, and multiphonon scattering allowed isolation of the vibrational spectra above 3 meV. Approximate phonon DOS curves were obtained for the liquid and the solid phases of Ge, Bi, Sn, and Pb using the same analyses, giving the change in vibrational entropy across melting.

The computational methods implemented to model the melt required large numbers of atoms, and employed classical molecular dynamics with machine-learned interatomic potentials obtained from ab initio molecular dynamics calculations on smaller systems. Computational results gave changes in vibrational entropies upon melting that were in excellent agreement with the INS results for Ge and Pb. These simulations also accounted well for the total latent heat.

We first note that a reasonable value of Richard's rule can be selected as the case where there is zero change in vibrational entropy upon melting. From Fig. 4.5 this sets Richard's rule at approximately 1.2 k_B/atom for the entropy of fusion. Positive deviations from Richard's rule imply both a positive value of ΔS_{vib}, and an extra ΔS_{config} of 77% of this ΔS_{vib}, but with the same sign. A positive departure from Richard's rule suggests that the PEL surface has more basins, but these basins have curvatures that are smaller than for the crystal.

4.7 Supporting Information

Inelastic Neutron Scattering Methods and Analysis

Data Acquisition

At the Spallation Neutron Source, the number of neutrons emitted is directly proportional to the number of protons incident on the target. Therefore we account for variations in power by counting to a certain number of protons incident on the target or a specific proton charge in Coulombs. To obtain the excellent statistical quality reported in the main text, data was collected until 2C of proton charge was accumulated.

Multiple Scattering Corrections

The MCViNE (Monte-Carlo VIrtual Neutron Experiment) software is a neutron ray-tracing simulation package that tracks the pathway of neutrons through the interaction with instrument components, scattering from the sample, interception by the detectors, and reduction to an experimentally equivalent format [69]. Here, MCViNE was used to simulate the effects of multiple scattering from polycrystalline germanium, tin, and lead measured on the wide Angular-Range Chopper Spectrometer (ARCS) instrument near each melting temperature.

All samples were modeled with dimensions and orientations matching the respective experimental setup. The simulated inelastic spectra were obtained from 7×10^9 neutron packets emitted from the moderator and passed through the simulated instrument with chopper settings identical to those from the ARCS measurements. The incoherent approximation using the full neutron cross-section was assumed for all elements, allowing for a polycrystalline average without explicit knowledge of the phonon dispersions. The resulting event-mode NeXus files were reduced using the same data reduction tools as the experimental data [31].

These simulations allow contributions from multiple scattering (MS) to be turned on or off, making intensities from MS in the dynamic scattering function, $\mathcal{S}(Q, \varepsilon)$, easy to identify. For each Q-cut of interest, results show that while MS is non-negligible, it is predominately elastic scattering, and the shape of the one-phonon scattering is preserved. This implies that a constant background subtraction scaled to match MS is sufficient to correct for these effects. Excellent agreement between the solid densities of states (DOS) from Q-cuts and previous experimental DOS [70–72] supports this choice of MS subtraction in the solid. Similarly, the strong agreement between the experimental and computational results in the liquid phase implies that this correction method also holds for liquid scattering.

Quasielastic Fitting

An incident energy of 50 meV provides scattering from $Q = 0.5 - 10\text{Å}^{-1}$ with a resolution of 0.1Å^{-1}[1]. After data reduction and subtraction of the signal from the sample holder, regions of reciprocal space with distinct intensity away from $\varepsilon = 0$ meV were identified. These were below $Q = 1.65\text{Å}^{-1}$ (Ge) or $Q = 1.55\text{Å}^{-1}$ (Bi, Sn, and Pb) and between $Q = 3.15 - 3.55\text{Å}^{-1}$ (Bi and Sn) or $Q = 2.85 - 3.25\text{Å}^{-1}$

[1] This resolution was determined by observing at which bin size there were not any intensities for a given value of Q.

(Pb). For these values of Q, quasielastic scattering takes the shape of a Lorentzian, and the spectra can be fit to the incoherent response function,

$$\mathcal{S}(Q,\varepsilon) = \frac{A}{\pi}\frac{\hbar\Gamma(Q)}{\varepsilon^2 + (\hbar\Gamma(Q))^2} * R(Q,\varepsilon)\ , \tag{4.14}$$

where A is a scaling factor, $\Gamma = DQ^2$ describes the peak width, and $*R(Q,\varepsilon)$ denotes convolution with the resolution function. All spectra fit to this expression were normalized with respect to the structure factor, $\mathcal{S}(Q)$ and symmetrized using detailed balance,

$$\mathcal{S}(Q,-\varepsilon) = \exp\left(-\varepsilon/k_{\mathrm{B}}T\right)\mathcal{S}(Q,\varepsilon). \tag{4.15}$$

The objective of fitting quasielastic neutron scattering (QENS) peaks was to subtract them from each Q_{n} spectrum and extract the vibrational intensities. Since vibrational dynamics have some contributions to the intensity under the quasielastic peak, using the hydrodynamic limit (where $Q < Q_0/2$ and Q_0 corresponds to the location of the first intensity peak in $\mathcal{S}(Q)$) and known diffusion coefficients to build the initial fitting model was essential. First, a $Q \approx 0.5\text{Å}^{-1}$ spectral cut for each element was normalized to $S(Q)$ and symmetrized with detailed balance. Then, using $Q = 0.5\text{Å}^{-1}$ and previously reported liquid diffusion coefficients, D, near the melting temperature [38–41], Γ was calculated. From Γ, Eqn. 4.14 was evaluated for varying intensity offsets of the $Q = 0.5\text{Å}^{-1}$ cut, and the value that gave the smallest root mean squared error fit to the data was chosen as the starting offset for higher Q spectra. Aside from this empirical starting model, all spectra were fit to Eqn. 4.14 with Γ and A as free parameters. The Q^2 behavior of vibrational intensity was also taken into account. Where possible, the diffusion coefficient from higher Q-cuts (but still below $Q_0/2$) was found to reproduce the diffusion coefficient well (see Table 4.5). Fitting with this procedure (i.e., only looking at the central peak) avoided any assumptions regarding the behavior of vibrational dynamics away from $\varepsilon \approx 0$. The resulting quasielastic fits from each Q of interest are subtracted from the inelastic neutron spectra and further analyzed using the density of states algorithm described below.

Density of States Analysis

To analyze the range of Q-cuts with distinct vibrational spectra, a $\mathcal{S}(Q_{\mathrm{n}},\varepsilon)$ specific density of states (DOS) algorithm was developed. For each Q, a multiple scattering correction, informed by Monte Carlo ray tracing (see above), was performed. Then, an initial guess of the vibrational density of states with a chosen

energy maximum was input to calculate multiphonon contributions. The $\mathcal{S}(Q_n, \varepsilon)$ generated from this process was used to scale the measured vibrational intensities to this calculated spectra to obtain the one-phonon scattering function. The experimental density of states was then calculated from

$$g(\varepsilon) = A_1(\varepsilon) \times \varepsilon \times \gamma_0 \times [1 - \exp(-\varepsilon/(k_B T))], \tag{4.16}$$

where A_1 is the one-phonon scattering and

$$\gamma_0 = \int \coth\left(\frac{\varepsilon}{2k_B T}\right) \frac{g(\varepsilon)}{\varepsilon} d\varepsilon \tag{4.17}$$

is calculated from the previous DOS iteration. This process is continued until the difference between the calculated and observed DOS is minimal, as outlined by Sears et al. and others [25, 73]. Varying the initial DOS energy maximum by ± 1 meV showed little change in the final DOS. Once converged, the Q-cut DOSs are summed together and renormalized. This workflow is repeated on the solid for the same Q-cuts.

As outlined in the main text, a concern of this process is the limited Q-range where vibrational and diffusive motion are separable. This limitation means the DOSs generated from the sampled Q-cuts do not fully represent the thermodynamic $g(\varepsilon)$. Two scalings were performed to demonstrate that although the Q-cut derived DOSs are not fully descriptive of phonon thermodynamics, the entropy difference between the liquid and solid Q-cut DOSs is.

Both scaling methods begin with the thermodynamic polycrystalline DOS calculated using the well-established multiphonon package [74]. The solid Q-cut weighed DOS is then calculated using the same $\{Q_n\}$ that are of interest in the liquid. As in the liquid, the transverse modes of the solid Q-weighed $g(\varepsilon)$ are not visible at low Q where $\vec{Q} \perp \vec{e}$ ($\vec{e}$ is the atom displacement in the vibrational mode) [49, 50]. However, the true $g(\varepsilon)$ is known in the solid, and a multiplicative factor to bring the Q-weighed DOS into agreement with the thermodynamic DOS is calculated for each element.

The first scaling applies this multiplicative factor to the solid and liquid Q-weighed DOS up to the energy of the first transverse peak. After renormalization, the lower region of the liquid DOS is in better agreement with the computational (thermodynamic) vibrational $g(\varepsilon)$, as seen from Fig. 4.7. For the second scaling, the multiplicative factor is applied to the entire energy range of the solid and liquid $\{Q_n\}$ DOS. The resulting (renormalized) liquid DOSs for each element are

shown in Fig. 4.8. After each scaling, the sound velocity of the solid and liquid was used to confirm that the behavior of the low-energy regime (less than 2 meV) was correct [75]. In bismuth, the low energy scaled $g(\varepsilon)$ required an additional correction (the step in the liquid DOS of Fig. 4.7).

Entropy differences between the solid and liquid vibrational densities of states were calculated using the DOSs from each of these scaling methods and compared to the $\Delta S_{\text{fus,vib}}$ from the non-scaled DOSs. Minor variations observed between these values were used to generate error bars for the reported vibrational entropy of fusion. The general agreement of the final change in entropy supports that these values are thermodynamically representative even using subsets of Q.

Computational Methods and Analysis

Density functional theory calculations

All density functional theory (DFT) calculations were performed with the Vienna *Ab Initio* Simulation Package (VASP) [76–78]. Plane-wave basis sets with a kinetic energy cutoff of 500 eV and projector-augmented-wave pseudopotentials [79, 80] were used with Perdew-Burke-Ernzerhof (PBE) exchange-correlation functionals [81]. Each calculation used a 4×4×4 supercell (128 atoms) for bcc Li, 3×3×3 supercell (108 atoms) for fcc Pb, and 2×2×2 supercell (64 atoms) for diamond Ge and Si. Monkhorst-Pack [82] k-point meshes of $5 \times 5 \times 5$ for Li, $3 \times 3 \times 3$ for Pb, and $4 \times 4 \times 4$ for Ge and Si were used for vibrational and electronic supercell calculations.

Moment Tensor Potential training

Large-scale molecular dynamics (MD) simulations were performed with the use of Moment Tensor Potentials (MTPs) [33, 83] as implemented in the MLIP software package [34]. A total of four MTPs were fit to quantum mechanical data.

Moment tensor potentials for each element were trained to reproduce both the solid and liquid phases and their lattice dynamics near and across the melt. Training for each followed the procedure described in [34] for the calculation of the melting point of Al. In the pretraining stage, a level-16 MTP with a cutoff radius of 5 Å and the mindist parameter set to 1.4 Å was trained with 20 configurations sampled from *ab initio* molecular dynamics. Next, on-the-fly training was performed using classical molecular dynamics for the solid and liquid phases near the melting point. Configurations selected from this training were processed with low-fidelity DFT to

Table 4.3: Details of the MTPs fitting procedure.

Element	N_{conf}	ΔE (meV/atom)	F_{rel} (%)	S_{rel} (%)
Li	115	0.6	5	2
Pb	128	0.8	8	3
Ge	104	3.3	15	14
Si	124	5.4	14	16

reduce computational cost. The final training set, generated from a subset of these configurations, was run with high-accuracy DFT calculations using the parameters given in the previous section. Another round of active learning was also performed in this step.

A summary of the fitting procedure is shown in Table 4.3. N_{conf} is the number of configurations in the training set, ΔE is the mean potential energy difference per atom between the MTP and the *ab initio* model. F_{rel} and S_{rel} are the relative energy and stress difference per atom and are computed using

$$A_{\text{rel}} = \sqrt{\frac{\langle (\Delta A - \overline{\Delta A})^2 \rangle}{\langle (A_{\text{MTP}} - \overline{A}_{\text{MTP}})^2 \rangle}}\,, \tag{4.18}$$

where ΔA is the difference in force or stress between the *ab initio* model and the moment tensor potential, and $\overline{\Delta A}$ its mean value.

Autocorrelation function analyses

As is shown in [36, 84] an accurate method for calculating the vibrational density of states, $g(\varepsilon)$, is taking the Fourier transform of the velocity autocorrelation function $\Phi(t)$.

$$\Phi(t) = \frac{1}{N}\sum_{i}^{N} \frac{\left\langle \mathbf{v}_i(t)\mathbf{v}_i(0) \right\rangle}{\left\langle \mathbf{v}_i(0)\mathbf{v}_i(0) \right\rangle}, \quad g(\varepsilon) = \int_0^\infty \Phi(t)\cos(\varepsilon t/\hbar)dt. \tag{4.19}$$

In theory, autocorrelation methods include anharmonic effects up to infinite order. However, convergence of the autocorrelation function is only reached at long time scales, and a large supercell is required to resolve a sufficient amount of points in the Brillouin zone. Thus, due to computational cost, *ab initio* molecular dynamics can only be used for very approximate calculations [85]. On the other hand, classical force fields scale well with time and supercell size but provide only a general

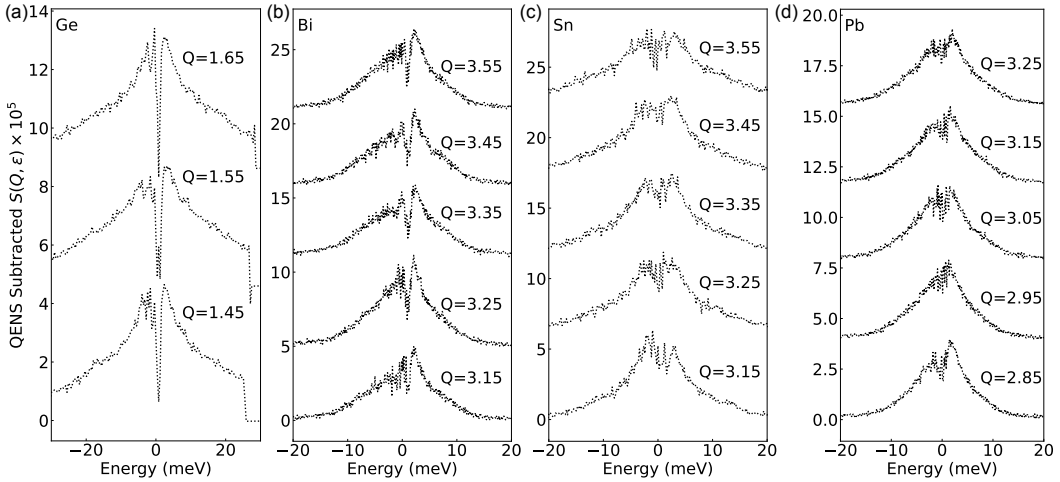

Figure 4.6: Quasielastic subtracted spectra for (a) Ge, (b) Bi, (c) Sn, and (d) Pb.

description of systems' behavior [86]. Thus, we use machine learning interatomic potentials trained on *ab initio* data to perform large-scale simulations, preserving the quantum-mechanical level of accuracy with reasonable computational time.

The Moment Tensor Potentials obtained with the MLIP procedure were used to perform large-scale molecular dynamics simulations with the LAMMPS code [87]. The supercell size was 20×20×20 of the conventional unit cell of the corresponding solid phase. The calculations were performed in two subsequent steps. In the first step, the system was equilibrated near melting. For the solid phase, this corresponded to a molecular dynamics run at zero pressure and melting temperature for 40 ps. The procedure for liquids included an additional melting stage in which the system was kept at a high temperature (four times the melting temperature) for 40 ps. In the second step, the equilibrated phases were run in the microcanonical (NVE) ensemble for 10 ps. The autocorrelation function was then computed using outputs from this step.

The Fourier transform of the autocorrelation function was used to obtain the anharmonic vibrational density of states. For the liquid phase, the contributions from diffusive processes were removed by subtracting a Lorentzian fit (similar to Eqn. 4.14) from the density of states (the resolution function was taken as one in the case of computational data). The obtained computational density of states for different elements is shown in Fig. 4.10. Finally, the vibrational contribution to the entropy from both phases was calculated using Eqn. 4.4.

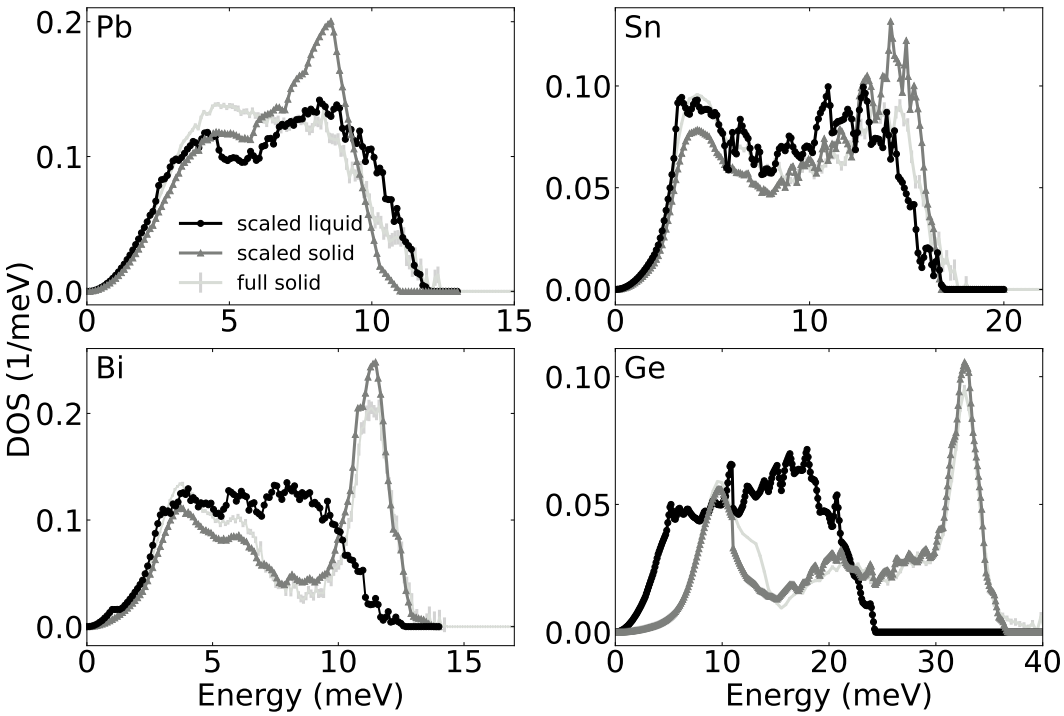

Figure 4.7: Low-energy scaled vibrational DOS curves from low Q-cuts. The location of the first transverse mode in the solid density of states determined the low energy scaling cutoff. All DOSs are normalized to one.

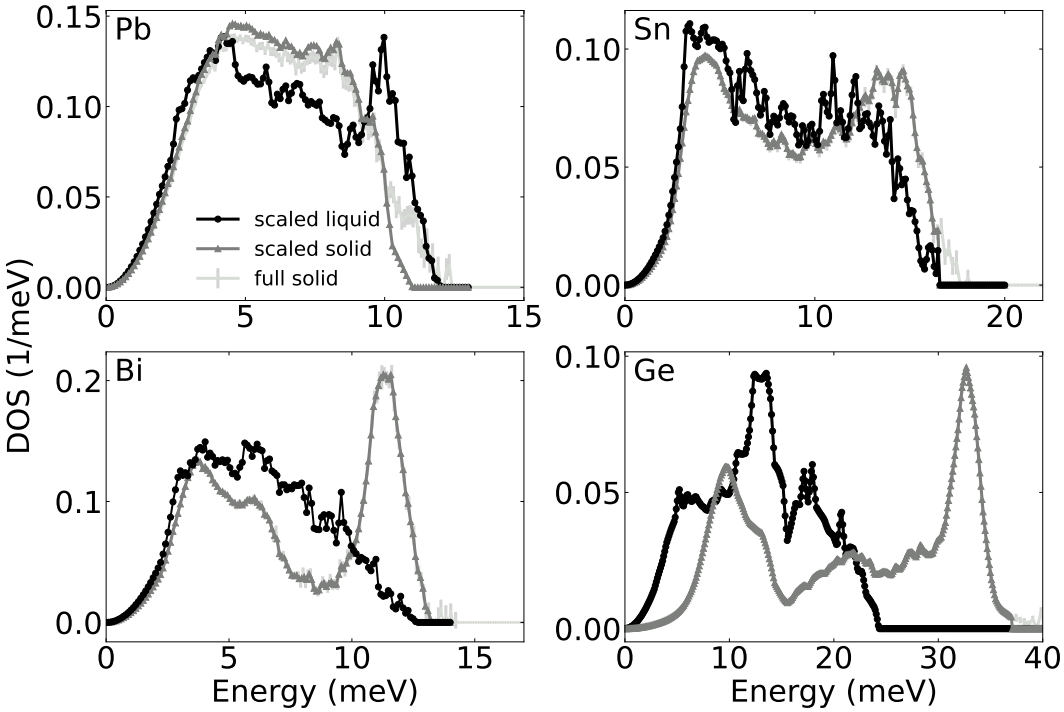

Figure 4.8: Full-energy scaled vibrational DOS curves from low Q-cuts. All DOSs are normalized to one.

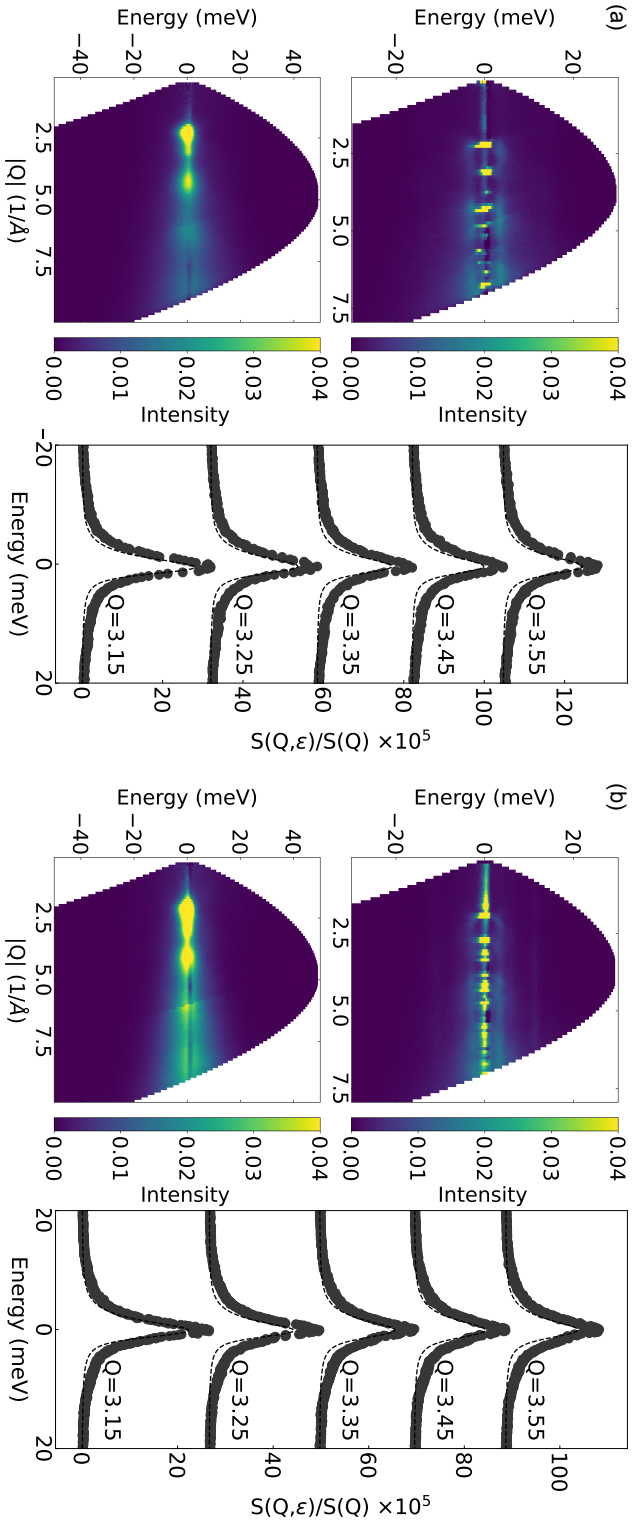

Figure 4.9: Total $\mathcal{S}(Q,\varepsilon)$ in the crystalline solid (top left) and liquid (bottom left) phases and selected $\mathcal{S}(Q_n,\varepsilon)$ (right) normalized to $\mathcal{S}(Q)$ for (a) Sn and (b) Bi near their respective melting temperatures. The dashed lines under the constant Q cuts are quasielastic fits to the data that include a convolution with the Q and ε-dependent instrument resolution function. The $\mathcal{S}(Q,\varepsilon)$ intensity for each element is identical and is shown on a log scale.

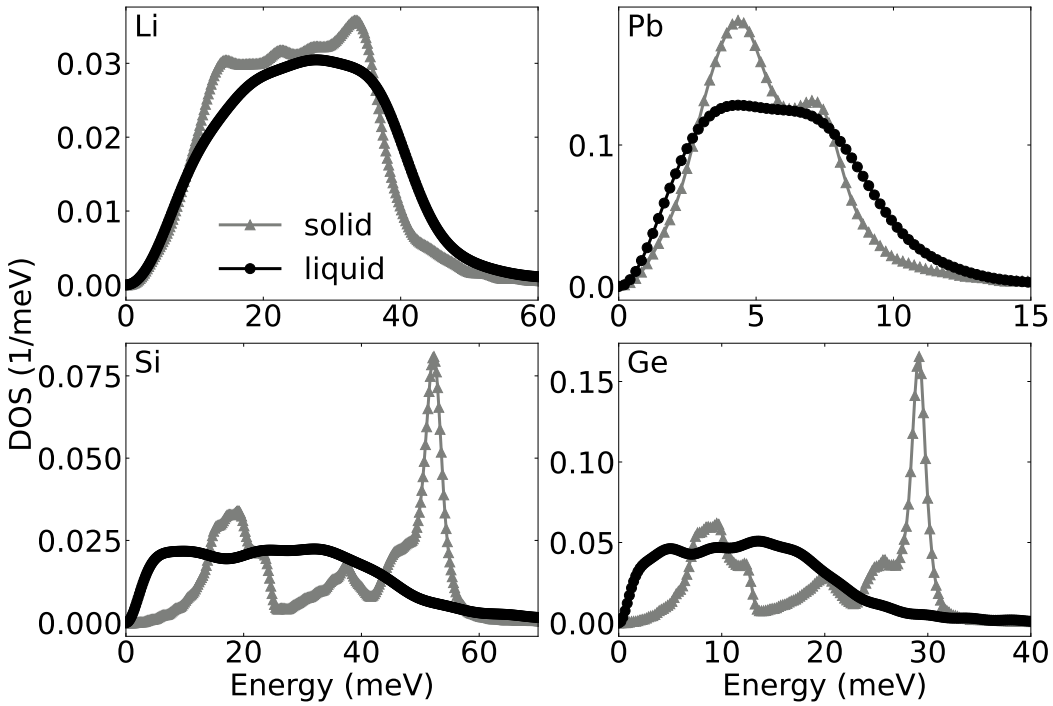

Figure 4.10: Vibrational DOS curves from velocity autocorrelations of Li, Pb, Si, and Ge in the crystalline solid (gray triangles) and liquid (black circles) from computations. Note the large softening in liquid Ge and the small stiffening in Li and Pb. All DOSs are normalized to one.

Table 4.4: Time-of-flight inelastic neutron scattering details, including maximum temperature measured, incident energies, and chopper settings.

	Temp.(K)	E_{inc}(meV)	T0(Hz)	Fermi Chopper(Hz)
Ge	1373	30, 50	90	300, 420
Sn	673	30, 50	90	300, 420
Bi	673	30, 50	90	300, 420
Pb	773	30, 50	90	300, 420

Table 4.5: Diffusion coefficients of Ge, Bi, Sn, and Pb from fits to the incoherent dynamic structure factor below the structure factor maximum.

Element	D ($Å^2/s$)	Q ($Å^{-1}$)
Ge	1.25×10^{12}	1.05
Sn	2.66×10^{11}	0.95
Bi	2.48×10^{11}	0.85
Pb	1.74×10^{11}	0.95

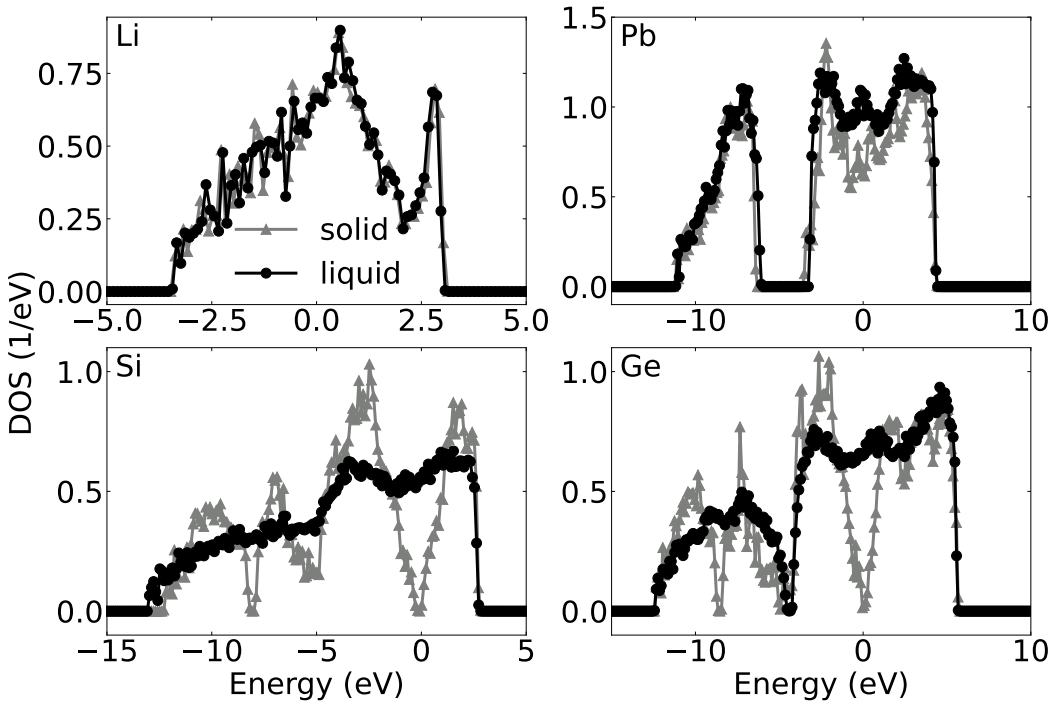

Figure 4.11: Electronic DOS curves from of Li, Pb, Si, and Ge in the crystalline solid (gray triangles) and liquid (black circles) from computations. At the Fermi energy ($E = 0$), Li and Pb show little change across the melt, while Si and Ge do. These results are consistent with the semiconductor-to-metal transition of Si and Ge.

References

[1] H. B. Callen, *Thermodynamics and an introduction to thermostatistics*, 2nd ed. (Wiley New York, New York, 1985).

[2] J. R. Morris, C. Z. Wang, K. M. Ho, and C. T. Chan, Phys. Rev. B **49**, 3109 (1994).

[3] M. Karthikeyan, R. C. Glen, and A. Bender, J. Chem. Inf. Model. **45**, 581 (2005).

[4] Q.-J. Hong and A. van de Walle, J. Chem. Phys. **139**, 094114 (2013).

[5] Q.-J. Hong, S. V. Ushakov, A. van de Walle, and A. Navrotsky, Proc. Natl. Acad. Sci. **119**, e2209630119 (2022).

[6] F. Lindemann, Phys. Z. **11**, 609 (1910).

[7] M. M. Vopson, N. Rogers, and I. Hepburn, Solid State Commun. **318**, 113977 (2020).

[8] C. Chakravarty, P. G. Debenedetti, and F. H. Stillinger, J. Chem. Phys **126**, 204508 (2007).

[9] S.-A. Cho, J. Phys. F: Met. Phys. **12**, 1069 (1982).

[10] D. C. Wallace, Proc. Royal Soc. London. Ser. A: Math. Phys. Sci. **433**, 631 (1997).

[11] J. Ding, L. Li, N. Wang, L. Tian, M. Asta, R. Ritchie, and T. Egami, Mater. Today Phys. **17**, 100359 (2021).

[12] Q. An, W. L. Johnson, K. Samwer, S. L. Corona, and W. A. Goddard, Scr. Mater. **194**, 113695 (2021).

[13] P.-W. Guan and V. Viswanathan, *Meltnet: predicting alloy melting temperature by machine learning*, 2020.

[14] K. K. Bejagam, J. Lalonde, C. N. Iverson, B. L. Marrone, and G. Pilania, J. Phys. Chem. B **126**, 934 (2022).

[15] J. H. Jung, P. Srinivasan, A. Forslund, and B. Grabowski, NPJ Comput. Mater. **9**, 3 (2023).

[16] B. Fultz, *Phase Transitions in Materials*, 2nd ed. (Cambridge University Press, Cambridge, 2020).

[17] G. Grimvall, Liquid Metals 1976, 90 (1977).

[18] D. C. Wallace, Int. J. Quantum Chem. **52**, 425 (1994).

[19] R. K. Schulze, D. C. Wallace, and J. C. Lashley, J. Phys.: Condens. Matter **25**, 465107 (2013).

[20] C. K. Das, in Evolutionary Computing and Mobile Sustainable Networks, edited by V. Suma, X. Fernando, K.-L. Du, and H. Wang, Lecture Notes on Data Engineering and Communications Technologies (2022), pp. 575–592.

[21] V. Sears, Adv. Phys. **24**, 1 (1975).

[22] B. N. Brockhouse, Phys. Rev. Lett. **2**, 256 (1959).

[23] S. K. Sinha, J. Phys.: Condens. Matter **13**, 7511 (2001).

[24] P. D. Bogdanoff, B. Fultz, J. L. Robertson, and L. Crow, Phys. Rev. B **65** (2001).

[25] M. Kresch, O. Delaire, R. Stevens, J. Y. Y. Lin, and B. Fultz, Phys. Rev. B **75**, 104301 (2007).

[26] H. L. Smith, C. W. Li, A. Hoff, G. R. Garrett, D. S. Kim, F. C. Yang, M. S. Lucas, T. Swan-Wood, J. Y. Y. Lin, M. B. Stone, D. L. Abernathy, M. D. Demetriou, and B. Fultz, Nat. Phys. **13**, 900 (2017).

[27] D. L. Abernathy, M. B. Stone, M. J. Loguillo, M. S. Lucas, O. Delaire, X. Tang, J. Y. Y. Lin, and B. Fultz, Rev. Sci. Instrum. **83**, 015114 (2012).

[28] V. Jaiswal, L. Leal, and A. I. Kolesnikov, EPJ Web Conf. **239**, edited by Z. Ge, N. Shu, Y. Chen, W. Wang, and H. Zhang, 14007 (2020).

[29] T. Egami and Y. Shinohara, J. Chem. Phys. **153**, 180902 (2020).

[30] J. L. Niedziela, R. Mills, M. J. Loguillo, H. D. Skorpenske, D. Armitage, H. L. Smith, J. Y. Y. Lin, M. S. Lucas, M. B. Stone, and D. L. Abernathy, Rev. Sci. Instrum. **88**, 105116 (2017).

[31] O. Arnold, J. C. Bilheux, J. M. Borreguero, A. Buts, S. I. Campbell, L. Chapon, M. Doucet, N. Draper, R. Ferraz Leal, M. A. Gigg, V. E. Lynch, A. Markvardsen, D. J. Mikkelson, R. L. Mikkelson, R. Miller, K. Palmen, P. Parker, G. Passos, T. G. Perring, P. F. Peterson, S. Ren, M. A. Reuter, A. T. Savici, J. W. Taylor, R. J. Taylor, R. Tolchenov, W. Zhou, and J. Zikovsky, Nucl. Instrum. Methods. Phys. Res. A **764**, 156 (2014).

[32] F. Akeroyd, S. Ansell, S. Antony, O. Arnold, A. Bekasovs, J. Bilheux, J. Borreguero, K. Brown, A. Buts, S. Campbell, D. Champion, L. Chapon, M. Clarke, S. Cottrell, R. Dalgliesh, D. Dillow, M. Doucet, N. Draper, R. Fowler, M. A. Gigg, G. Granroth, M. Hagen, W. Heller, A. Hillier, S. Howells, S. Jackson, D. Kachere, M. Koennecke, C. Le Bourlot, R. Leal, V. Lynch, P. Manuel, A. Markvardsen, R. McGreevy, D. Mikkelson, R. Mikkelson, R. Miller, S. Nagella, T. Nielsen, K. Palmen, P. G. Parker, M. Pascal, G. Passos, T. Perring, P. F. Peterson, F. Pratt, T. Proffen, P. Radaelli, J. Rainey, S. Ren, M. Reuter, L. Sastry, A. Savici, J. Taylor, R. J. Taylor, M. Thomas, R. Tolchenov, R. Whitley, M. Whitty, S. Williams, W. Zhou, and J. Zikovsky, 10.5286/SOFTWARE/MANTID (2013).

[33] A. V. Shapeev, Multiscale Model Simul. **14**, 1153 (2016).

[34] I. S. Novikov, K. Gubaev, E. V. Podryabinkin, and A. V. Shapeev, Mach. learn.: sci. technol. **2**, 025002 (2020).

[35] V. Ladygin, I. Beniya, E. Makarov, and A. Shapeev, Phys. Rev. B **104**, 104102 (2021).

[36] J. M. Dickey and A. Paskin, Phys. Rev. **188**, 1407 (1969).

[37] J.-P. Hansen and I. R. McDonald, *Theory of simple liquids: with applications of soft matter*, Fourth edition (Elsevier/AP, Amstersdam, 2013).

[38] S. M. Chathoth, B. Damaschke, T. Unruh, and K. Samwer, Appl. Phys. Lett. **94**, 221906 (2009).

[39] A. Meyer, EPJ Web of Conferences **83**, edited by B. Frick, M. M. Koza, M. Boehm, and H. Mutka, 01002 (2015).

[40] U. Balucani and M. Zoppi, *Dynamics of the liquid state* (Clarendon Press ; Oxford University Press Oxford, New York, 1994).

[41] B. N. Brockhouse and N. K. Pope, Phys. Rev. Lett. **3**, 259 (1959).

[42] D. Wallace, *Thermodynamics of crystals*, Dover Books on Physics (Dover Publications, 1998).

[43] D. Wallace, *Statistical Physics of Crystals and Liquids* (World Scientific, 2002).

[44] D. C. Wallace, S. Rudin, G. De Lorenzi-Venneri, and T. Sjostrom, Phys. Rev. B **99**, 104204 (2019).

[45] M. Palumbo, B. Burton, A. Costa e Silva, B. Fultz, B. Grabowski, G. Grimvall, B. Hallstedt, O. Hellman, B. Lindahl, A. Schneider, P. E. A. Turchi, and W. Xiong, Phys. Status Solidi B **251**, 14 (2014).

[46] Y. Shen, C. W. Li, X. Tang, H. L. Smith, and B. Fultz, Phys. Rev. B **93**, 214303 (2016).

[47] D. S. Kim, H. L. Smith, J. L. Niedziela, C. W. Li, D. L. Abernathy, and B. Fultz, Phys. Rev. B **91** (2015).

[48] C. M. Bernal-Choban, H. L. Smith, C. N. Saunders, D. S. Kim, L. Mauger, D. L. Abernathy, and B. Fultz, Phys. Rev. B **107**, 054312 (2023).

[49] F. W. De Wette and A. Rahman, Phys. Rev. **176**, 784 (1968).

[50] M. E. Manley, R. J. McQueeney, J. L. Robertson, B. Fultz, and D. A. Neumann, Philos. Mag. Lett. (2010).

[51] T. Schneider, R. Brout, H. Thomas, and J. Feder, Phys. Rev. Lett. **25**, 1423 (1970).

[52] L. Bosio, E. Schedler, and C. Windsor, J. phys. **37**, 747 (1976).

[53] T. Springer, *Quasielastic neutron scattering for the investigation of diffuse motions in solids and liquids*, Springer tracts in modern physics 64 (Springer, Berlin, 1992).

[54] J. R. D. Copley and S. W. Lovesey, Rep. Prog. Phys. **38**, 461 (1975).

[55] O. Soderstrom, J. R. D. Copley, J.-B. Suck, and B. Dorner, J. Phys. F: Met. Phys. **10**, L151 (1980).

[56] V. Hugouvieux, Theses (Université Montpellier II - Sciences et Techniques du Languedoc, Nov. 2004).

[57] V. M. Glazov and O. D. Shchelikov, High Temp. **38**, 405 (2000).

[58] S. P. Isherwood, B. R. Orton, and R. Mănăilă, J. Non-Cryst. Solids **8-10**, 691 (1972).

[59] S. Krishnan and D. L. Price, J. Phys.: Condens. Matter **12**, R145 (2000).

[60] J. A. Cahill and A. D. Kirshenbaum, J. Inorg. Nucl. Chem. **25**, 501 (1963).

[61] Y. Waseda, *The structure of non-crystalline materials : liquids and amorphous solids* (McGraw-Hill International Book Co. New York, 1980).

[62] L. Xu, Z. Wang, J. Chen, S. Chen, W. Yang, Y. Ren, X. Zuo, J. Zeng, Q. Wu, and H. Sheng, Nat. Commun. **13**, 126 (2022).

[63] S. A. Been, H. S. Edwards, C. E. Teeter Jr., and V. P. Calkins, NEPA Report 1585 (1950).

[64] Y. Waseda and K. Suzuki, Phys. Status Solidi B **49**, 339 (1972).

[65] P. S. Salmon, I. Petri, P. H. K. d. Jong, P. Verkerk, H. E. Fischer, and W. S. Howells, J. Phys.: Condens. Matter **16**, 195 (2004).

[66] F. H. Stillinger and T. A. Weber, Phys. Rev. A **25**, 978 (1982).

[67] F. H. Stillinger, Science **267**, 1935 (1995).

[68] P. G. Debenedetti and F. H. Stillinger, Nature **410**, 259 (2001).

[69] J. Y. Y. Lin, H. L. Smith, G. E. Granroth, D. L. Abernathy, M. D. Lumsden, B. Winn, A. A. Aczel, M. Aivazis, and B. Fultz, Nucl. Instrum. Methods. Phys. Res. A **810**, 86 (2016).

[70] E. R. Cowley, Solid State Commun. **14**, 587 (1974).

[71] A. D. Zdetsis and C. S. Wang, Phys. Rev. B **19**, 2999 (1979).

[72] A. Barla, R. Rüffer, A. I. Chumakov, J. Metge, J. Plessel, and M. M. Abd-Elmeguid, Phys. Rev. B **61**, R14881 (2000).

[73] V. F. Sears, E. C. Svensson, and B. M. Powell, Can. J. Phys. **73**, 726 (1995).

[74] J. Y. Y. Lin, F. Islam, and M. Kresh, J. Open Source Softw. **3**, 440 (2018).

[75] M. Y. Hu, W. Sturhahn, T. S. Toellner, P. D. Mannheim, D. E. Brown, J. Zhao, and E. E. Alp, Phys. Rev. B **67**, 094304 (2002).

[76] G. Kresse and J. Hafner, Phys. Rev. B **47**, 558 (1993).

[77] G. Kresse and J. Hafner, Phys. Rev. B **49**, 14251 (1994).

[78] G. Kresse and J. Furthmüller, Phys. Rev. B **54**, 11169 (1996).

[79] G. Kresse and D. Joubert, Phys. Rev. B **59**, 1758 (1999).

[80] P. E. Blöchl, Phys. Rev. B **50**, 17953 (1994).

[81] J. P. Perdew, K. Burke, and M. Ernzerhof, Phys. Rev. Lett. **77**, 3865 (1996).

[82] H. J. Monkhorst and J. D. Pack, Phys. Rev. B **13**, 5188 (1976).

[83] K. Gubaev, E. V. Podryabinkin, G. L. Hart, and A. V. Shapeev, Comput. Mater. Sci. **156**, 148 (2019).

[84] P. Korotaev, M. Belov, and A. Yanilkin, Comput. Mater. Sci. **150**, 47 (2018).

[85] D. Minakov, P. Levashov, and V. Fokin, Comput. Mater. Sci. **127**, 42 (2017).

[86] I. Novoselov, A. Yanilkin, A. Shapeev, and E. Podryabinkin, Comput. Mater. Sci. **164**, 46 (2019).

[87] A. P. Thompson, H. M. Aktulga, R. Berger, D. S. Bolintineanu, W. M. Brown, P. S. Crozier, P. J. in 't Veld, A. Kohlmeyer, S. G. Moore, T. D. Nguyen, R. Shan, M. J. Stevens, J. Tranchida, C. Trott, and S. J. Plimpton, Comp. Phys. Comm. **271**, 108171 (2022).

Chapter 5

CONCLUSIONS AND FUTURE DIRECTIONS

5.1 Conclusions

This thesis combined ab-initio and molecular dynamics simulations with inelastic neutron scattering measurements to investigate the atomic thermodynamics of pure elements. It revealed the roles of configurational, vibrational, electronic, and magnetic contributions in the systems considered. Additionally, the effect of each on the macroscopic properties, including the heat capacity and latent heat, was explored.

The beginning of this dissertation addressed conflicting reports on the roles of magnetism and anharmonicity in the paramagnetic phase of bcc chromium (Cr). Ab-initio-informed calculations using quasiharmonic (QH) and anharmonic (AH) models account for most of the entropy in high-temperature Cr. Previously measured phonon dispersions and time-of-flight neutron scattering show that the AH model is more representative of the actual vibrational physics in Cr. A relatively small but larger than anticipated electronic component helps bring the calculated and INS entropies into better agreement with calorimetric data. The remaining discrepancy between the total simulated and measured (INS and calorimetric) entropy is tentatively assigned to a phonon-paramagnon interaction.

Next, the entropic components in the latent heat of melting were discussed. It is well-established that vibrations dominate the solid and liquid entropies of materials. However, little about atomic interactions across the melting transition was known. Here, inelastic neutron scattering and computational techniques were combined to investigate such processes. Developing a new analysis routine of vibrational spectra from INS in the solid and liquid phases of Ge, Bi, Sn, and Pb revealed that the change in vibrational entropy across melting scales with the total entropy of fusion. This behavior was confirmed and extended to Si and Li using machine-learned interatomic potential molecular dynamics simulations. Configurational and electronic entropic components through the melt were also determined from these simulations and shown to be, respectively, significant and small. These results provided insight into the distinction between normal versus anomalous melting and revealed an interesting correlation in the potential energy surface across the

melt; as the change in the number of basins increases, the change in the curvature of the basins decreases.

Each study presented here is only possible with recent advances in computational and time-of-flight spectroscopy techniques. Investigating the importance of anharmonicity in high-temperature Cr relied on calculating third-order phonon processes (which required thousands of computational hours) and the high flux of the wide angular range chopper spectrometer (ARCS) at the Spallation Neutron Source. Only with both of these was another high-temperature contribution to the entropy (the proposed paramagnon-phonon coupling) discernible. The high flux and appropriate resolution of ARCS also made studying the vibrational spectra of liquids possible. Further analyses of the entropic components to the entropy of fusion were viable due to developments in neutron data processing and simulations using machine-learning interatomic potentials with thermodynamic integration.

5.2 Future Directions

As much as these studies highlight progress in scientific techniques, they also indicate what direction improvements can take.

Paramagnons in transition metals

The work on Cr identified an explanation for the gap between measured versus calculated anharmonic entropies but did not discuss how the proposed paramagnon interactions might be confirmed. To address this, new experimental and computational methods are needed.

Computational efforts to include magnetic contributions require an extensive exploration of phase space or knowledge of the existing magnetic structure [1, 2]. These difficulties arise from the additional degrees of freedom spin direction and magnitude add to a system. To date, full calculations are restricted to $T = 0\,\mathrm{K}$ [3] or only include collinear magnetization.

One avenue to explore is machine learning interatomic potentials. In addition to other complex problems, such methods were recently used to reproduce the high-temperature magnetic configurations of bcc iron [4]. If trained on the time-dependent density functional theory calculations such as those in [3], lower cost, accurate, high-temperature noncollinear magnetic structures (that include paramagnon-phonon interactions) may be possible to simulate.

Neutron scattering is the default for elucidating magnetic scattering due to the similar interaction intensity of atomic nuclei and magnetic moments. Furthermore, spherical neutron polarimetry can help distinguish magnetic states in complex magnetic structures, including skyrmions and coexisting spin density waves [5, 6], using spherical neutron polarimetry.

Resonant inelastic x-ray scattering (RIXS) is another option for investigating spin dynamics. Unlike neutrons, x-rays are more readily applicable to thin films but suffer from elastic line resolution. Nonetheless, RIXS has been used to ascertain spin waves in transition metals, including chromium, with long-range magnetic order [7, 8] and provide evidence of paramagnon excitations in superconductors [9].

Still, experimentally determining spin-lattice fluctuations above magnetic transition temperatures also presents challenges. Paramagnons are damped, dispersive excitations, and even with excellent statistical quality, distinguishing them from other components in spectra is complex. Fitting to models can help overcome some of this uncertainty but often involve many fitting parameters [10]. Additionally, low background and single crystals of high purity are necessary for most experiments that can probe magnetic fluctuations.

Ultimately, to get a true picture of paramagnon behavior in materials ab-initio or molecular dynamics calculations must be combined with state-of-the-art scattering techniques to compare and contrast models with scattering spectra.

Entropy contributions to melting, continued

Investigating the components of the entropy of melting revealed two trends in the elements considered. The first was that the vibrational entropy of fusion and the total entropy of fusion are directly correlated. A second unexpected observation was that the change in the number of basins across melting is inversely related to the change in the curvature of these basins. However, this study considered seven elements, and more support for these findings would be beneficial.

One of the difficulties with choosing additional elements for in-situ melting neutron measurements is that they must be compatible with experimental environments. For example, the sample must melt 200 K below the maximum furnace temperature to ensure a complete melt. Current furnace capabilities at Oak Ridge National Laboratory (ORNL) set this limit to 1400 K, which is low compared to the melting point of many elements. Activation, or how radioactive a material becomes after exposure to irradiation, is another issue to consider. Uranium melts

at about 1400 K, a reachable furnace temperature, but becomes highly radioactive. Therefore, it is a terrible candidate for melting studies. Checking neutron absorption cross-sections [11] gives hints for the severity of such activation. Other health hazards also must be addressed so that the safety concerns of the facility are assuaged. With these physical restrictions, only a subset of elements are viable for experiments.

Thankfully, computational methods do not suffer from sample environment or safety restrictions. However, they rely on the level of density functional theory (DFT) calculations performed, so care must be taken to validate these training simulations. Systems that may present a problem include those containing f-electrons, which are known to be predicted poorly with DFT, or those with unusual long-range structures (such as bismuth and selenium or complex magnetism).

Nevertheless, as the present melting study demonstrated, inelastic neutron scattering and machine-learning interatomic potentials are powerful tools for elucidating the components of the entropy of fusion. Combined, they can span a wide range of materials and complement the shortcomings of the other. Possible elements and compounds to investigate using (and improving on) these methods are outlined next.

Lanthanides generally have lower fusion entropies than Richard's rule predicts ($1.1k_B$/atom). Of this series, cerium (Ce, $\Delta S_{fus} = 0.61k_B$/atom) has a reasonable melting point (1068 K), is not strongly activated, and adopts a cubic structure above room temperature. These properties make Ce a strong contender for in-situ inelastic scattering melting measurements. If the reported correlation holds, the vibrational entropy across the melt would be more negative than in lithium (Li). An unexpected result (i.e., a deviation) would also be interesting since the f-electrons in Ce lead to valance instabilities [12] and are believed to affect melting temperatures [13]. In the latter case, computational methods including f-electron physics would be essential for determining the contributions across melting from each component. No matter the result, such a study would provide insight into another region of "anomalous" melters.

Another option is to extend the exploration of atomistic contributions of melting to binary compounds. The question then becomes what alloys to investigate. Ionic compounds (NaCl, MgI) pose a challenge due to their charge separation [14], and binary alloys that form two liquid phases are also not ideal. Here, the ASM Alloy Phase Diagram Database provides guidance. A search of metal alloys reveals that

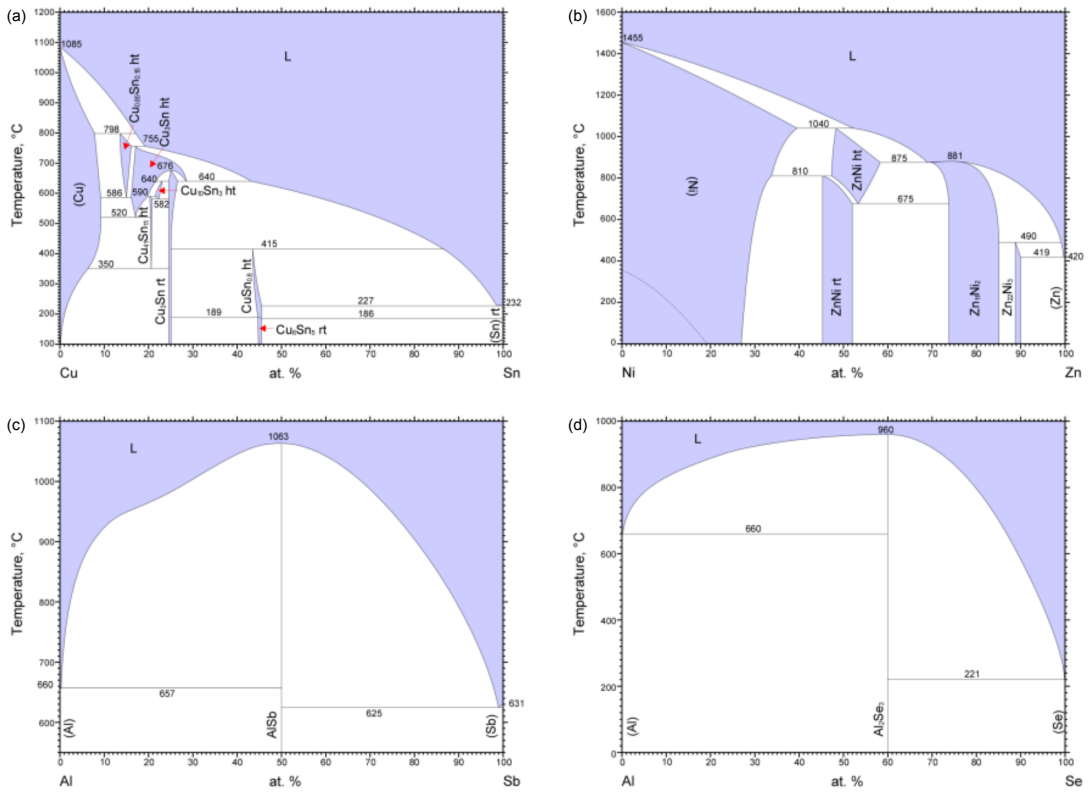

Figure 5.1: Binary phase diagrams for (a) Cu-Sn, (b) Ni-Zn, (c) Al-Sb, and (d) Al-Se. Reproduced with permission from [15–18].

Cu-Sn, Al-Sb, Al-Se, and Ni-Zn compounds could be viable (Fig. 5.1). Each system contains an alloy that meets the temperature and activation constraints of inelastic neutron scattering and is accessible with simulations. Furthermore, each introduces increased complexity in the entropy. This is due to new physics from configurational entropy in the solid phase (all, from the solid solution containing more than one atom), magnetic moments (Ni-Zn), and melting temperatures higher than the constituent elements (Al-Sn and Al-Sb), all effects that have yet to be considered in the melting work.

To conclude, plenty of materials remain to study the fundamental, atomistic physics of melting.

References

[1] F. Körmann, A. Dick, T. Hickel, and J. Neugebauer, Phys. Rev. B **81**, 134425 (2010).

[2] S. H. Lohaus, M. Heine, P. Guzman, C. M. Bernal-Choban, C. N. Saunders, G. Shen, O. Hellman, D. Broido, and B. Fultz, Nat. Phys., 1 (2023).

[3] K. Cao, H. Lambert, P. G. Radaelli, and F. Giustino, Phys. Rev. B **97**, 024420 (2018).

[4] I. Novikov, B. Grabowski, F. Körmann, and A. Shapeev, NPJ Comput. Mater. **8**, 1 (2022).

[5] N. Qureshi, E. Ressouche, A. Mukhin, M. Gospodinov, and V. Skumryev, Sci. Adv. **6**, eaay7661 (2020).

[6] J. Tosado, W. C. Chen, S. Gnewuch, T. Hasaan, T. Dax, and E. E. Rodriguez, Rev. Sci. Instrum. **90**, 063303 (2019).

[7] K. Sugimoto, Z. Li, E. Kaneshita, K. Tsutsui, and T. Tohyama, Phys. Rev. B **87**, 134418 (2013).

[8] N. B. Brookes, D. Betto, K. Cao, Y. Lu, K. Kummer, and F. Giustino, Phys. Rev. B **102**, 064412 (2020).

[9] M. C. Rahn, K. Kummer, N. B. Brookes, A. A. Haghighirad, K. Gilmore, and A. T. Boothroyd, Phys. Rev. B **99**, 014505 (2019).

[10] L. Wang, G. He, Z. Yang, M. Garcia-Fernandez, A. Nag, K. Zhou, M. Minola, M. L. Tacon, B. Keimer, Y. Peng, and Y. Li, Nat. Commun. **13**, 3163 (2022).

[11] V. F. Sears, Neutron News **3**, 26 (1992).

[12] J. M. Lawrence, M. C. Croft, and R. D. Parks, in *Valence Instabilities and Related Narrow-Band Phenomena* (Boston, MA, 1977), pp. 35–47.

[13] E. A. Kmetko and H. H. Hill, J. Phys. F: Met. Phys. **6**, 1025 (1976).

[14] Y. Shinohara, A. S. Ivanov, D. Maltsev, G. E. Granroth, D. L. Abernathy, S. Dai, and T. Egami, J. Phys. Chem. Lett. **13**, 5956 (2022).

[15] P. Nash and Y. Pan, J. Phase Equilibria **8**, 422 (1987).

[16] N. Saunders and A. Miodownik, Bull. alloy phase diagr. **11**, 278 (1990).

[17] H. Okamoto, J. Phase Equilibria **18**, 217 (1997).

[18] J. M. Howe, Bull. alloy phase diagr. **10**, 650 (1989).